NEW APPLICATIONS OF THz TIME-DOMAIN SPECTROSCOPY

By

TAE-IN JEON

Bachelor of Science
Dong-A University
Pusan, Korea
1987

Master of Science
Dong-A University
Pusan, Korea
1989

Submitted to the Faculty of the
Graduate College of the
Oklahoma State University
in partial fulfillment of
the requirements for
the Degree of
DOCTOR OF PHILOSOPHY
May, 1997

PREFACE

This thesis was conducted to provide new applications to THz time-domain spectroscopy and to test alternative theories of conduction by precisely measuring the complex conductivity of doped silicon from low frequencies to frequencies higher than the plasma frequency and the carrier damping rate. I hope this thesis should be of interest to a wide audience of researchers who use thin film and doped silicon as an optical material at THz frequencies.

I would like to sincerely thank Dr. Daniel Grischkowsky, my principal advisor, for his intelligent supervision, constructive guidance, scholarship, and encouragement. The helpful advice of the other committee members, Dr. Jin-Joo Song, Dr. Louie G. Johnson, Dr. James C. West, and Dr. Alan Cheville are also gratefully appreciated. I would also like to thank Dr. Nir Katzenellenbogen, Dr. Roger W. McGowen, and Dr. Xincheng Xie for informative discussions. Dr. Michael B. Santos and Dr. Patrick J. MCCan of University of Oklahoma also have my thanks for helping my experiments.

Finally, I would also like to thank my parents Jeong-Weon Jeon and Ok-Sun Ji; my loving wife Jeong-Weon Oh; proud daughter and son Ha-Keong Jeon and Hong-Ki Jeon. They give me encouragement and love throughout this process.

TABLE OF CONTENTS

LIST OF TABLES

LIST OF FIGURES

NOMENCLATURE

A	Parameter in phenomenological equation, $cm^2K^{\gamma}V^{-1}sec^{-1}$
c	Speed of light, cm/sec
D	Parameter in phenomenological equation
D_i	Parameter in phenomenological equation
D_r	Parameter in phenomenological equation
d	Thickness of sample, cm
e	Electronic charge, C
k	Boltzmann constant, J/K
m^*	Effective carrier mass, kg
m_e	Effective mass of electrons, kg
m_h	Effective mass of holes, kg
m_o	Free electron mass, kg
N	Number density of carriers, $1/cm^3$
N_{ref}	Parameter in phenomenological equation, $1/cm^3$
n_r	Real part of index of refraction
n_i	Imaginary part of index of refraction
n_1~n_5	Index of refraction
R_s	Magnitude reflection from silicon sample
R_w	Magnitude reflection from silicon window
R_{23}	Magnitude of r_{23}
r_{12},r_{23}	Reflection coefficient
$r_{\perp 23}$	Reflection coefficient for perpendicular incidence

T	Absolute temperature, K
T_o	Parameter in phenomenological equation
T_{tot}	Magnitude of total transmission
t_{tot}	Total transmission
t_{12}, t_{21}	Transmission coefficient
α	Power absorption coefficient, 1/cm
β	Cole-Davidson distribution parameter
β_o	Parameter in phenomenological equation
ε	Complex dielectric constant
ε_o	Permittivity of free space, F/m
ε_∞	Limiting high frequency dielectric constant of silicon
$\Phi(t)$	Time-dependent decay function
Φ_o	Parameter in phenomenological equation
ϕ_{tot}	Phase of total transmission, rad
ϕ_{23}	Phase of r_{23}, rad
Γ	Damping rate, THz
$\Gamma(E)$	Energy dependent damping rate, THz
$\Gamma_L(E)$	Energy dependent damping rate of lattice scattering, THz
$\Gamma_I(E)$	Energy dependent damping rate of impurity scattering, THz
Γ_l	Lattice coupling constant, THz
Γ_i	Impurity coupling constant, THz
γ	Parameter in phenomenological equation

λ_o	Free space wavelength, m
μ	Carrier mobility, cm^2/Vsec
μ_{max}	Parameter in phenomenological equation, cm^2/Vsec
μ_{min}	Parameter in phenomenological equation, cm^2/Vsec
θ	Incident angle
ρ_{CD}	Distribution of relaxation time
σ	Complex conductivity, Ω^{-1} cm^{-1}
σ_{dc}	dc conductivity, Ω^{-1} cm^{-1}
σ_r	Real part conductivity, Ω^{-1} cm^{-1}
σ_i	Imaginary part conductivity, Ω^{-1} cm^{-1}
σ_∞	Real conductivity at infinite frequency, Ω^{-1} cm^{-1}
$\sigma'_{\omega o}$	Parameter in phenomenological equation, Ω^{-1} cm^{-1}
$\sigma''_{\omega o}$	Parameter in phenomenological equation, Ω^{-1} cm^{-1}
$\sigma'_{\omega m}$	Parameter in phenomenological equation, Ω^{-1} cm^{-1}
$\sigma''_{\omega m}$	Parameter in phenomenological equation, Ω^{-1} cm^{-1}
τ	Carrier relaxation time, sec
τ_{CD}	Characteristic relaxation time, sec
$\tau(E)$	Energy dependent carrier relaxation time, sec
$\tau_L(E)$	Energy dependent carrier relaxation time of lattice scattering, sec
$\tau_I(E)$	Energy dependent carrier relaxation time of impurity scattering, sec
ω	Angular frequency, THz
ω_p	Plasma angular frequency, THz

C-D	Cole-Davidson
CPM	Colliding-Pulse Mode-locked
FWHM	Full Width at Half Maximum
GaAs	Gallium Arsenide
GHz	Giga Hertz
Si	Silicon
SOS	Silicon-On-Sapphire
TDS	Time-Domain Spectroscopy
THz	Tera Hertz

CHAPTER I

INTRODUCTION

For several years the electronics industry has made increasing use of semiconductor materials in the manufacture of solid-state components. Most of these devices have been made of silicon, and after oxygen (45.5 %), silicon (27.2 %) is the most abundant element in the earth's crust. To improve production and design processes, much research has gone into the physical properties of this material. In order to characterize semiconductor materials, knowledge of resistivity, concentration of carriers, and carrier mobility is necessary, and these three characteristics of the materials are related to dopant levels.

Four-point probe [1], Van der Pauw measurement [2], and Hall effect measurement [3] can measure the characteristics of the semiconductor materials by direct sample contact. Four-point probe and Van der Pauw measurements measure only the resistivity, while Hall effect techniques measure the carrier density and the carrier mobility. The use of the four-point probe requires prior calculation of the correction factors of the sample, which are dependent on the size and thickness of the sample [1, 4]. All of these electrical measurements measure only d.c. values of a sample, but some electrical and optical characteristics (conductivity, power absorption, and index of refraction) have frequency-dependent values. In some semiconductor wafers, such as GaAs, it is very difficult to characterize their electrical properties with simple mechanical contacts, due to the Schottky barrier at the metal-semiconductor interface. This Schottky barrier is one of the important error sources in the electrical measurements. Therefore, a contactless and frequency-dependent method of electrical characterization of semiconductor wafers would be extremely desirable.

Many physicists have studied the dynamics of carriers in semiconductors without contact to the wafers by microwave techniques [5, 6]. Microwave techniques can probe only low frequencies, but the strongest absorption of the free carriers and change in index of refraction lie between 0.1 THz and 2 THz. For reliable characterization of commercially important silicon, the dynamics of carriers must be investigated in the frequency range from 0.1 THz to 2 THz.

Recently the powerful technique of THz time-domain spectroscopy (TDS) has been applied to several systems in the range from 0.1 THz to 2 THz [7, 8, 9]. THz-TDS is based on the optoelectronic generation and reception of a beam of subpicosecond terahertz pulses. These pulses of terahertz electromagnetic radiation can be detected with signal-to-noise ratio of better than 10,000 to 1 [18]. This thesis describes an application of THz-TDS for measuring absorption and dispersion from 0.08 THz to 2.5 THz. Using THz-TDS transmission measurement, thin films and Si wafers were measured and the power absorption and index of refraction were calculated. Using the THz radiation radar system [19], reflected THz pulses from silicon sample surfaces were measured and the reflection coefficient and phase shift were analyzed.

In the transmission measurement of the Si samples the difference between the index of refraction of the Si sample and the index of refraction of free space results in the reflection of THz pulses from the surface of the sample. The time-delayed reflected THz pulse occurs after the main pulse, corresponding to the round-trip time inside the sample. Like the time delay of the main pulse, the time delay of the reflected THz pulse depends on the index of refraction and the thickness of the sample. The multiple reflections from the wafer surfaces were eliminated by sandwiching the wafers between thick plates of high resistivity silicon (greater than 10 kΩ cm). Because the index of refraction of the doped silicon is suddenly increased at lower frequency ranges, there was an index of refraction mismatch between the Si window and Si sample at these frequency ranges. Therefore it required an additional magnitude and phase shift compared to the usual simple analysis.

The experimental results of the Si samples by the transmission measurement were fitted by alternative theories: Drude theory, scattering theory, and Cole-Davidson distribution. The experimental results were well fit in the low frequency ranges by the Drude theory but in the high frequency ranges Drude theory was not a good fit, especially for power absorption and real conductivity. The scattering theory [10,11,12], where the carrier relaxation time was energy-dependent, fits better than the Drude theory but there were still deviations in the high-frequency ranges. All the measurement results were exceptionally well fit by a Cole-Davidson (C-D) distribution [13, 14, 15], which corresponds to Drude theory with a fractional exponent β.As the carrier density is increased, β approaches unity. The results presented here are the first application of the C-D distribution to fit the complex conductivity of well-ordered crystalline semiconductors. All the *n* and *p* type samples were analyzed by these three different theories and fitted in the frequency range from 0.08 THz to 2.5 THz.

CHAPTER II

THz TIME-DOMAIN SPECTROSCOPY (THz-TDS) SYSTEM

Experimental Setup

Recently, high-performance optoelectronic sources [16, 17, 18] have been used to generate and detect short pulses of terahertz (THz) radiation. Such a THz optoelectronics system is illustrated in Figure 2-1 (a). The distance between the center of a paraboloidal mirror and the transmitter or receiver chip is 12 cm which is the focal length of the paraboloidal mirror. The diameter of the paraboloidal mirror is 7.62 cm (3 inches). The distance between the centers of the two paraboloidal mirrors is 26 cm. A colliding-pulse mode-locked (CPM) dye laser provides 623 nm, 130 fsec (auto-correction pulse width) excitation pulses at a 100 MHz repetition rate with an average power of 6 mW. When the laser pulses arrive at the transmitter or receiver chip, the THz pulses are generated or detected, respectively. Figure 2-1 (b) shows the experimental setup. Because the optoelectronic receiver is gated synchronously with the excitation of the transmitter, the two paths between the beamsplitter and the receiver chip should be the same length. The THz pulse is obtained by scanning the relative time delay between the laser excitation pulse and the laser detection pulse.

The measurement delay line is controlled through a programmable motor controller (Klinger model MC1). When the measurement delay line is stepped to measure the data, the manual delay line is fixed. The manual delay line is used only to optimize THz signal while adjusting the THz system. In order to eliminate the effects of water vapor on the terahertz beams [17], the THz system is located in an airtight dry box.

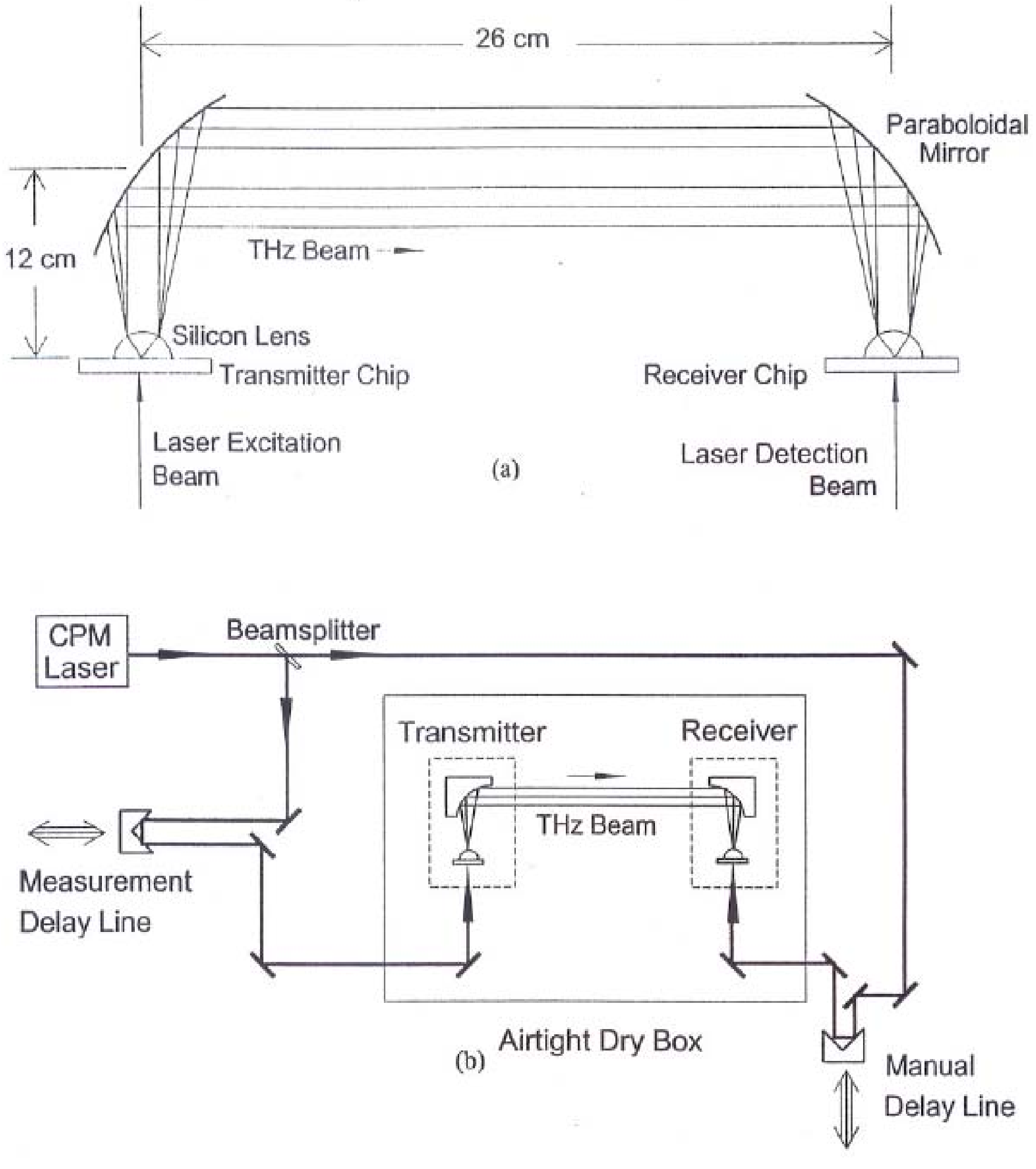

Figure 2-1 (a) Schematic diagram of the optoelectronic THz beam system. (b) Schematic diagram of the experimental setup.

Generating THz Radiation

Two kinds of high-resistivity Gallium Arsenide (GaAs) chips were used as a THz transmitter. A GaAs 10-80-10 transmitter chip was used for high frequency range and a GaAs bowtie 30^o transmitter chip was used for low frequency range.

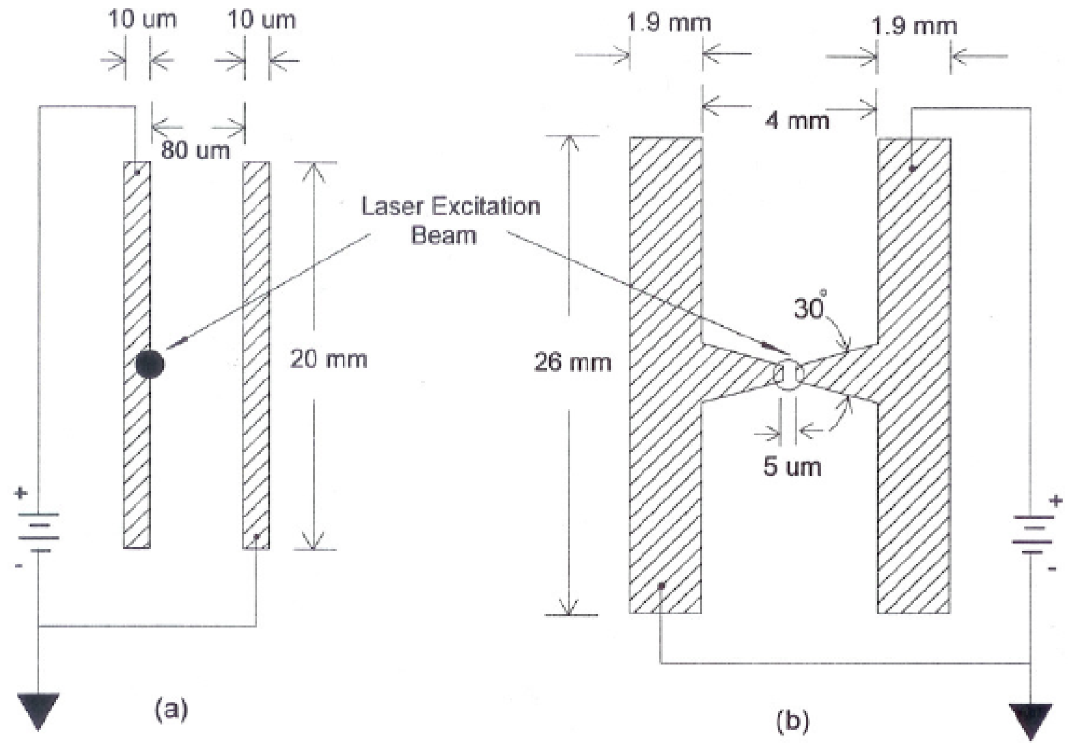

Figure 2-2. Antenna structure used in transmitter chip
(a) GaAs 10 80-10 (b) GaAs Bowtie 30^o.

GaAs 10-80-10 Transmitter Chip

This chip consists of coplanar 10 μm wide, 20-mm-long, metal lines separated by 80 μm, fabricated on high-resistivity GaAs as shown in Figure 2-2(a). The measured dc resistance of a single 10 μm transmission line is 120 Ω/mm. The laser excitation is focused onto the metal-semiconductor interface of the positively biased (96V) transmission line. A slice of indium was used to make an ohmic contact between an electric wire and the transmission line. This was accomplished by sandwiching the electric wire between slices of indium at the end of the transmission line. Pressure was applied to make contact.

The generation and detection THz pulses were discussed previously [7-9, 16-18]. Each excitation laser pulse creates a spot of photocarriers in a region of extremely high electric field. The consequent acceleration of the carriers generates the burst of terahertz radiation. This laser-generated burst of terahertz radiation is emitted into the transmitter chip in a cone normal to the interface, and is then collected and collimated by a crystalline silicon lens attached to the back side of the chip. After collimation by the silicon lens, the THz beam propagates and diffracts to a paraboloidal mirror where the THz beam is recollimated into a highly directional beam. The THz beam has an average power of 10 nW [18] and the propagating THz beam has a frequency-dependent cross section [11]. The low-frequency components are more spread out than the high-frequency components.

GaAs Bowtie 30^o Transmitter Chip

This chip consists of coplanar 1.9 mm wide, 26-mm-long, transmission lines separated by 4 mm and two 30^o dipole antenna separated by a 5 μm gap as shown in Figure 2-2 (b). The laser excitation beam is focused onto the 5 μm gap of the biased dipole antenna. Because the dipole antenna gap is only 5 μm, the dc voltage bias is 8 V.

Optical Lens Mount and Adjustment

The optical lens used to focus the laser excitation beam (2 mm beam diameter) onto the transmission line had a focal length of 6 mm. The diameter of the excitation spot was 10 µm. The optical lens was secured to small aluminum brackets with epoxy glue as shown in Figure 2-3 below.

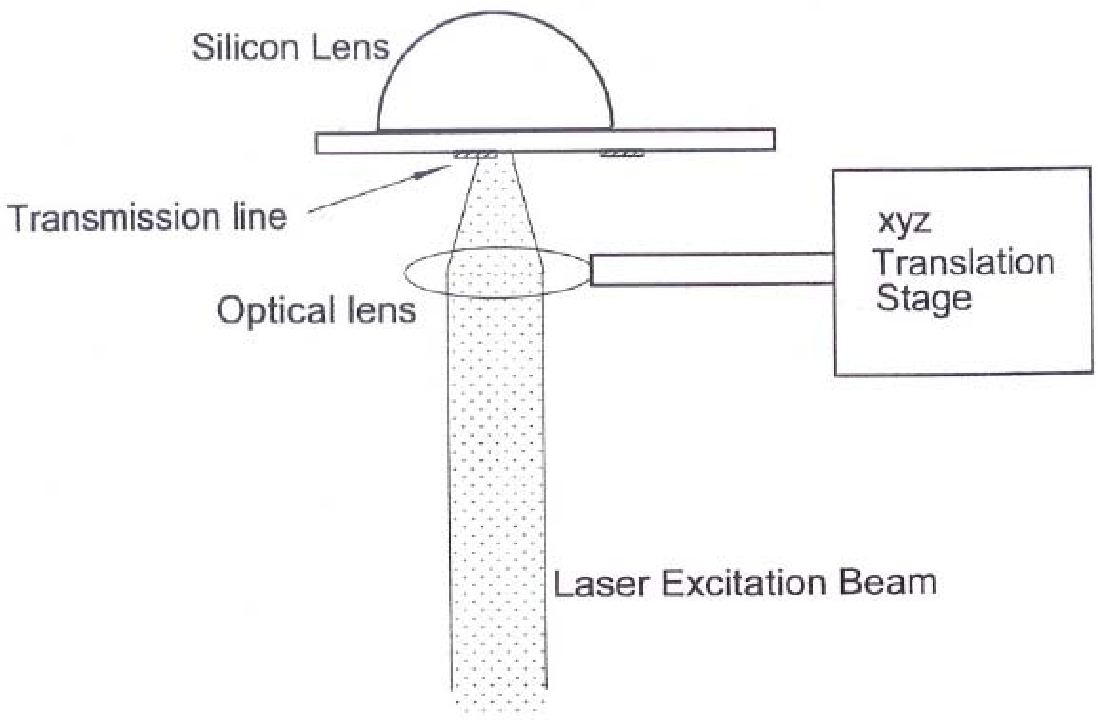

Figure 2-3. Focus of the laser excitation beam by the optical lens.

The bracket was secured to a Newport 642 xyz translation stage. This enabled precise positioning of the lens. Because the transmission lines are only 10 µm wide, it is necessary to have very precise adjustment of the laser spot position by the translation stage. In order to concentrate the energy of the laser excitation beam, the laser beam should be perpendicular to the transmitter chip.

Silicon Lens Mount and Adjustment

Silicon lenses were used to collimate the outgoing THz beam at the transmitter and recollimate the beam incident upon the receiver. These silicon lenses were made by Insaco Inc. These special order lenses are composed of high-resistivity (10 kΩ) single-crystal silicon. The dimensions of the silicon lens at the transmitter are 6.46 mm height, 5 mm radius, and 8.9 mm diameter, and the dimensions silicon lens at the receiver are 6.41 mm height, 5 mm radius, and 8.9 mm diameter. Figure 2-4 shows the dimensions of the silicon lens.

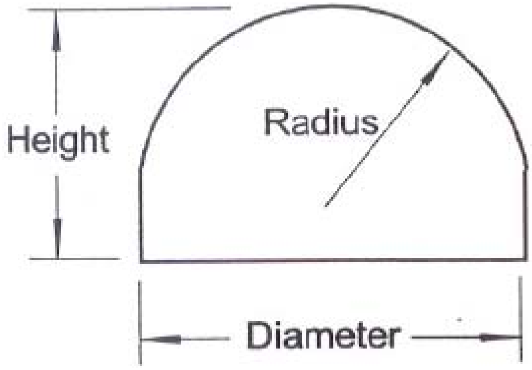

Figure 2-4. Diagram of silicon lens

The lenses mount directly against the back surface of the transmitter or receiver chip. Each silicon lens is held in place by pressure from a spring and collar within a modified Newport Fiber Optic Coupler. Thereby the THz beam can propagate without refraction or loss from the interface between the lens and the chip. The center of the silicon lens should be located at the collimated laser focus to allow for maximum transmission of the THz beam. The modified coupler allows for adjustment of the lens position in the x and y directions as necessary.

Detecting THz Radiation

After 50cm (from transmitter chip to receiver chip) of propagation though free space, the terahertz beam is incident upon the receiver. A second matched paraboloidal mirror focuses the beam onto a second silicon lens which is attached to the back side of the receiver chip. The receiver chip, shown in Figure 2-5, consists of two 20-μm-wide stubs separated by a 5-μm gap in a coplanar transmission line consisting of two parallel 10-μm-wide aluminum lines separated from each other by 30μm. This structure was fabricated on an ion-implanted silicon-on-sapphire (SOS) wafer.

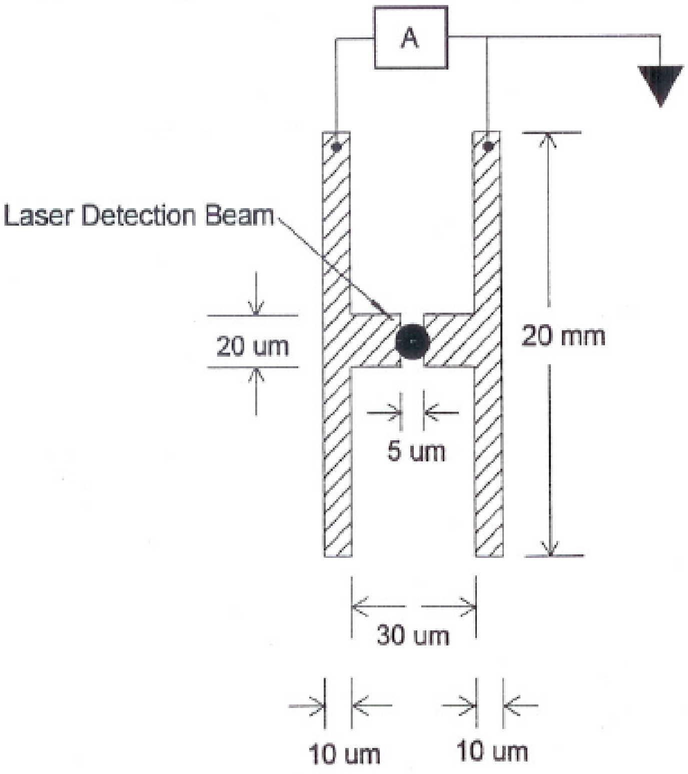

Figure 2-5. Antenna structure used in receiver chip.

The electric field of the focused terahertz radiation induces a transient bias voltage across the 5-μm antenna gap. This receiving antenna is directly connected to a low-noise current amplifier which is connected to a lock-in amplifier. The time-dependent induced voltage across the antenna gap is obtained by measurement of the collected charge versus the time delay between the terahertz pulse and an optical pulse which synchronously gates the receiver. To maximize the signal the center of the silicon lens should be located at the focus of the laser detection beam.

Data Gathering

Recording of data was accomplished with the receiving antenna, a low-noise current amplifier (Ithaco model 1211), a lock-in amplifier (Stanford Research Systems model SR530), an analog to digital (A/D) converter and a personal computer as shown in Figure 2-6. The computer records data using the Viewdac 2.2 data acquisition software package.

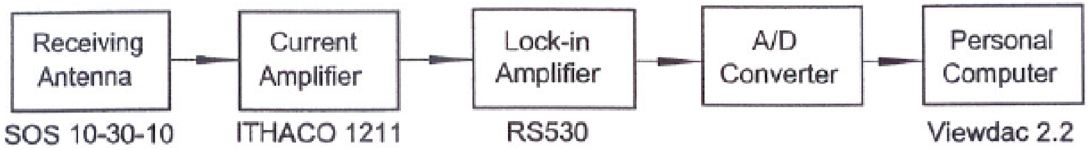

Figure 2-6. Block diagram of data gathering.

CHAPTER III

THz TIME-DOMAIN SPECTROSCOPY MEASUREMENTS

Noise Reduction

In order to optimize the signal-to-noise ratio noise sources should be minimized. Compared to previous THz measurements some noise sources were discovered and the noise level reduced. The following noise analysis is applicable to my THz system which used a CPM laser. The actual noise levels will depend on the type of devices used and the laser source. Because each noise level was measured in different conditions (devices and laser stability), the relative magnitudes cannot be compared.

Chip Noise

In the absence of the CPM laser beam, the noise of the receiver chip (SOS 10-30-10, 0.33 MΩ resistance between two transmission lines) was 0.45 pA rms for a 100 ms integration time on the Lock-in amplifier (Stanford Research Systems model SR530) with the current amplifier (Ithaco model 1211) at a setting 10^{-7} A/V. Because of the different receiver chip, this noise level is higher than the previous measurement [18]. The noise level depends on the size of a dipole antenna and the condition of chips. The high resistance chip has a small noise (SOS 10-200-10, 9.6 MΩ resistance, has 0.095 pA rms). The width of the transmission lines of the transmitter or receiver chip is only 10 μm as shown in Figure 2-2 (a) and Figure 2-5. If these thin transmission lines are damaged, the THz pulse also has noise. Because the transmission lines are very sensitive, a small static spark damages the transmission lines. Whenever a person touches the chips the other hand should be connected to ground. If the chips are damaged, the THz noise is very large compared to the other noise sources.

Laser Noise

The noise from a colliding pulse mode locking (CPM) laser is very complicated and its noise is directly related to the THz noise. The laser noise is the second largest noise source of the THz system (The largest noise is thermal noise) [18]. One of the noise sources of a CPM laser is the pumping laser which uses an Ar^+ laser (Spectra Physics model 2030). This noise level is very small compared to the output noise of the CPM laser. Figure 3-1 (a, b) show the noise from the pumping laser and CPM laser These noise curves were measured by a photodetector (Hamamatsu model S2837) connected to a digitizing signal analyzer (Tektronix model DSA 601A). When the CPM laser is stable, the rms value of the laser noise is 5.23 mV and the offset value is 342.6 mV. Thereby the relative laser noise is 1.5%. However, the rms value of Ar^+ laser noise is 0.42 mV and the offset value is 174.5 mV. The relative pumping laser noise is 0.24% (0.5% noise is the specification of the Ar^+ laser) and it is about 16% of the total CPM laser noise. The other noises are generated by the CPM laser itself.

In my experience the main noise source from the CPM laser is a poor alignment of the CPM laser ring cavity. It is very difficult to find the right position of the two dyes, especially the DODC Iodide dye. Whenever the laser is mode locked, the position of DODC Iodide dye is carefully adjusted to make a stable laser. The second noise source is from bad dyes: DODC Iodide and Rhodamine 590 Chloride (Rh-6G). Usually the lifetime of DODC Iodide is about 1 month and of Rh-6G is about 5 months. The laser is very unstable at the end of these lifetimes. The last noise source is the vibration from the two dye jets. The two dyes are circulated by a pumping motor. If the dye tube is in contact with the vibration source, the vibration transfers to the dye. The vibration of the dye which is focused by the laser beam directly creates an unstable laser beam. To make a stable laser beam all vibration sources must be removed.

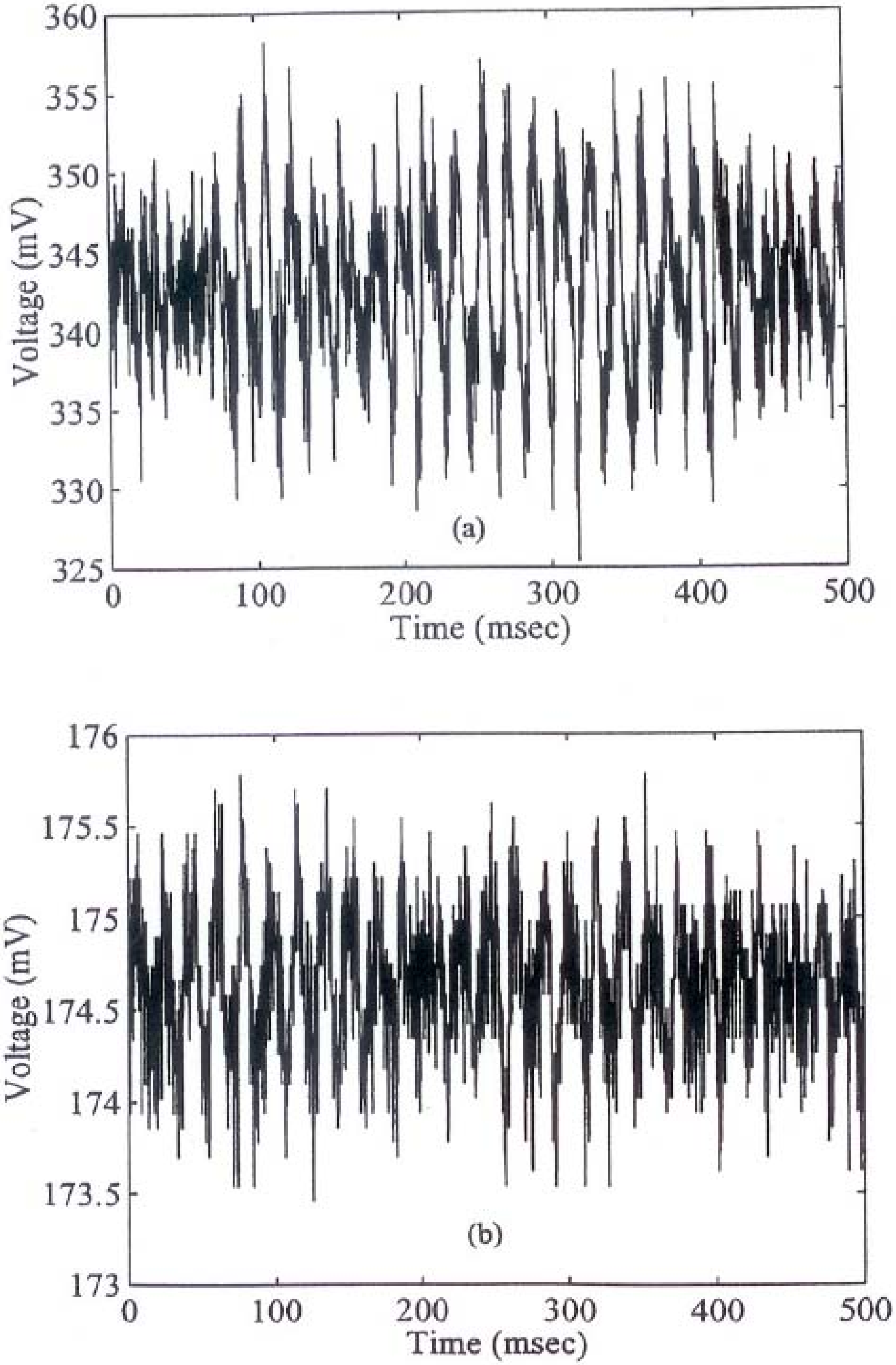

Figure 3-1. Noise from laser. (a) CPM laser noise (1.5% relative noise). (b) Pumping laser (Ar^+ laser) noise (0.24% relative noise).

Chopper Noise

The generated THz pulse from the transmitter chip is mechanically chopped before striking the first paraboloidal mirror. When the chopper motor (Stanford Research System model SR540) is operating, the motor vibration transfers to the transmitter or receiver chip through the optical table. In the air tight dry box, the motor noise affects the noise to the receiver chip. Figure 3-2 (a,b) show the relative noises which are related the motor noise. When an aluminum plate (17.4 cm × 24.3 cm) is located near the receiver chip to block the motor noise from the chopper, the noise was reduced as shown in Figure 3-2(b). Without the aluminum plate, the rms value was 17.1 mV and with the aluminum plate the rms value was 10.8 mV. The rms values are measured using the SOS 10-30-10 antenna, a current amplifier at setting 10^{-9} V/A, and a signal analyzer. The high-speed chopper also generates air movement inside of the dry box. This air movement is related static noise which is discussed in a later section on *static noise*.

In order to reduce these problems the chopper was moved outside of the dry box and not attached to the optic table. The chopper modulates the laser excitation beam to provide a reference frequency to the Lock-in amplifier. Thus we can avoid the vibration, motor noise, and static noise problems. To reduce the photocurrent from the transmission chip and the noise of an electronic component, the chopper had to rotate with high frequency. Figure 3-3 (a, b) shows these relations. Figure 3-3 (a) shows the THz noise when the chopper frequency is 455 Hz and Figure 3-3 (b) shows the THz noise when the chopper frequency is 3000 Hz. The inserts show the noise on an expanded time and current scale. Now the real THz noise is reduced 50%.

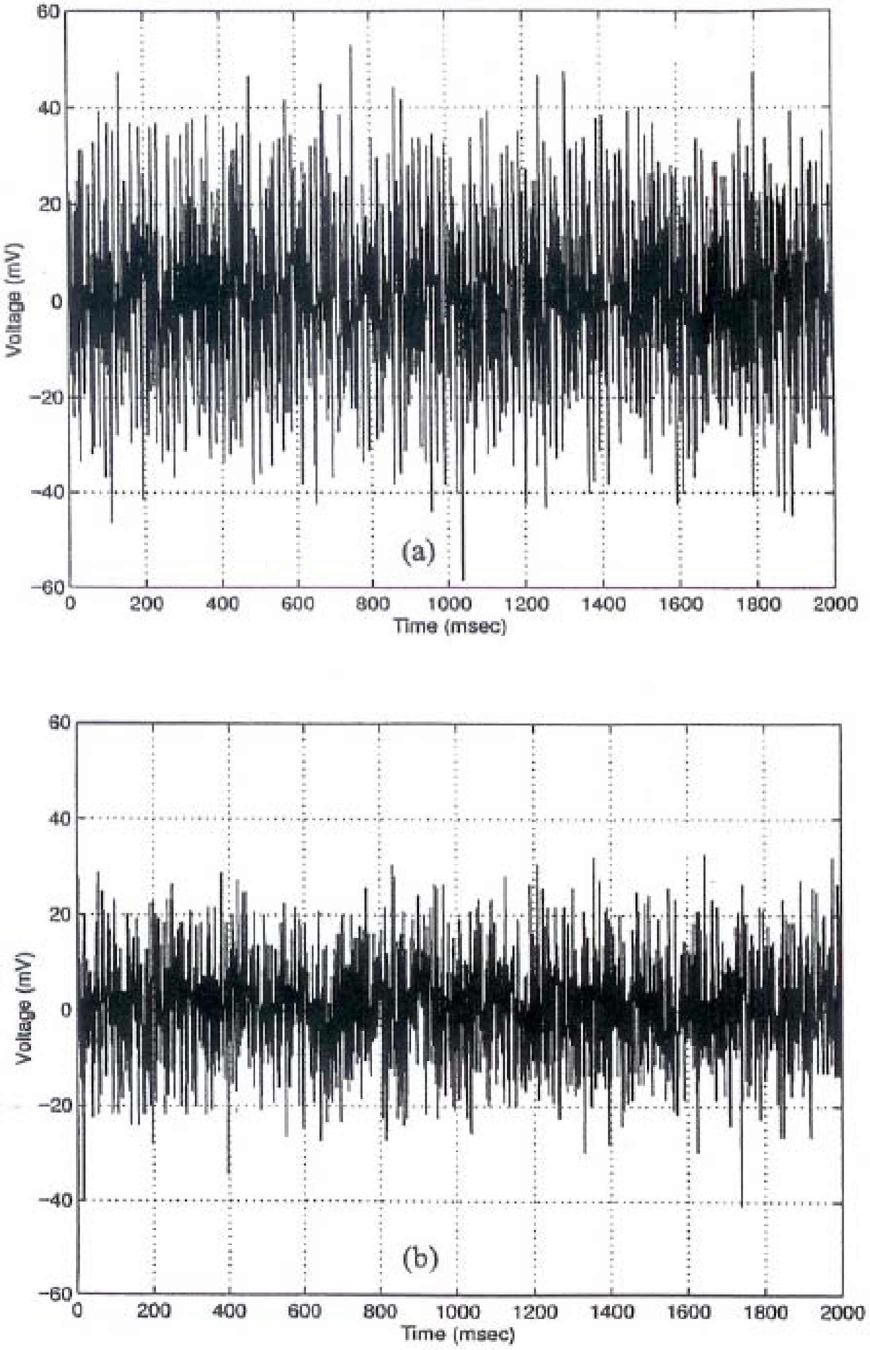

Figure 3-2. Noise from chopper motor. (a) Noise from receiver chip without the aluminum plate. (b) Noise from receiver chip with the aluminum plate.

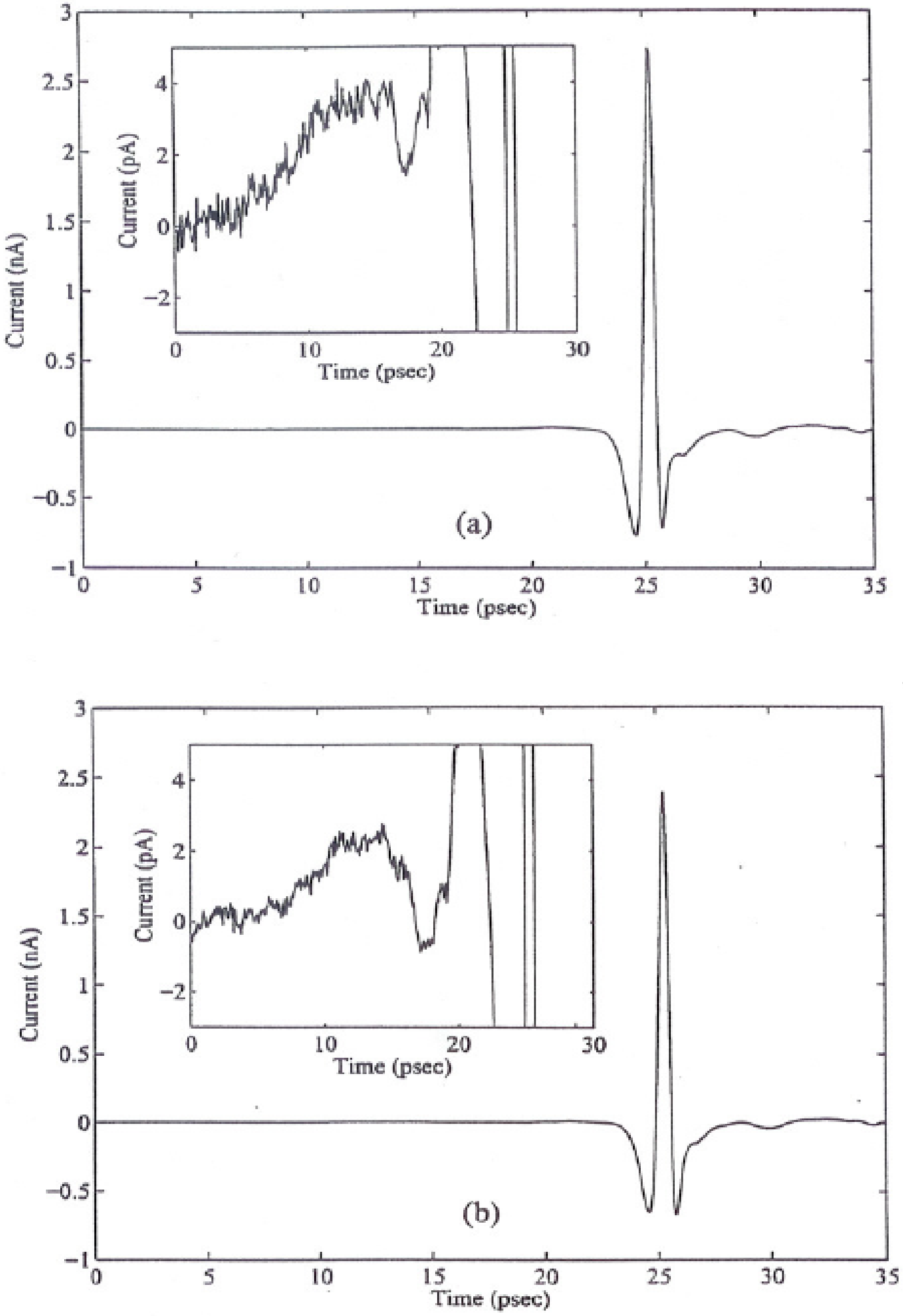

Figure 3-3 The THz noise when the chopper is cutting the excitation laser beam. The inserts show the noise on an expanded time and current scale. (a) Chopper frequency 455 Hz. (b) Chopper frequency 3000 Hz.

60 Hz Noise

Every electric device has 60 Hz noise from the power line. The photoconductive THz switch is also sensitive 60 Hz noise because the photoconductive switch is sensitive to room lights. Figure 3-4 (a, b) show the noise from the receiver chip and its spectrum. This kind of noise is expected around harmonics of 60 Hz. If the chopper frequency is a multiple of 60 Hz, the current amplifier receives no signal except 60 Hz noise [19]. This problem can be reduced by turning off the room light or blocking the room light from the receiver chip. Figure 3-4 (c, d) show the noise and its spectrum when turning off the room light. When the room light was on, the rms noise value was 33.6 mV. When the room light was off, the rms noise value was 16.4 mV. The rms values are measured by SOS 10-30-10, the current amplifier at setting 10^{-9} V/A, and a signal analyzer. In Figure 3-4 (d) most of the 60 Hz noise was removed compared to Figure 3-4 (b).

Static Noise

To reduce water vapor in the air, the THz system is located in an airtight dry box and continually supplied with dry air during measurement of the THz signal. This dry air movement makes a static charge on the box, and the charged box makes static noise in the receiver chip. To reduce the static noise, the box is covered with aluminum foil and connected to ground. Then the receiver chip is protected from some outside noise sources such as static noise, 60 Hz noise and electric wave noise.

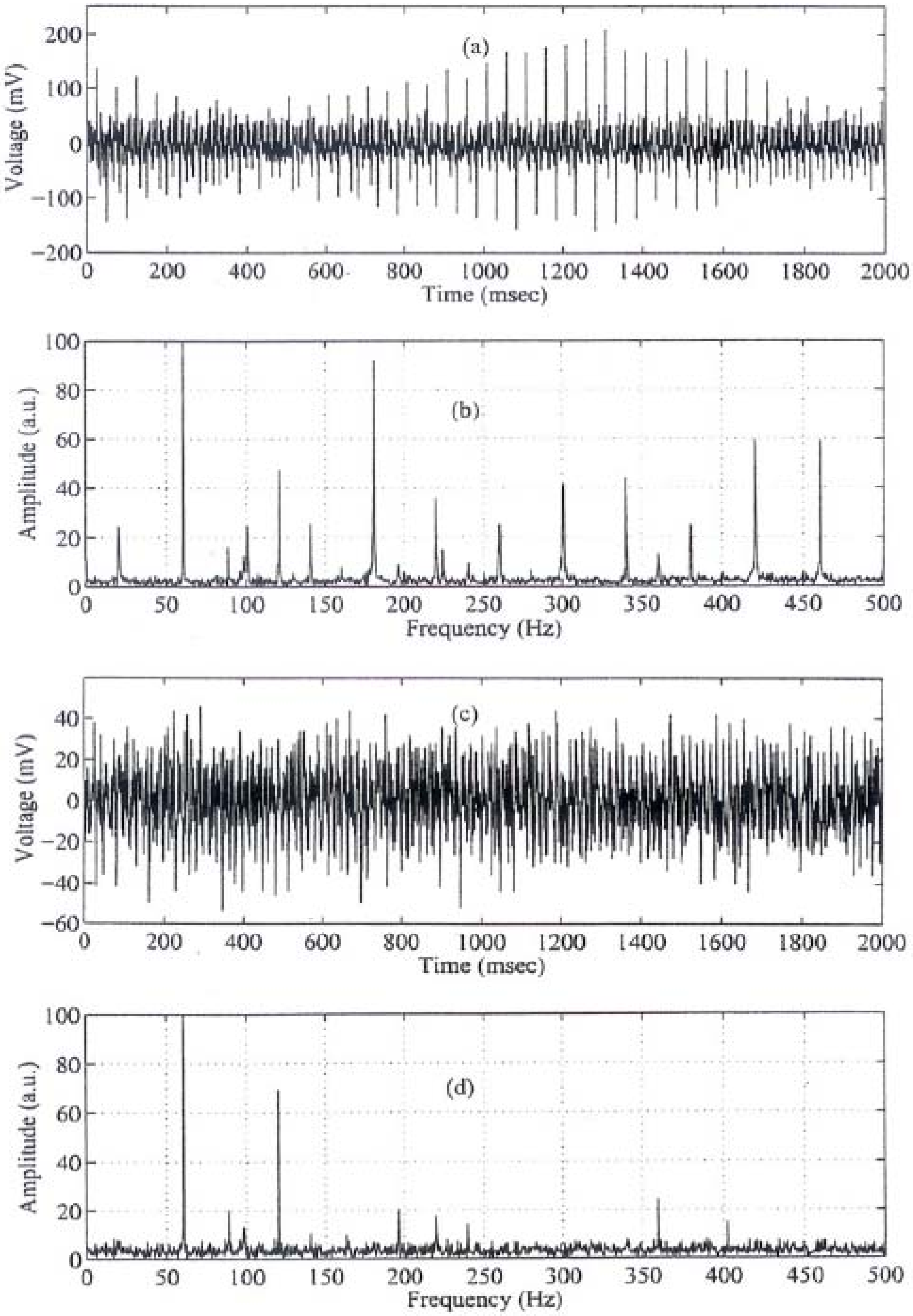

Figure 3-4. Noise from room light. (a) Noise when the room light was on. The rms noise value was 33.6 mV. (b) The spectrum of (a). (c) Noise when the room light was off. The rms noise value was 10.4 mV. (d) The spectrum of (c).

Water-vapor Removal

With free space propagation of the THz beam, interaction with ambient water vapor in the air becomes a significant factor in signal quality. The propagation of THz beams through water vapor was already discussed and yielded the absorption and dispersion of water vapor as a function of frequency in previous papers [17, 20]. Like other spectroscopy systems, to generate a clean output spectrum, the THz system was located in the airtight dry box and supplied with dry air through a Balston 75-62 FT-IR Purge Gas Generator. After about 5 minutes of receiving dry air, the humidity dropped to below 5%, which was measured using a Fisher Scientific Model 11-661-7B digital hydrometer. The working range of this hydrometer is 5% to 95% relative humidity.

A. Thin Film Measurement

Magnitude and Phase Shift

Recently, non-polar polymers such as low and high density polyethylene thin films have become of interest to the microelectronics industry as insulators in microelectronic devices [35] and have a common use as transmissive optical materials in the far infrared [36] because of their relatively low dielectric constant and easy processability. In order to make a meaningful fundamental investigation or to fabricate useful devices (capacitors, for example), many of the electrical properties of the dielectric thin films must be known.

Using THz-TDS, the absorption and dispersion of thin films can be measured. The optical absorption of thin films is influenced by interference effects. Thus the field distribution as a result of the standing wave within the thin plastic film must be known. The transmission equation of the thin sample has already been discussed by previous researchers [21, 22]. Figure 3-5 illustrates the multiple reflections and refractions of the THz beam in a thin parallel film. The THz beam enters a dielectric thin film from air at normal incidence (Figure 3-5 shows non-normal incidence for the purpose of display) and generates multiple reflections and refractions.

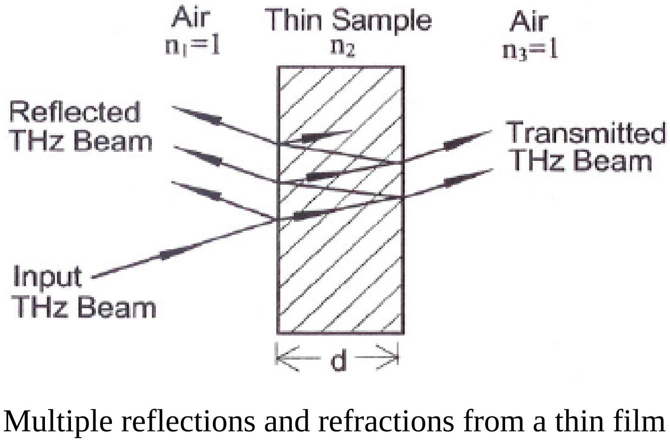

Figure 3-5. Multiple reflections and refractions from a thin film

The total transmission of a free standing absorptive thin film at normal incidence is given by [21]

$$t_{tot} = \frac{t_{12}t_{23}\exp(-\alpha d/2)\exp(i\beta_o)}{1 + r_{12}r_{23}\exp(-\alpha d)\exp(i2\beta_o)} \tag{3-1}$$

where α is an absorption coefficient, and $\beta_o = 2\pi n_2 d/\lambda_o$. λ_o is the free space wavelength. The reflection and transmission coefficients r and t are $r_{12} = (n_1 - n_2)/(n_1 + n_2)$, $r_{23} = (n_2 - n_3)/(n_2 + n_3)$, $t_{12} = 2n_1/(n_1 + n_2)$, and $t_{23} = 2n_2/(n_2 + n_3)$. By numerical calculation (See Appendix A), the total transmission is

$$t_{tot} = \frac{t_{12}t_{23}\exp(-\alpha d/2)\exp(i\beta_o)\exp(i\phi)}{\left(1 + r_{12}^2 r_{23}^2\exp(-2\alpha d) + 2r_{12}r_{23}\exp(-\alpha d)\cos(2\beta_o)\right)^{1/2}} \tag{3-2}$$

In this case $n_3 = n_1$ and $r_{12} = -r_{23}$. Then, we can express the magnitude and phase terms as in the equations below (See Appendix A).

$$|t_{tot}| \approx \frac{t_{12}t_{21}}{\sqrt{D}}\left[1 - \frac{\frac{\alpha d}{2}\left(1 - r_{12}^4\right)}{D}\right] \tag{3-3}$$

$$\tan\phi \approx r_{12}^2\sin(2\beta_o) \tag{3-4}$$

Where $D = 1 + r_{12}^4 - 2r_{12}^2\cos(2\beta_o)$. From equations (3-3) and (3-4), the power absorption coefficient and the index of refraction are

$$\alpha = \frac{2}{d}\frac{\left(1 - \frac{|t_{tot}|}{t_{12}t_{21}/\sqrt{D}}\right)D}{1 - r_{12}^4} \tag{3-5}$$

$$n_2 = n_1 + \frac{(\Delta\phi - \phi)c}{2\pi f d} \tag{3-6}$$

where $\Delta\phi$ is phase difference between with-sample and without-sample and c is speed of light.

Power Absorption

The thickness of the low density polyethylene film obtained from National Bag (sample #88-433A7) is 86 μm ± 2.3% as measured by micrometer (Mitutoyo model 193-111). A measured THz pulse without the film is shown in Figure 3-6 (a) and Figure 3-6 (b) shows the THz pulse transmitted through the plastic film. The output THz pulse, Figure 3-6 (b), has multiple reflections. The spectra of the THz pulses are shown in figure 3-6 (c). The solid line is the spectrum of the THz pulse with no sample (input) and the dashed line is the spectrum of the THz pulse with the sample (output). The ratio between the amplitude of the input spectrum and the amplitude of the output spectrum is frequency-dependent.

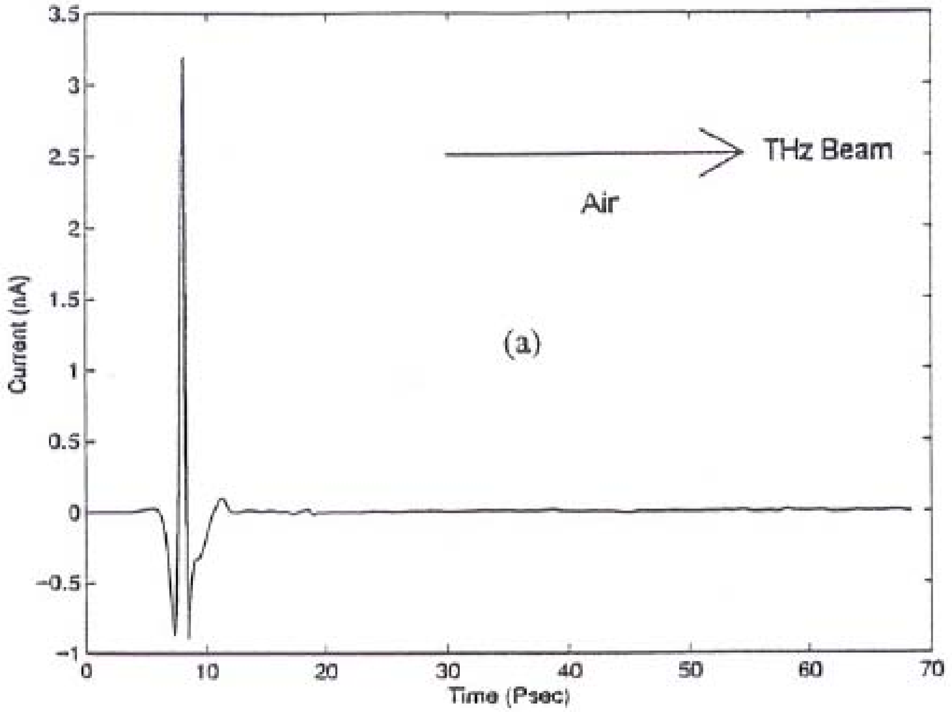

Figure 3-6 (a) Measured THz pulse with no sample.

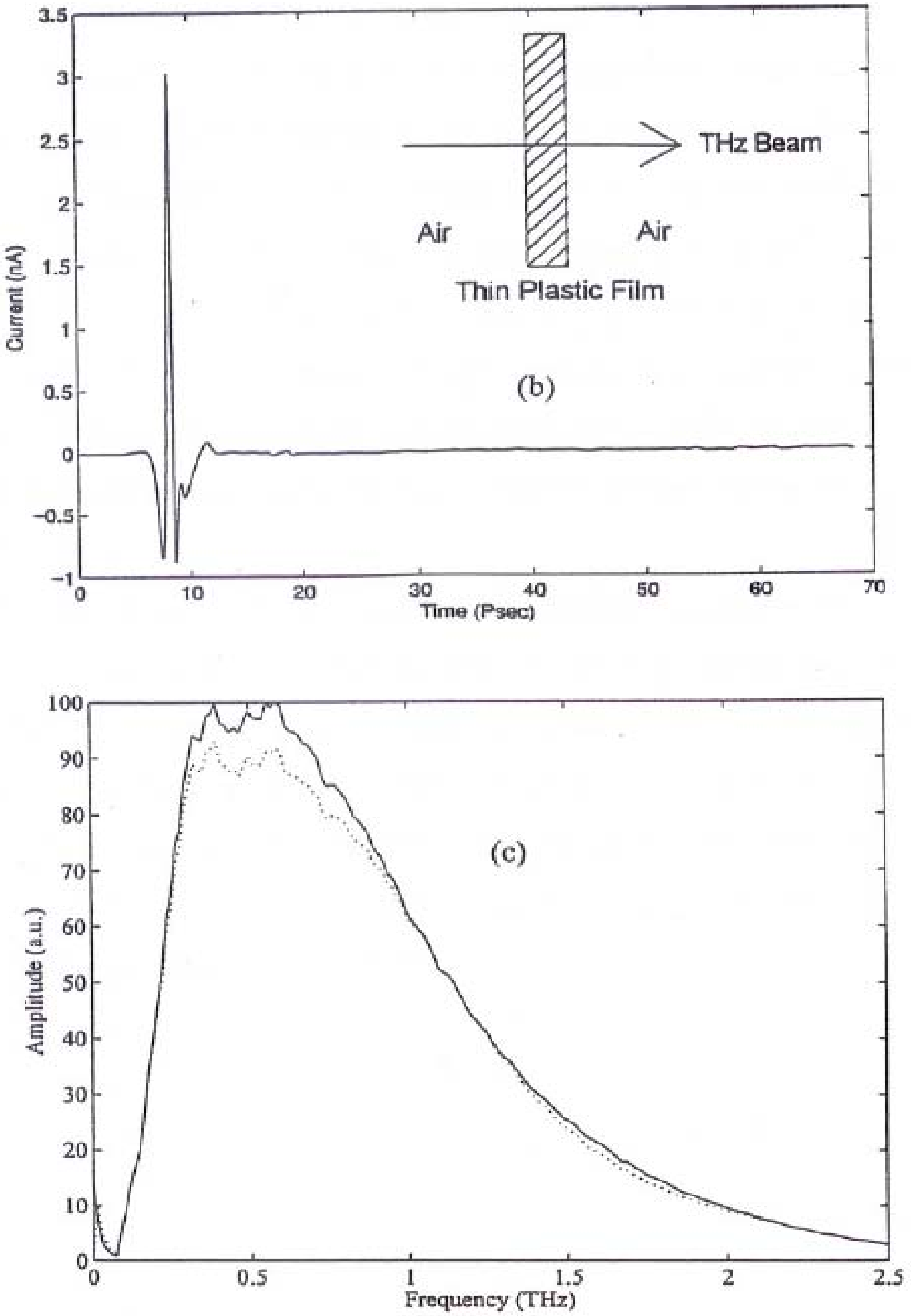

Figure 3-6 (b) Measured THz pulse transmitted through the thin plastic film. (c) Compare two spectra; Solid line is spectrum of (a) and dashed line is spectrum of (b).

Therefore the magnitude of total transmission, shown in Figure 3-7, is strongly frequency-dependent. The solid line is the experimental curve, which is calculated from the spectrum with sample divided by the spectrum without sample. The dotted line is the theoretical magnitude shift which is from $t_{12}t_{21}/\sqrt{D}$. The two curves fit very well. Because the magnitude shift is strongly frequency-dependent, the power absorption is also strongly frequency-dependent without the multiple effect of reflection. The dashed line of Figure 3-8 shows the power absorption without the multiple reflections. When the multiple reflections are considered, the calculated power absorption (by equation (3-5)) almost approaches the transparency of the thin film as shown in the solid line of Figure 3-8.

The amplitude of the measured output THz pulse is reduced compared with the input THz pulse because the sample is very thin with small power absorption. Also the sample does not have a uniform thickness. Therefore the measured power absorption is not a clean result but is in good agreement with the previous measurement (x marks as shown in Figure 3-8) [24, 32]. The measured power absorption of the low density polyethylene thin firm is less than 2 cm^{-1} for 0.1 to 2.5 THz frequency range and increases slightly with increasing the frequency.

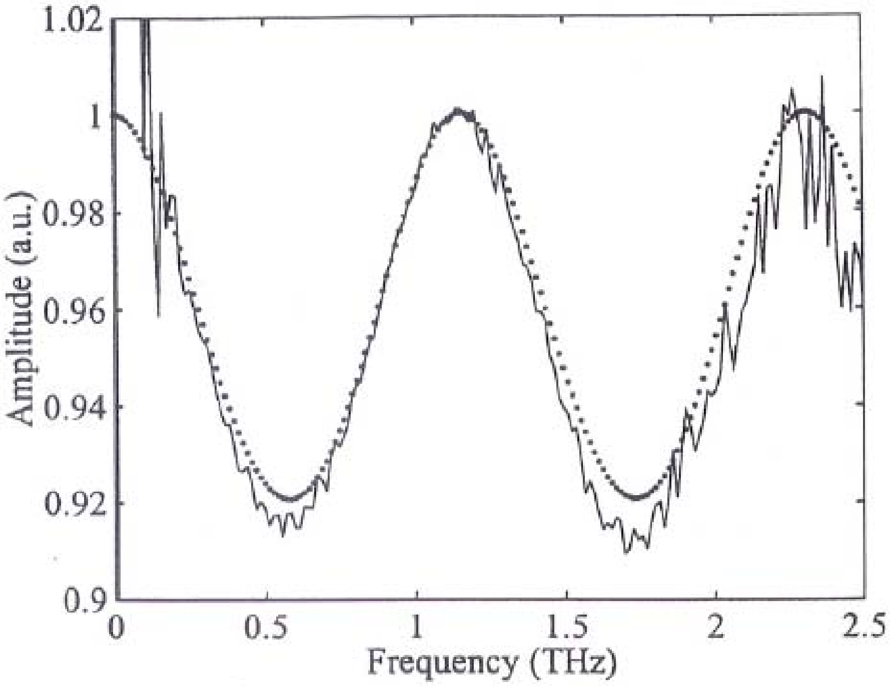

Figure 3-7. The measurement (Solid line) and theory (Dotted line) of the magnitude of total transmission.

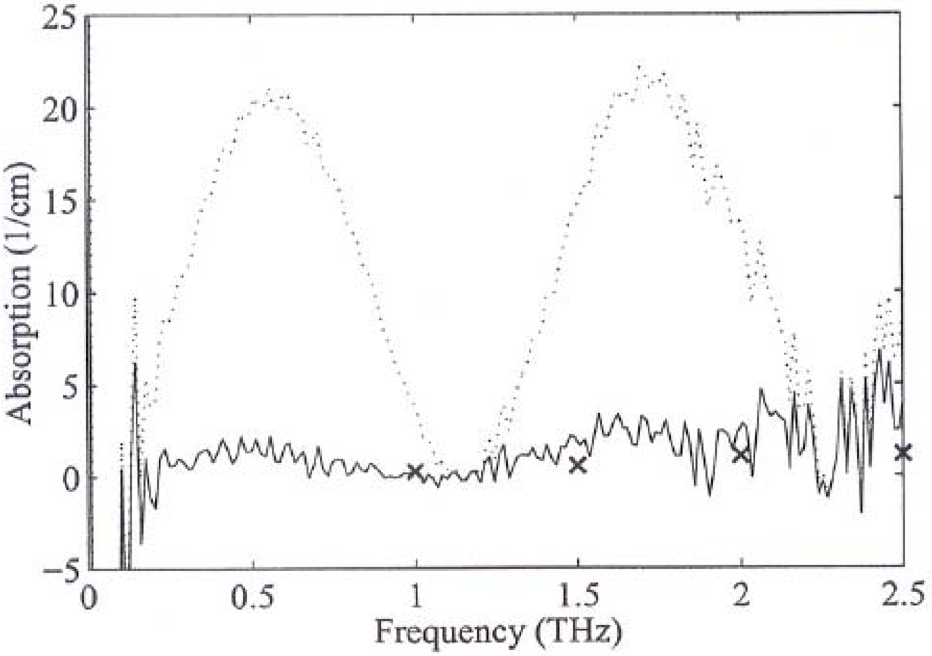

Figure 3-8. Power Absorption; Data analysis with multiple reflections (Solid line) and without multiple reflections (Dashed line). Previous measurement on low density polyethylene of Ref. 32 (x marks).

Index of Refraction

Because of the multiple reflections the phase change as shown in Equation (3-6) is strongly frequency-dependent. The measured phase difference between with-sample and without-sample is also frequency-dependent. The measured phase difference is the combination of the phase difference caused by the sample and phase shift due to the multiple reflections. To compare the theoretical phase shift and the measured extra phase shift, the measured phase difference is numerically shifted around 0 rad by subtracting (f × 0.917), where f is the frequency in THz. These relations are shown in Figure 3-9. The solid line is the measured phase term and the dotted line is the theoretical phase term. The two lines agree quite well. Figure 3-10 shows the ordinary phase difference (dotted line) and corrected phase difference (solid line). The calculated index of refraction is shown in Figure 3-11, where the solid line is after phase correction and the dotted line is before phase correction. The corrected index of refraction has a uniform index of refraction and its value is around 1.51 which is in good agreement with literature values [33, 34].

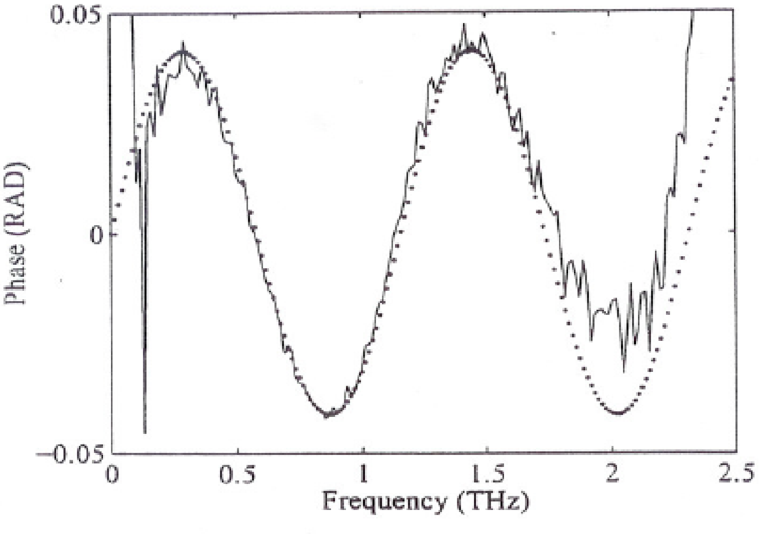

Figure 3-9. The measurement (Solid line) and theory (Dotted line) of the phase difference.

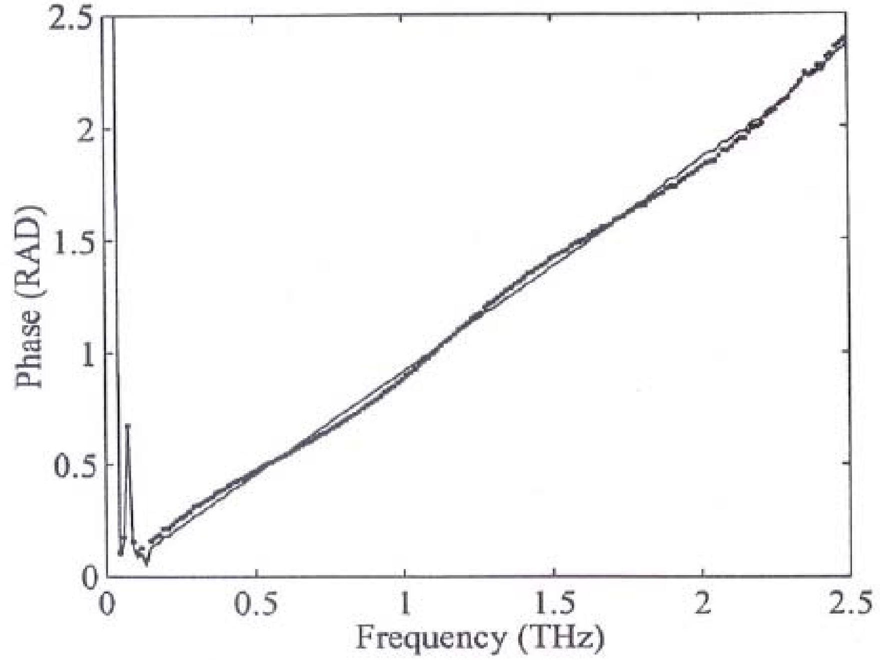

Figure 3-10. Before (dotted line) and after (Solid line) phase shift.

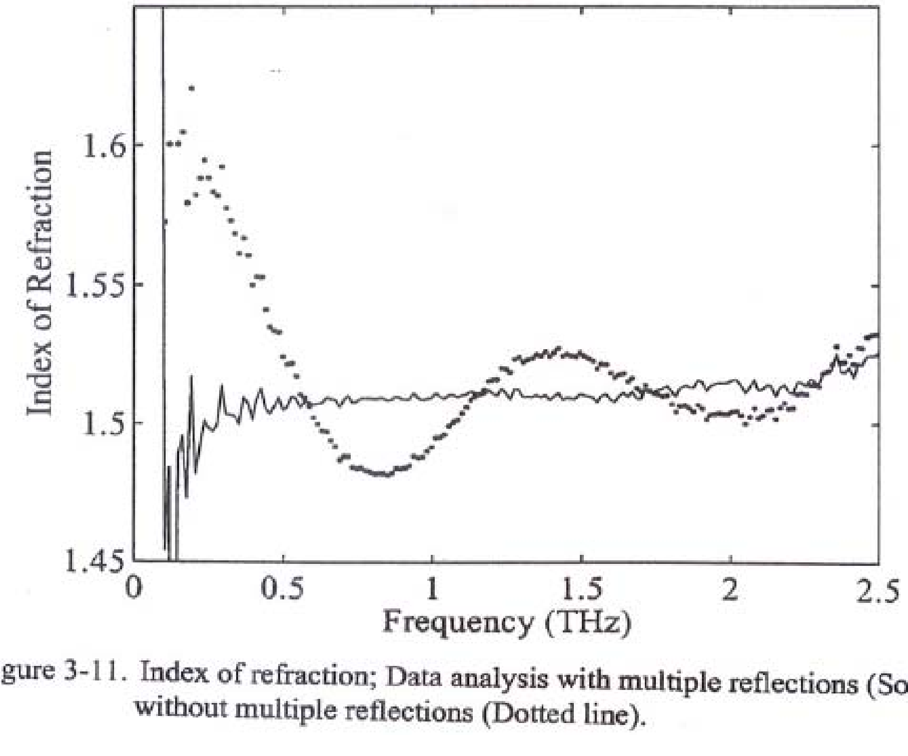

Figure 3-11. Index of refraction; Data analysis with multiple reflections (Solid line) and without multiple reflections (Dotted line).

Conclusions of the Thin Film Measurement

In this thin film measurement, I used the THz-TDS method to extract the power absorption and index of refraction of the thin film from the transmitted THz pulse measurement. Because this technique is contactless and gives frequency dependent results, the electrical properties of the thin films can be precisely measured. This method can be used to measure the physical properties of the other thin samples; for example the measurement of air gap thickness between two materials.

In this thin film measurement, the multiple reflection theory was used. The magnitude and phase shifts caused by the multiple reflections for the thin sample were introduced. The measured and calculated magnitude and phase shifts of the transmission were well fit. The magnitude and phase shifts were strongly frequency-dependent. Because the measured magnitude of the total transmission and the calculated magnitude shift were very well fit, the ratio between the measurement and theory was frequency-independent (around 1). Therefore the power absorption as written in Equation 3-5 becomes frequency-independent with very small values (less than 2 cm^{-1}).

The index of refraction was also frequency-independent. In the calculations of the magnitude and phase shifts, the index of refraction used was 1.51. The measured index of refraction of our thin film was also around 1.51 as shown in Figure 3-11 in solid line. The assumed and measured indexes of refraction were in good agreement.

The measured power absorption and the index of refraction were in good agreement with the literature values [24, 33, 34]. The power absorption in the previous measurement [24, 32] as shown in x marks in Figure 3-8 was slowly increasing with increasing the THz frequency and its values did not exceed 1.5 cm^{-1} at 2.5 THz. This result was similar to our measurement. In the room temperature the measured index of refraction was in good agreement between our THz-TDS measurement and the previous measurement [33, 34].

B Reflection Measurement of Doped Silicon

Introduction

For several decades physicists have studied the dynamics of carriers in semiconductors. The various electrical methods for determining the carrier concentration, mobility, and resistivity of semiconductors were adequately described and discussed in the previous literature. [1-4] Of all the requirements for making electrical measurements, the one that is most often difficult to satisfy is fabrication of a suitable electrical contact. These electrical measurements cannot precisely measure the electrical properties, due to the Schottky barrier at the metal and semiconductor interface. However, the TDS techniques have the important advantage that it is not necessary to physically contact the sample in order to measure its properties.

A powerful THz-TDS transmission technique has been available for studies of the electrical properties of semiconductors. [7-9] In this technique two THz pulse shapes are measured: the input pulse and the output pulse which is the transmission of the semiconductor sample. In order to measure the output THz pulse, there is a thickness limitation. The low resistivity semiconductor samples (high carrier density) should be extremely thin semiconductor wafers (several μm thicknesses) to detect the output signal because they strongly absorb THz radiation. Therefore the THz-TDS transmission measurement cannot measure the electrical properties of the thick semiconductor samples. However, transient THz reflection spectroscopy has no thickness limitation of the samples because this technique measures only the reflected THz pulse from the surface of the samples.

This section describes the application of THz reflection spectroscopy to the measurement of THz pulses reflected from doped Si wafer surface. Using this method, I am able to measure changes in the amplitude and phase of the THz pulse reflected from Si surface.

Experimental Setup

The THz radiation radar system was recently developed [19]. The THz reflection from a doped silicon sample was first investigated by the THz radiation radar system.

The flat deflecting mirrors which have 5.1 cm diameter are installed at the middle of the two paraboloidal mirrors. The deflecting mirrors are 9.5 cm from the center of the paraboloidal mirrors, and the target is 9.5 cm from the deflecting mirrors as shown in Figure 3-12. Because the THz beam is not perpendicular to the target sample, the edge of the sample holder is cut to remove the THz loss from the sample holder. A helium neon laser aligned coincident with the THz beam permits accurate positioning of the target.

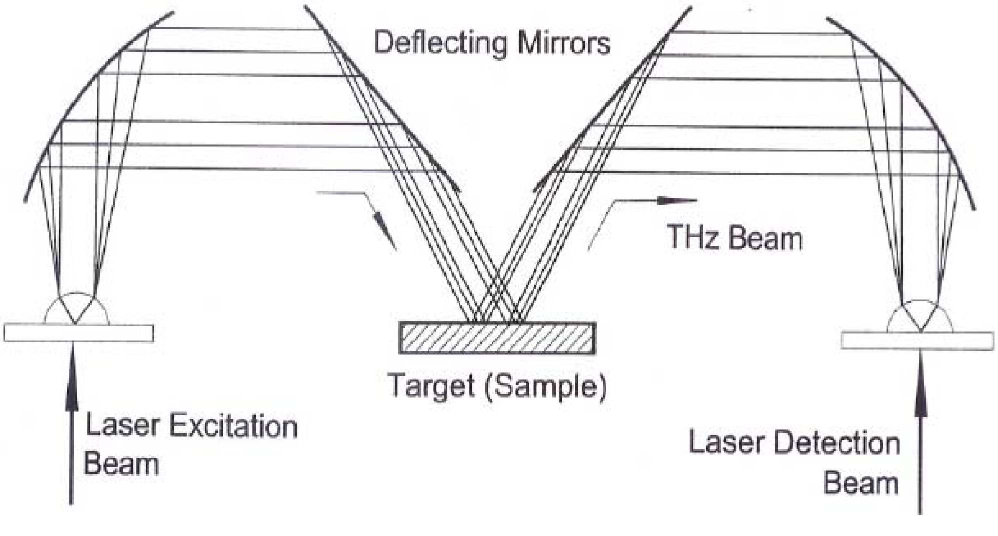

Figure 3-12. THz beam system used for reflected THz pulse measurement.

Theory for Reflection

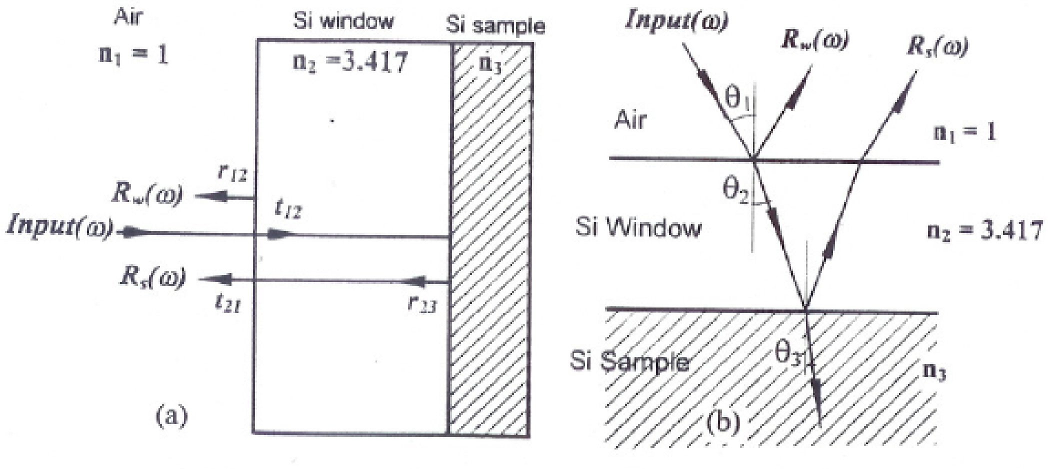

Figure 3-13. Reflection of the incident THz beam from target (sample) (a) Perpendicular to the plan of target; (b) Incident angle to the plan of target.

In this reflection measurement, two THz pulse shapes are measured: the input pulse and the output pulse that are before and after reflection from Si sample respectively. The measurement of the input THz pulse is very difficult because it requires the exact same geometrical conditions between the input and output measurements. The amplitude of the THz signal is very sensitive to the incident angle. Therefore I measured two reflected THz pulses (R_w and R_s) without any physical movement by attaching the Si window to the Si sample as shown in Figure 3-13. The amplitude reflection from the Si window (R_w) and the amplitude reflection from the Si sample (R_s) are given by

$$R_w(\omega) = Input(\omega) \cdot r_{12} \tag{3-7}$$

$$R_s(\omega) = Input(\omega) \cdot t_{12} \cdot \left|R_{23}\right| \cdot t_{21} \tag{3-8}$$

where t_{12} is the transmission coefficient from air to the Si window and t_{21} is the transmission coefficient from the Si window to air. r_{12} is the reflection coefficient from the interface between air and the Si window and $\left|R_{23}\right|$ is the magnitude reflection coefficient from the interface between the Si window and the Si sample. Because of the very small power absorption by the Si window [8], absorption by the Si window is neglected.

In the experimental setup (Figure 3-12), the incident THz beam is not perpendicular to the surface of the Si window as shown in Figure 3-13(b). Therefore the incident THz beam has an incident angle θ_1 which is 21.6° in this setup. By Snell's law, the reflected beam angle θ_2 with respect to the perpendicular direction of the Si window surface is 6.2°. The reflection coefficient r_{12} and the transmission coefficient t_{12} and t_{21} are given by

$$r_{12} = \frac{n_1 \cos\theta_1 - n_2 \cos\theta_2}{n_1 \cos\theta_1 + n_2 \cos\theta_2} = -0.57 \tag{3-9}$$

$$t_{12} = \frac{2n_1 \cos\theta_1}{n_1 \cos\theta_1 + n_2 \cos\theta_2} = 0.43 \tag{3-10}$$

$$t_{21} = \frac{2n_2 \cos\theta_2}{n_1 \cos\theta_1 + n_2 \cos\theta_2} = 1.57 \tag{3-11}$$

where n_1 and n_2 are index of refraction of air and the Si window respectively.

The amplitude ratio of the measurements between the reflection from the Si window and the reflection from the Si sample can be written as

$$\frac{R_s}{R_w} = \frac{Input(\omega) \cdot t_{12} \cdot |R_{23}| \cdot t_{21}}{Input(\omega) \cdot r_{12}} \tag{3-12}$$

Therefore the measured reflection coefficient from the interface between the Si window and the Si sample yields

$$|R_{23}| = \frac{r_{12}}{t_{12}t_{21}} \cdot \frac{R_s}{R_w} = 0.84\frac{R_s}{R_w} \tag{3-13}$$

When the incident THz beam is perpendicular to the surface of the Si window, as shown in Figure 3-13 (a), the theoretical calculation of the reflection coefficient from the interface between the Si window and the Si sample is given by

$$r_{\perp 23} = \frac{n_2 - n_3}{n_2 + n_3}$$

where n_3 is index of refraction of Si sample and $n_3 = n_r + i\, n_i$.

Therefore
$$r_{\perp 23} = \frac{\left(n_2 - n_r\right) - in_i}{\left(n_2 + n_r\right) + in_i} \tag{3-14}$$

$$r_{\perp 23} = -\frac{\left(n_r^2 + n_i^2 - n_2^2\right) + i2n_i n_2}{n_2^2 + 2n_2 n_r + n_r^2 + n_i^2} \tag{3-15}$$

The reflection coefficient can be expressed by its magnitude and phase as $r_{\perp 23} = \left| R_{\perp 23} \right| \exp\left(i\phi_{\perp 23}\right)$. Therefore the calculated reflection coefficient from the interface between the Si window and the Si sample yields

$$\left|R_{\perp 23}\right| = \left[\frac{\left(n_r^2 + n_i^2 - n_2^2\right)^2 + 4\left(n_i n_2\right)^2}{\left(n_2^2 + 2n_2 n_r + n_r^2 + n_i^2\right)^2}\right]^{\frac{1}{2}} \tag{3-16}$$

$$\phi_{\perp 23} = \tan^{-1}\left(\frac{2n_i n_2}{n_r^2 + n_i^2 - n_2^2}\right) \tag{3-17}$$

But in this measurement the incident beam is not perpendicular to the surface of the Si window, so the reflection coefficient r_{23} is given by

$$r_{23} = \frac{n_2 \cos\theta_2 - n_3 \cos\theta_3}{n_2 \cos\theta_2 + n_3 \cos\theta_3} \tag{3-18}$$

where θ_3 is the reflected THz beam angle in the Si sample.

By the same process, the magnitude $|R_{23}|$ and the phase ϕ_{23} terms are given by

$$\left|R_{23}\right| = \left[\frac{\left(\left(n_r^2 + n_i^2\right)\cos^2\theta_3 - n_2^2\cos^2\theta_2\right)^2 + 4\left(n_i n_2 \cos\theta_2 \cos\theta_3\right)^2}{\left(n_2^2\cos^2\theta_2 + 2n_2 n_r \cos\theta_2\cos\theta_3 + \left(n_r^2 + n_i^2\right)\cos^2\theta_3\right)^2} \right]^{\frac{1}{2}} \qquad (3\text{-}19)$$

$$\phi_{23} = \tan^{-1}\left(\frac{2n_i n_2 \cos\theta_2 \cos\theta_3}{\left(n_r^2 + n_i^2\right)\cos^2\theta_3 - n_2^2\cos^2\theta_2} \right) \qquad (3\text{-}20)$$

where n_r and n_i can be determined by plasma frequency $\omega_p/2\pi$ and damping rate $\Gamma/2\pi$ (see Chapter IV Drude Theory).

Silicon Sample Measurement

In order to test the measurement and the theory, the two reflected THz pulses, R_w and R_s, are measured without a Si sample where R_w is the amplitude reflection from the interface between air and the front side surface of the Si window and R_s is the amplitude reflection from the interface between the back side surface of the Si window and air. The two measured reflected THz pulses are shown in Figure 3-14 (a) and (b). Because of the reflection from the high index of refraction (Si window) to the low index of refraction (air), the polarity of R_s when compared to the polarity of R_w is changed. Figure 3-14 (c) shows the amplitude spectra of the two reflected THz pulses and its ratio is shown in Figure 3-14 (d). Because of the noise amplitude ratio, an approximation is taken. In this measurement, the angle θ_3 is the same as the angle θ_1 because both sides of the Si window have the same index of refraction (air). The magnitude of the reflection coefficient $|R_{23}|$ is 0.57 by Equation (3-18). In the high frequency range, the measurement is higher than the theory. Therefore the correction factor should be used with the Si sample measurement.

When the Si window and the Si sample are attached, there are some air gaps between the two materials because the two materials are not flat. By an interferometer measurement, there is about 4 μm difference between minimum and maximum height. Since the power absorption of the Si window is very small, the multiple reflections from these air gaps change the amplitude of the output THz pulse. We can determine the average air gap between the two materials from the data fitting to the measurement. The multiple reflection coefficient R can be calculated by the multiple transmission coefficient T as shown below.

$$R = 1 - T \tag{3-21}$$

By Equation (3-2) and (3-3), the multiple reflection coefficient is

$$R = 1 - \frac{t_{12} t_{21}}{\sqrt{1 + r_{12}^4 - 2 r_{12}^2 \cos(2\beta_o)}} \tag{3-22}$$

where $\beta_o = 2\pi n_2 d/\lambda_o$. λ_o is the free space wavelength, n_2 is index of refraction of air, and d is thickness of the air gap. Finally, by data fitting, I can determine that there is a 7 μm air gap between the two materials. Figure 3-14 (e) shows the multiple reflection coefficients for a 7 μm air gap between two Si windows. Figure 3-14 (f) shows the multiple reflection coefficients and the difference between the measurement and the theory of Si window measurement (correction factor) from 0 to 2.5 THz frequency range.

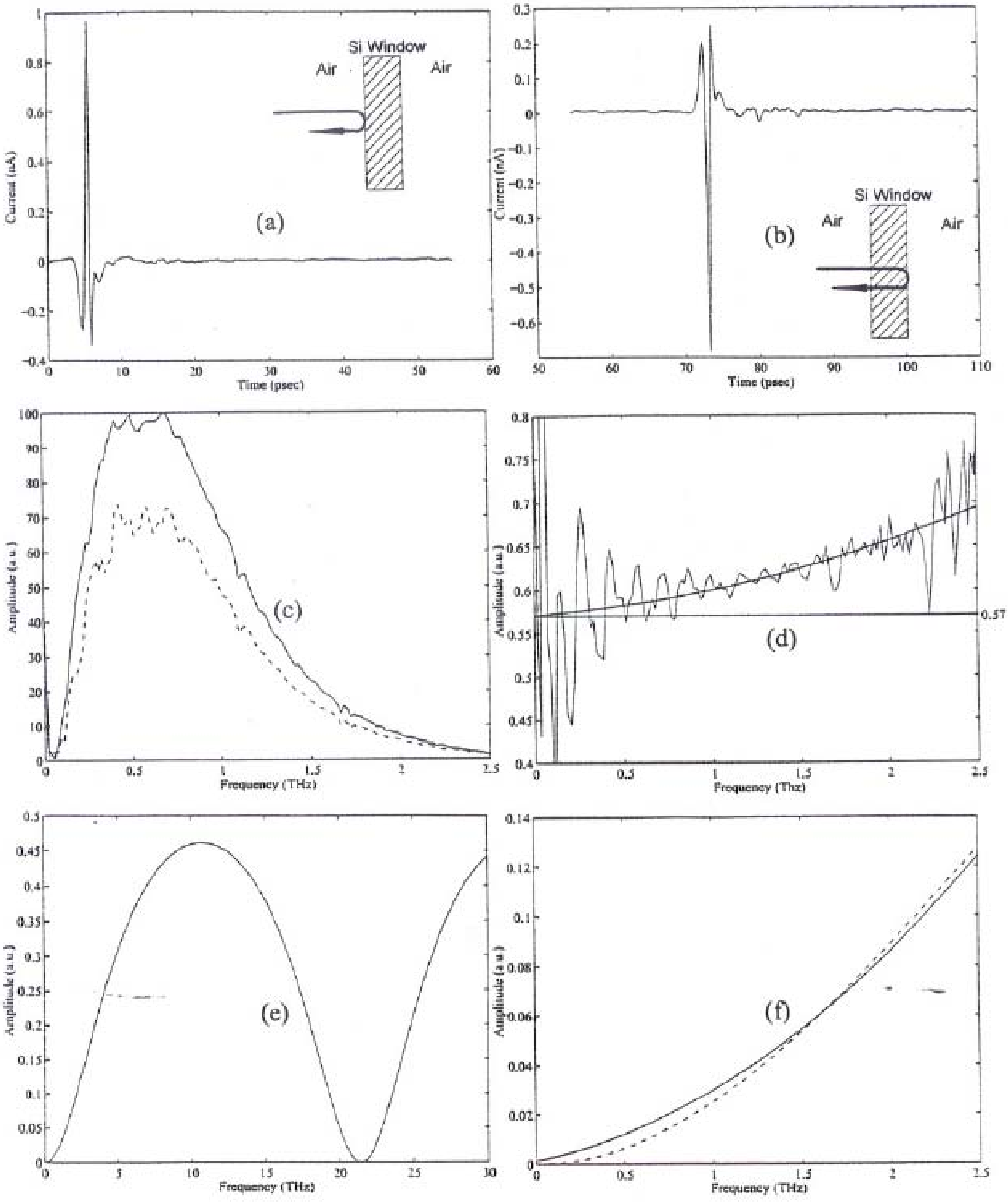

Figure 3-14. (a) Reflected THz pulse from air to Si window. (b) Reflected THz pulse from Si window to air. (c) Compare two amplitude spectra; solid line (spectrum of (a)) and dashed line (spectrum of (b)). (d) Ratio of (c) and its approximation curve. (e) Multiple reflection coefficient between two Si windows. (f) solid line: correction factor & dashed line: zoom of (e).

The measured sample is 0.2 Ω cm, *n*-type silicon from Virginia Semiconductor Inc. Figure 3-15 (a) shows the THz pulse R_w reflected by the interface between air and the front side of the Si window. Consistent with the reflection coefficient (r_{12}=0.57), the peak THz pulse is reduced by about 50% compared with that of the input THz pulse. The normalized amplitude spectrum of the reflected THz pulse is shown in Figure 3-15 (b). The THz pulse R_s reflected by the interface between the back side of the Si window and the Si sample is shown in Figure 3-15 (c). The peak THz pulse is reduced to 0.37 nA. Because of the thick Si window, the round trip THz pulse in the Si window has a time delay of about 67.8 psec. Therefore, the reflected THz pulse from the sample is numerically shifted by -67.8 psec in order to measure the phase difference caused by the reflection from the interface between the Si window and the doped Si sample. Figure 3-15 (d) shows the normalized amplitude spectrum of the reflected THz pulse from the sample. Figure 3-15 (e) shows the phases of the two reflected THz pulses where the solid line describes the phase of the incident THz pulse to the Si sample and the dashed line describes the phase of the reflected THz pulse from the Si sample surface. Figure 3-15 (f) shows the relative amplitude of the two spectra. The solid line and dashed line describe the THz pulse incident to and reflected from the Si sample.

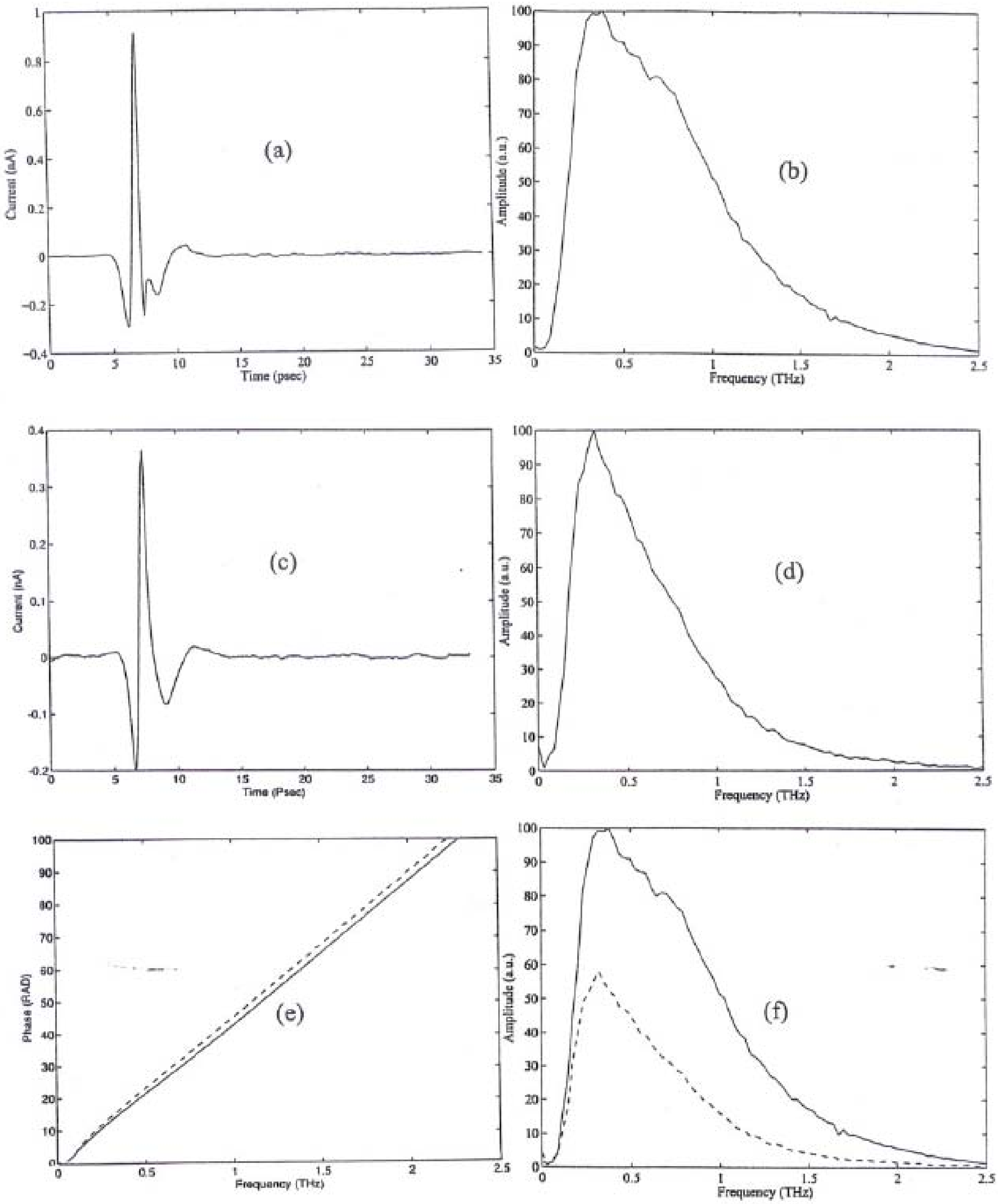

Figure 3-15. Measured reflected THz pulse (a) reflected THz pulse from Si window; (b) normalized amplitude spectrum of (a); (c) reflected THz pulse from Si sample; (d) normalized amplitude spectrum of (c); (e) phase difference : solid line (Phase of (c)) and dashed line (phase of (a)); (f) compare two amplitude spectra : Solid line (amplitude of (a)) and dashed line (amplitude of (c)).

Data Analysis

After multiplying the transmission and the reflection coefficients by the measured amplitude ratio, the magnitude of the reflection from the sample surface does not fit the theory as shown in Equation 3-19. The measurement and the theory are in disagreement especially in the high frequency range. Therefore we should consider the correction factor and the air gap between the Si window and Si sample. After subtracting the correction factor from the measurement and adding the extra multiple reflection coefficients by the air gap to the theory, the measurement and theory curves are in excellent agreement as shown in Figure 3-16 (a). The measured resistivity is 0.17 Ω cm which has two parameters; plasma frequency $\omega_p/2\pi = 3.3$ THz and damping rate $\Gamma/2\pi = 1$ THz. The phase difference caused by the reflected THz pulse from the interface between the Si window and the Si sample has good agreement for both the measurement (dots) and the theory (solid line) as shown in Figure 3-16 (b).

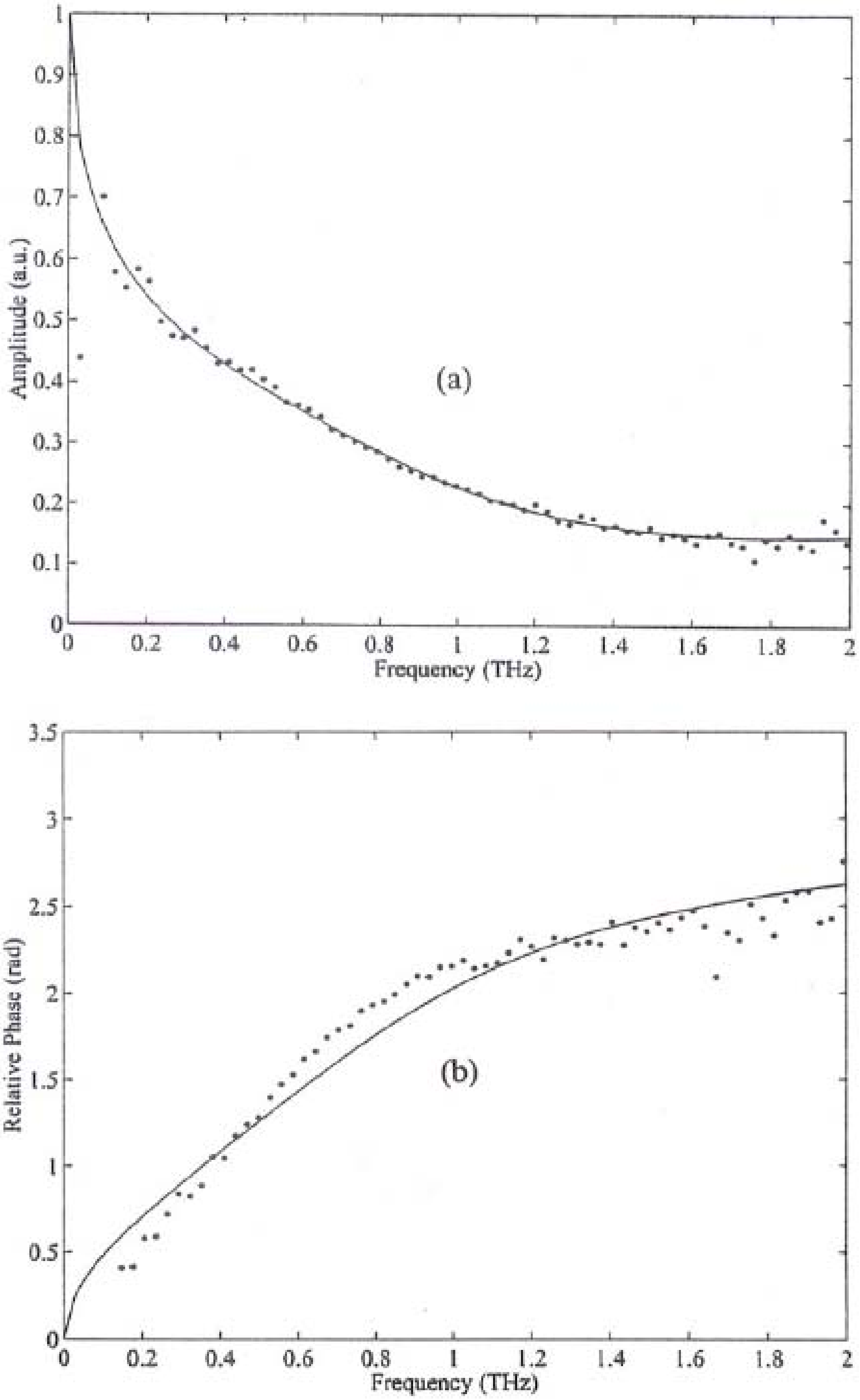

Figure 3-16. (a) Reflection coefficient $|R_{23}|$; theory (solid line) and measurement (dots).
(b) Phase difference ϕ_{23}; theory (solid line) and measurement (dots).

Conclusions of Reflection Measurement

Using the THz radar system, the THz reflection from the silicon surface is measured. From the simple reflection coefficient calculation, the frequency-dependent magnitude and phase difference of the reflection coefficient are measured. In the calculation of the theory, I neglect the Si window absorption since it is very small and consider the incident angle to the surface of the Si window. Because the measured reflection coefficient from the Si window is noisy, I take the smooth curve to calculate the correction factor. Therefore a new measurement of the reflection coefficient of the Si window is needed in the future.

The measured Si sample has 300 μm thickness at 0.2 Ωcm resistivity. Because of the thick wafer and low resistivity, the THz-TDS transmission measurement cannot detect the output signal. However, I can measure the amplitude and associated phase change of THz pulses upon reflection from the sample by this reflection measurement. In the data analysis, the carriers are treated as classical particles subjected to random collisions, and the reflected amplitude and phase change data are closely fit by adjusting the plasma frequency $\omega_p/2\pi = 3.3$ THz ± 3% and the damping rate $\Gamma/2\pi = 1$ THz ± 6%. By using the Drude model (see Chapter IV), the calculated properties of the Si sample are mobility $\mu = 1080\ \mathrm{cm^2/Vs} \pm 6\%$, carrier concentration $N = 3.5\times10^{16} \pm 6\%$, and resistivity $R = 0.17\ \Omega\mathrm{cm} \pm 2\%$. Using this analysis, I can determine the presence of a 7 μm air gap between the Si window and the Si sample. The air gap should be confirmed by another method in the future. The experiment described here shows the utility of measuring the optical and electronic properties of the Si sample nondestructively and without invasive contact.

C. Transmission Measurement of Doped Silicon

Removal of Reflected THz Pulses

The doped silicon sample is located at the middle of the two paraboloidal mirrors and the THz pulses transmitted through the sample. Because of the sample’s characteristics, the transmitted THz pulses change their amplitude shape and are delayed. The pulse sequence transmitted through the silicon sample is shown in Figure 3-17 (a), where the sample is 292 μm thick, 50 mm diameter, and 0.4 Ω cm *n* type silicon. The peak amplitude is reduced about 75% compared to that of the original pulse. The output pulse amplitude and shape are changed due to reflection loss, the frequency-dependent absorption, and dispersion of the sample [7, 11]. The second transient is a THz pulse reflected inside of the thin sample. The multiple reflections are responsible for the oscillations in the corresponding amplitude spectrum shown in Figure 3-17 (b). In the time domain, the position of the main pulse is 7.1 psec and the position of the second reflected THz pulse is 14.1 psec. In previous THz measurements these multiple reflections were numerically removed to facilitate interpretation of the data [7, 11]. As demonstrated in this work, the multiple reflections can be removed in the time domain by attaching silicon windows to both sides as shown in Figure 3-18. The silicon windows are 0.3-cm-thick, 5-cm-diameter, and high-resistivity (10-KΩ-cm). Undoped silicon is a good window material, owing to its almost complete transparency and lack of dispersion in the THz frequency range [8]. The pulse sequence transmitted through the silicon window, the silicon sample, and the other silicon window is shown in Figure 3-19 (a).

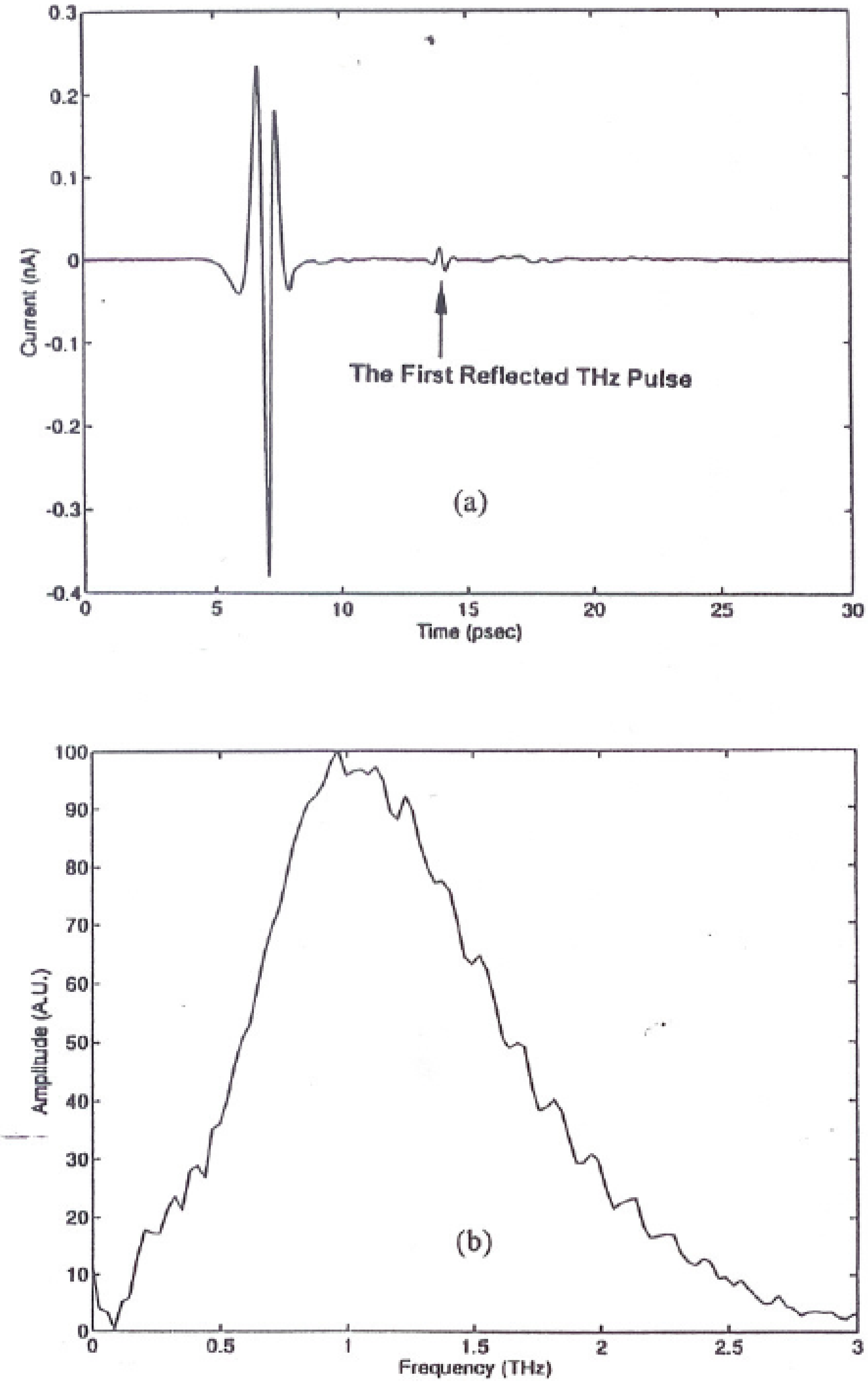

Figure 3-17 (a) THz pulse transmitted through a 292-μm-thick wafer of *n*-type silicon and its reflected THz pulse. (b) Amplitude of spectrum of (a).

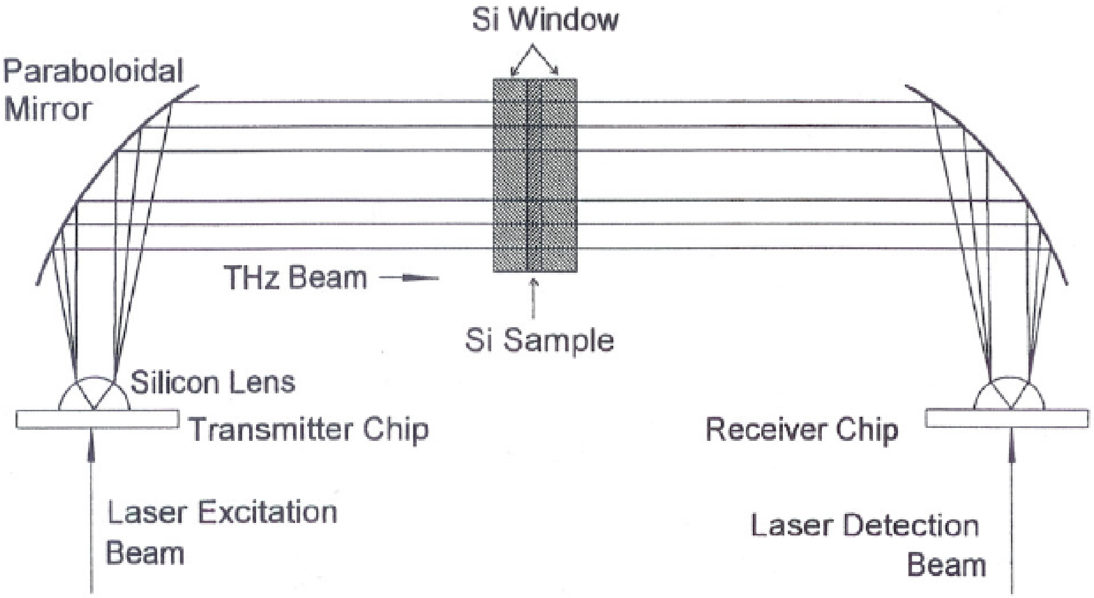

Figure 3-18. Silicon sample and silicon windows in the THz system to remove the reflected THz pulses

Now the reflected THz pulses travel a long distance. Therefore the reflected THz pulses disappear at their original position in the time domain. In this case the reflected THz pulses are delayed 143 psec from the main THz pulse. This time position is out of our measurement. In the time-domain, I usually measure the input and the output THz pulses over a 70 psec window. Figure 3-19 (b) shows the spectrum; it is clean compared to the previous spectrum.

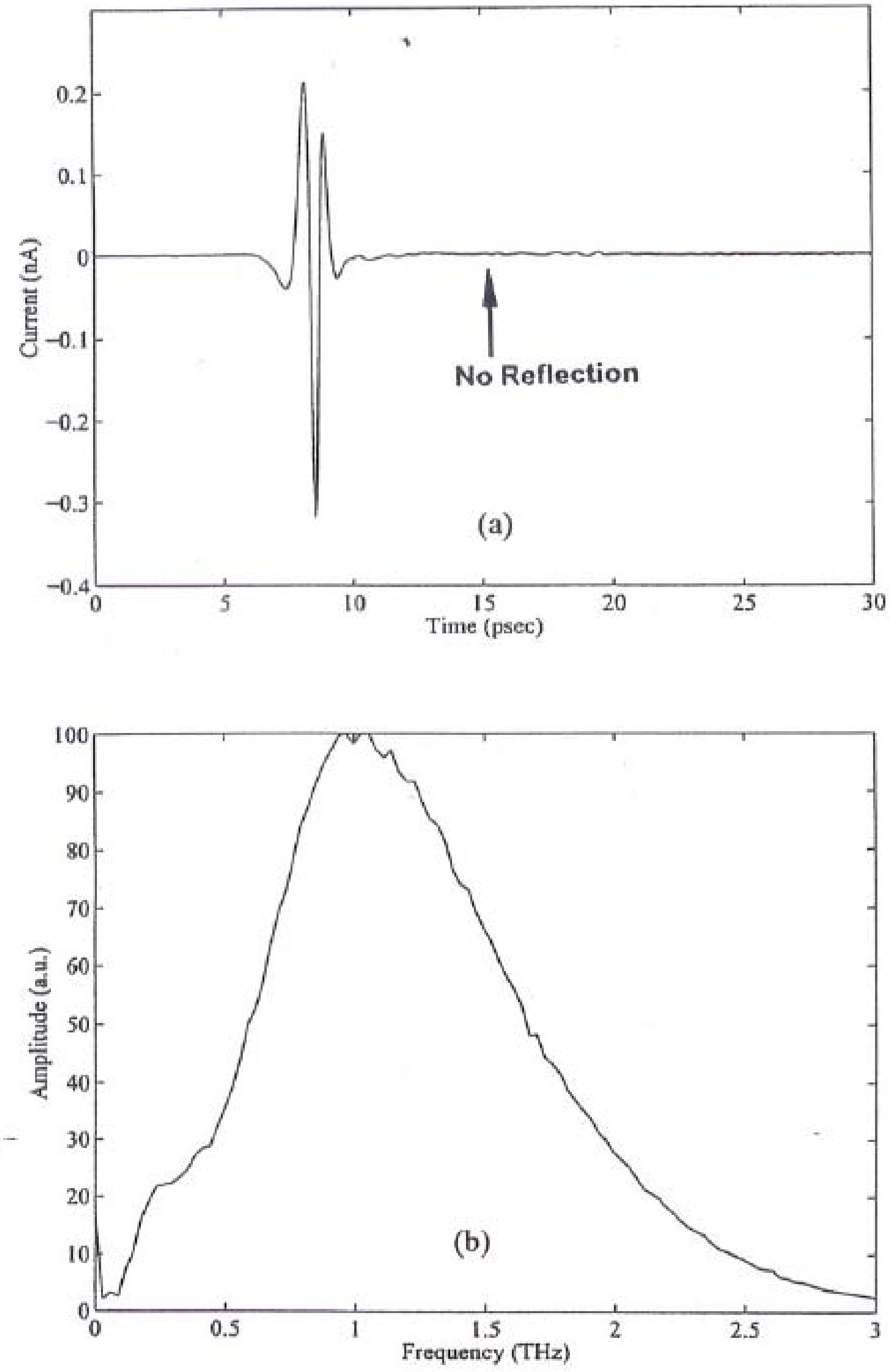

Figure 3-19. (a) THz pulse transmitted the silicon window, the silicon sample, and another silicon window. (b) Amplitude spectrum of (a).

Sample Holder

One important technique in using silicon windows is to remove the air gap between the sample and the windows. If there are air gaps in the interface, the THz beam has multiple reflections in the air gap. To avoid this problem, the silicon sample and the silicon windows have to be in very close contact.

Figure 3-20 (a, b) show the sample holder which is designed for this purpose. The silicon windows are squeezed from both sides by the four corner screws and, to avoid damage at the silicon windows, an ‘o’-ring is installed between the aluminum plate and the silicon windows. The whole sample holder can rotate to measure the reference THz pulse and the output THz pulse.

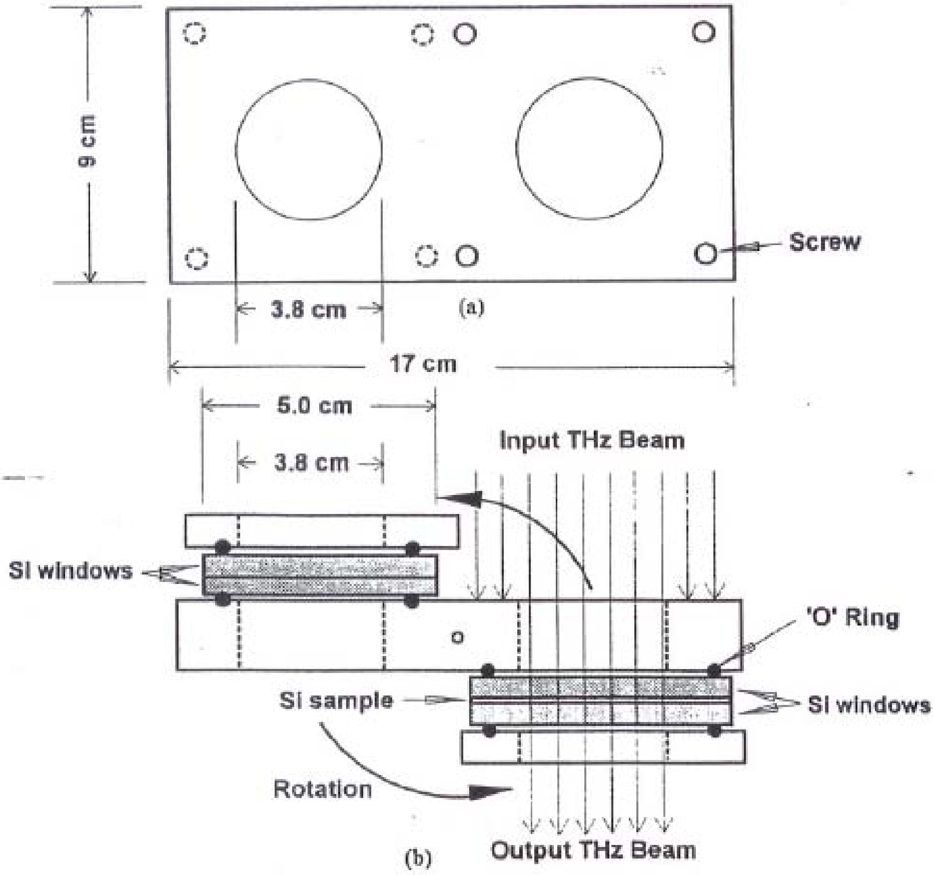

Figure 3-20. (a) Dimension of the sample holder. (b) Setup of the silicon sample, the silicon window and the sample holder (top down view).

Measurement of Silicon Samples

The measured samples were doped *n* type and *p* type silicon wafers with <100> orientation. Because of the large number of samples, only the THz pulses of the highest resistivity *n* type (8.15 Ω cm) sample will be shown in this section. The THz pulses of the other *n* and *p* type samples will be shown in Appendix B. All samples were doped with phosphorus (*n* type) or boron (*p* type). The specifications of silicon samples are shown in Table 1-1.

Sample No	**Orientation**	**Dopant**	**Type**	**Dia.**	**Manufac. Ω cm**	**4-Point R Ω cm**	**Thickness μm**
1894A	<100>±0.5°	Phosphorus	n	2"	10±30%	8.15±0.2%	5008±0.1%
950088702	<100>±0.5°	Phosphorus	n	2"	1.26±0.8%	1.31±1%	598±0.3%
4987	<100>±0.5°	Phosphorus	n	2"	0.4±20%	0.48±0.5%	292±0.7%
4986A	<100>±0.5°	Phosphorus	n	2"	0.2±20%	0.21±0.5%	199±0.5%
950088701	<100>±0.5°	Phosphorus	n	2"	0.1±20%		102±3.0%
950088703	<100>±0.5°	Phosphorus	n	2"	0.04	0.055±14%	56±4.0%
1895A	<100>±0.5°	Boron	p	2"	10±30%	9.61±0.4%	5013±0.1%
4989	<100>±0.5°	Boron	p	2"	0.4±20%	0.40±1%	296±0.8%
4988	<100>±0.5°	Boron	p	2"	0.2±20%	0.17±0.6%	204±0.5%

Table 1-1. Specifications of silicon samples. The resistivity values are from the manufacturer, Virginia Semiconductor Inc..

Two pulse shapes are measured by the THz-TDS technique: the reference pulse without a sample and the pulse after propagating through the sample. The magnitude of the transmitted pulse is reduced by the sample’s absorption. Also, the transmitted pulse has a time delay related to the sample's thickness and the index of refraction. Using Fourier analyses of the reference and output pulses, the frequency-dependent absorption and dispersion of the sample can be obtained.

Because the power absorption and dispersion of the highest resistivity *n* and *p* type samples have a very strong response at the low frequency ranges, the bowtie 30° transmitter chip is used to measure these low frequencies.

The phase difference between the reference and the output THz pulse is related to the calculation of dispersion. For very thick samples (5 mm thickness), the phase difference approaches 630 radians at 2.5 THz frequency (see Appendix II Figure B-2 (e)) and the low frequency phase shift is too large. Also, the low frequency phase data is too noisy below 0.1 THz because the THz pulses do not have enough power at these frequency ranges. The phase shift should start at zero radians but it is difficult to know that. Therefore, the theoretical calculated index of refraction is integrated to obtain the low frequency phase difference. Because the calculated phase difference is not linear, we can adjust our measurement to this phase difference.

GaAs 10-80-10 Transmitter and SOS 10-30-10 Receiver

Due to very low power absorption, the highest resistivity (8.15 Ω cm) *n* and *p* type sample have 5 mm thickness. This thickness is enough to delay the reflected THz pulses sufficiently; these samples do not need the silicon windows. Figure 3-21 (a) shows the THz pulse from 0 to 35 psec with no sample. The THz signal is an average of 9 scans to improve the signal-to-noise ratio. The corresponding amplitude spectrum of this 0.5 psec full width at half maximum (FWHM) pulse is presented in Figure 3-22 (a) solid line and illustrates the 2.5 THz bandwidth available for spectroscopy. The peak point of the spectrum corresponds to 0.5 THz frequency. Figure 3-21 (b) shows the measured THz pulse after passage through the 5 mm thick *n* type silicon sample. The main THz pulse is delayed 40.6 psec compared to the original THz pulse. The delay depends on the thickness of the sample and the index of refraction. The amplitude of the peak THz pulse is reduced 75%. Figure 3-22 (a) (dashed line) shows the corresponding amplitude spectrum of the output pulse with the sample. The spectrum is shifted in the high frequency direction and the peak point of the spectrum corresponds to 0.8 THz frequency.

The calculated power absorption shows in Figure 3-22 (dots). The power absorption measurement extends has from 0.15 to 2.5 THz because of the limited THz power spectra as shown in Figure 3-22 (a).

GaAs Bowtie 30^0 Transmitter and SOS 10-80-10 Receiver

The GaAs 10-80-10 transmitter and SOS 10-30-10 receiver have a low sensitivity around the 0.1 THz frequency range but the power absorption and dispersion of the highest *n* and *p* type Si samples have a very strong effect at the low frequency range. Since the GaAs bowtie 30^o transmitter and SOS 10-80-10 receiver have a long dipole antenna structure, the frequency response is shifted to the lower frequency range.

Figure 3-21 (c) shows the THz pulse from 0 to 35 psec with no sample. The corresponding amplitude spectrum of this 0.91 psec FWHM pulse is presented in Figure 3-22 (b) solid line and illustrates the 1.5 THz bandwidth available for spectroscopy. The peak point of this spectrum corresponds to 0.12 THz frequency. When compared to the other chips, the spectral response is shifted to the low frequency range. Figure 3-21 (d) shows the measured THz pulse after passage through the sample from 35 psec to 70 psec and its spectrum is shown in Figure 3-22 (b) (dashed line). The spectrum is shifted in the high frequency direction and the peak point of the spectrum corresponds to 0.45 THz frequency.

The calculated power absorption is shown in Figure 3-22 (circles). The power absorption can only be calculated from 0.08 to 0.8 THz because of its limited THz power spectra as shown in Figure 3-22 (b). The two different measurement results have overlap from 0.15 to 0.8 THz frequency range. We combine data from the low and the high frequency ranges of 0 to 0.15 THz data using the GaAs bowtie 30^o transmitter and SOS 10-80-10 receiver and 0.8 to 2.5 THz data by GaAs 10-80-10 transmitter and SOS 10-30-10 receiver respectively.

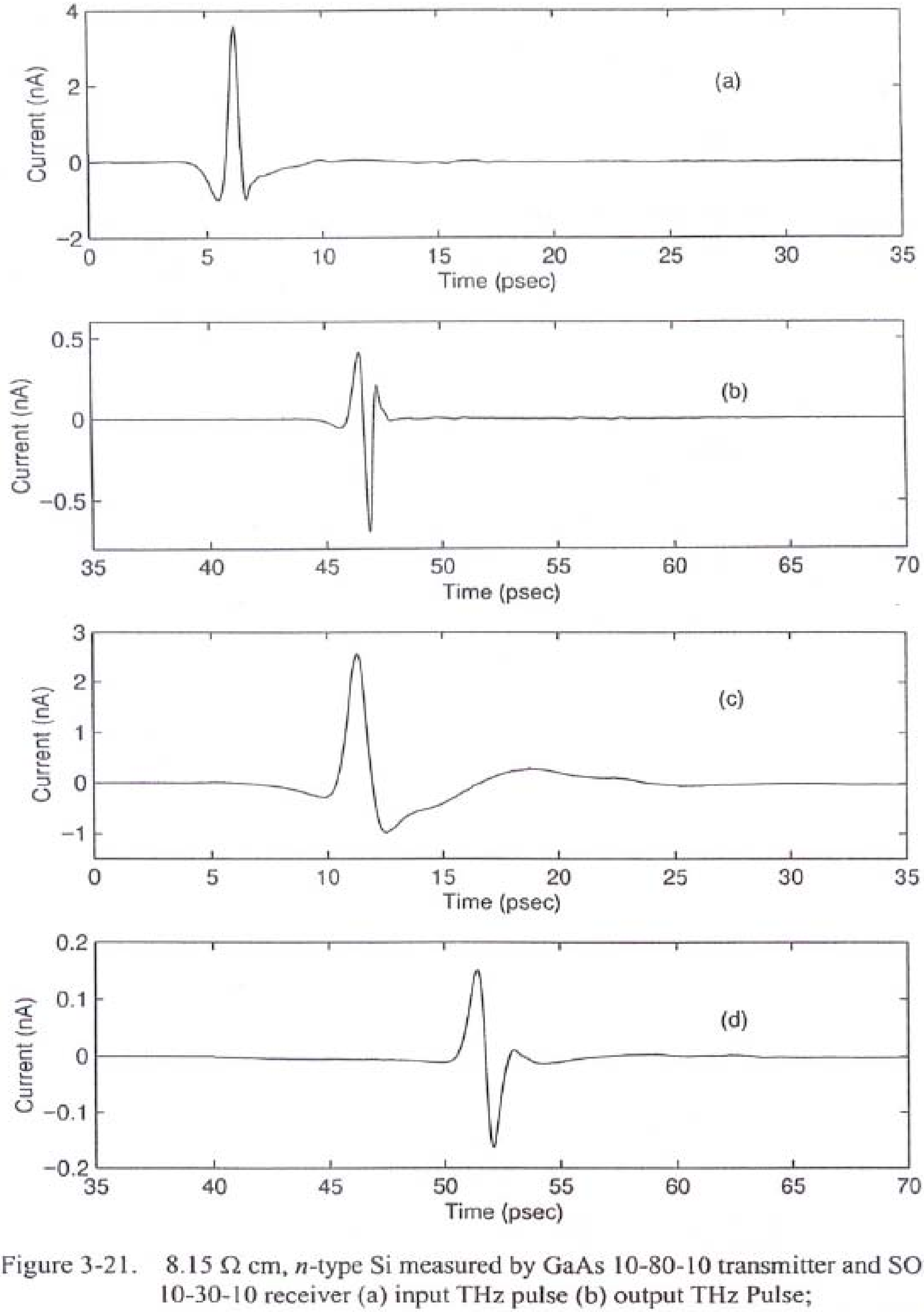

Figure 3-21. 8.15 Ω cm, *n*-type Si measured by GaAs 10-80-10 transmitter and SOS 10-30-10 receiver (a) input THz pulse (b) output THz Pulse; 8.15 Ω cm, *n*-type Si measured by GaAs Bowtie 30° transmitter and SOS 10-80-10 receiver (c) input THz pulse (d) output THz Pulse.

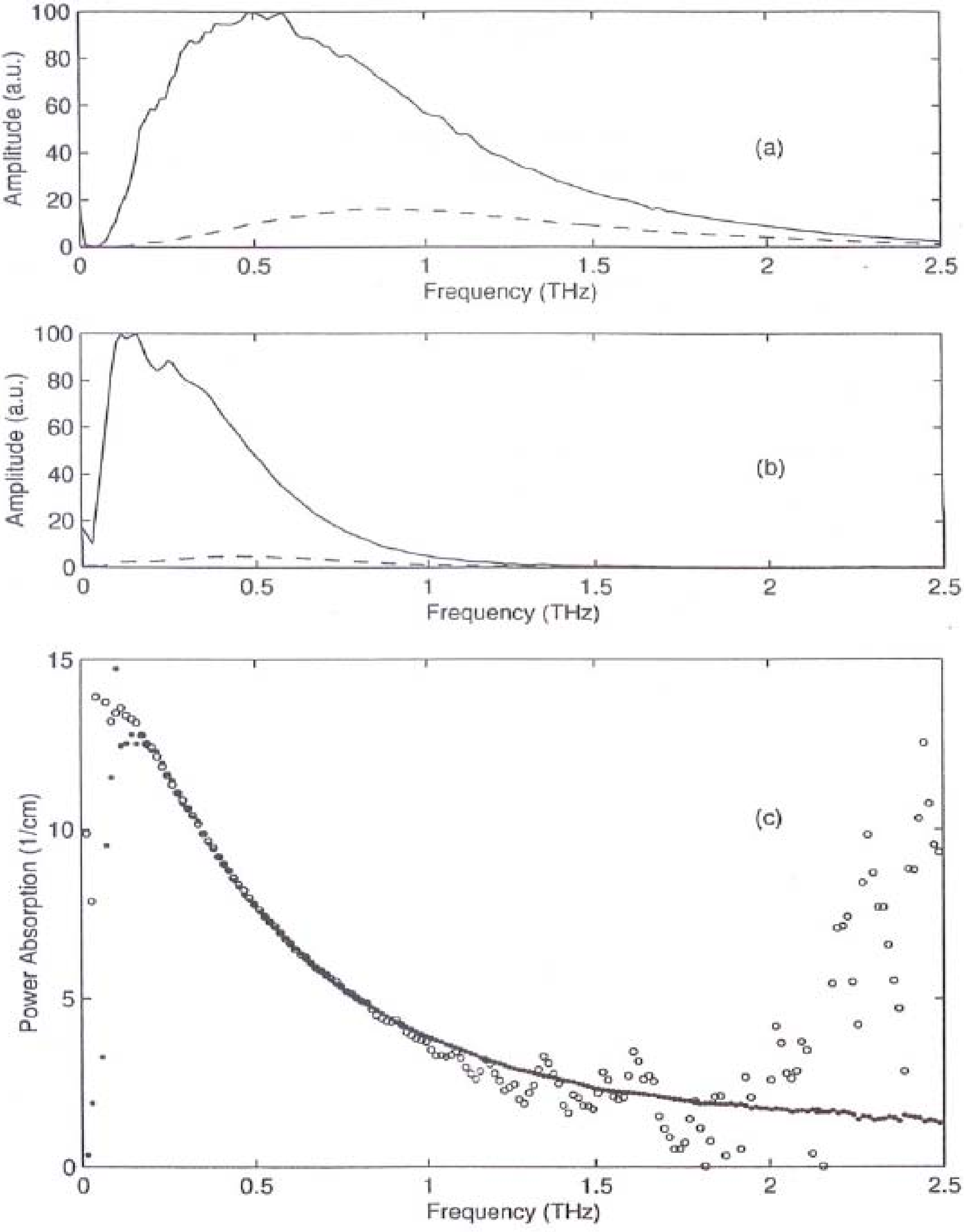

Figure 3-22. 8.15 Ω cm, *n*-type Si (a) compare two amplitude spectra; solid line (input) and dashed line (output) measured by GaAs 10-80-10 transmitter and SOS 10-30-10 receiver. (b) compare two amplitude spectra; solid line (input) and dashed line (output) measured by GaAs Bowtie 30° transmitter and SOS 10-80-10 receiver. (c) power absorption; dots (by spectra (a)) and circles (by spectra (b)).

CHAPTER IV

THEORIES FOR DOPED SILICON (TRANSMISSION MEASUREMENT)

Magnitude and Phase shift

In order to analyze the data we should consider the magnitude $|T_{tot}|$ and phase ϕ_{tot} correction factors, because the output data have already included these factors.

$$Output(\omega) = Input(\omega)\left|T_{tot}\right| \exp\left(-\frac{d\alpha}{2}\right) \exp\left(i\frac{2\pi}{\lambda}n(\omega)d\right) \exp\left(i\phi_{tot}\right) \qquad (4\text{-}1)$$

where α is the power absorption coefficient and d is the thickness of the sample. $\exp(-\alpha/2)$ is the power absorption by the sample and $\exp(i(2\pi/\lambda)n(\omega)d)$ is the phase change caused by the sample. The output signal is

$$Output.Signal(\omega) = Input(\omega) \exp\left(-\frac{d\alpha}{2}\right) \exp\left(i\frac{2\pi}{\lambda}n(\omega)d\right) \qquad (4\text{-}2)$$

$$Output.Signal(\omega) = \frac{Output(\omega)}{\left|T_{tot}\right| \exp\left(i\phi_{tot}\right)} \qquad (4\text{-}3)$$

Therefore, in order to compute the output signal, the magnitude of the output data should be divided by the magnitude correction factor and the phase of output data should be subtracted from the phase correction factor.

Some of the low resistivity Si samples have exceptionally large index of refraction in the low frequency ranges, but the high resistivity Si window has almost constant index of refraction at all frequency ranges. Because the indices of refraction of the doped Si sample and the Si window are mismatched, an additional phase and magnitude shift will need to be considered in addition to the usual simple analysis.

When the THz pulse propagates perpendicular to the interface between air and the Si window, the transmission coefficients are

$$t_{12} = \frac{2n_1}{n_1 + n_2} = 0.45 \tag{4-4}$$

$$t_{45} = \frac{2n_4}{n_4 + n_5} = 1.55 \tag{4-5}$$

where t_{12} is the transmission coefficient from the air to the Si window and t_{45} is transmission coefficient from the Si window to air, as shown in Figure 4-1. The total transmission is

$$t_{tot} = t_{12}t_{23}t_{34}t_{45} = 0.7\left(\frac{2n_2}{n_2 + n_3}\right)\cdot\left(\frac{2n_3}{n_3 + n_4}\right) \tag{4-6}$$

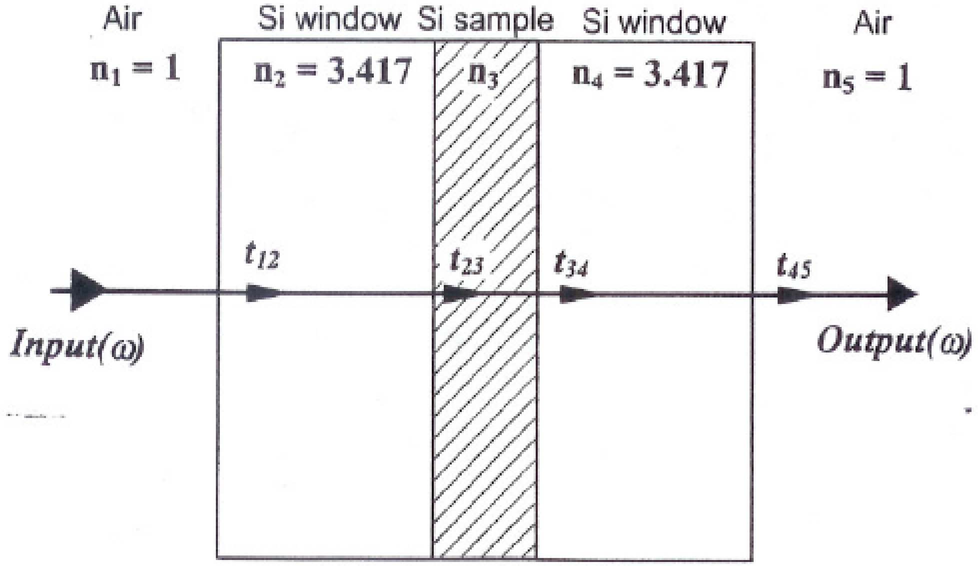

Figure 4-1. Perpendicular propagation of the THz pulse to the ”Si window + Si sample + Si window”.

where $n_1 = n_5$ and $n_2 = n_4$. Because the samples have frequency-dependent absorption and dispersion, n_3 has complex index of refraction, $n_3 = n_r + i\, n_i$.

Therefore

$$t_{tot} = 0.7\frac{4n_2n_3}{\left(n_2+n_3\right)^2}$$

$$= 0.7\frac{4n_2n_3}{\left(n_2^2+2n_2n_3+n_3^2\right)}$$

$$= 0.7\frac{4n_2\left(n_r+in_i\right)}{n_2^2+2n_2\left(n_r+in_i\right)+\left(n_r^2+i2n_rn_i-n_i^2\right)}$$

$$= 0.7\frac{4n_2\left(n_r+in_i\right)}{n_2^2+2n_2n_r+n_r^2-n_i^2+i2\left(n_2n_i+n_rn_i\right)}$$

Let $D_r = n_2^2+2n_2n_r+n_r^2-n_i^2$ and $D_i = 2\left(n_2n_i+n_rn_i\right)$, then the above equation can be written as

$$t_{tot} = 2.8\frac{n_2\left(n_r+in_i\right)}{D_r+iD_i}$$

$$= 2.8\frac{n_2\left(n_r+in_i\right)\left(D_r-iD_i\right)}{\left(D_r+iD_i\right)\left(D_r-iD_i\right)}$$

$$= 2.8\frac{n_2\left(n_rD_r+n_iD_i\right)+in_2\left(n_iD_r-n_rD_i\right)}{D_r^2+D_i^2} \qquad (4\text{-}7)$$

The total transmission can be expressed by its magnitude and phase as $t_{tot} = \left|\mathrm{T}_{tot}\right|e^{i\phi_{tot}}$. The magnitude of the correction factor (shift) is

$$\left|T_{tot}\right| = 2.8n_2\sqrt{\frac{n_r^2+n_i^2}{D_r^2+D_i^2}} \qquad (4\text{-}8)$$

and the phase correction factor (shift) is

$$\tan\phi_{tot} = \frac{n_i D_r - n_r D_i}{n_r D_r + n_i D_i}$$

$$= \frac{n_i\left(n_2^2 + 2n_2 n_r + n_r^2 - n_i^2\right) - 2n_r\left(n_2 n_i + n_r n_i\right)}{n_r\left(n_2^2 + 2n_2 n_r + n_r^2 - n_i^2\right) + 2n_i\left(n_2 n_i + n_r n_i\right)}$$

$$= \frac{n_i n_2^2 + 2n_i n_2 n_r - 2n_r n_2 n_i + n_i n_r^2 - 2n_r^2 n_i - n_i^3}{n_r n_2^2 + 2n_2 n_r^2 + n_r^3 - n_r n_i^2 + 2n_2 n_i^2 + 2n_r n_i^2}$$

$$= \frac{n_i\left(n_2^2 - n_r^2 - n_i^2\right)}{n_r\left(n_2^2 + 2n_2 n_r + n_r^2 + n_i^2\right) + 2n_2 n_i^2}$$

$$\phi_{tot} = \tan^{-1}\left(\frac{n_i\left(n_2^2 - n_r^2 - n_i^2\right)}{n_r\left(n_2^2 + 2n_2 n_r + n_r^2 + n_i^2\right) + 2n_2 n_i^2}\right) \qquad (4\text{-}9)$$

where the magnitude correction factor $|T_{tot}|$ and the phase correction factor ϕ_{tot} have two unknown parameters; n_r and n_i. These two unknown parameters can be determined by plasma frequency $\omega_p/2\pi$ and damping rate $\Gamma/2\pi$. These relations are discussed along with Drude theory in this Chapter and calculations are shown in Appendix C. Then we can determine the magnitude and phase correction factors by an iterative method as shown in below.

1. Determine the plasma frequency and the damping rate to calculate the power absorption and index of refraction which have the best fit to the measurements.
2. Calculate the magnitude and phase correction factors by the index of refraction.
3. Using the correction factors, determine new plasma frequency and damping rate to calculate the new power absorption and index of refraction for the best fit to the measurements.

4. Calculate new magnitude and phase correction factors by the new index of refraction
5. And so on.
6. When the discrepancy between the new and the old parameters is less than 1%, we can determine the plasma frequency and damping rate.
7. Finally we can determine the magnitude and phase correction factors.

Because these magnitude and phase correction factors depend on the real and imaginary part of the index of refraction, the correction factors also depend on the resistivity of the samples.

Figure 4-2 shows these correction factors for the *n* and *p* type Si samples. The highest resistivity *n* type sample, Figure 4-2 (a) and (b) (solid line), has very small change of the magnitude and phase correction. The shifted frequency ranged is from 0 to 0.05 THz. Because of the frequency response of this THz-TDS system, the experimental data is considered reliable only above approximately 0.08 THz. Therefore these magnitude and phase shifts do not affect the experimental data. However, the lowest resistivity *n* type sample, Figure 4-2 (c) and (d) (dotted line), has a very large change of the magnitude and phase shift that extend to 2.5 THz. The magnitude shift is increasing from 0 to 1.19 with frequency from 0 to 1.25 THz and slowly decreasing at higher frequencies. The phase shift is slowly increasing from -0.8 rad to 0.05 rad with frequency from 0 to 1.9 THz and slowly decreases at higher frequencies. Therefore these correction factors are important for the low resistivity Si sample. Figure 4-2 (e) and (f) shows the correction factors of *p* type Si samples and the situation is the same as *n* type silicon.

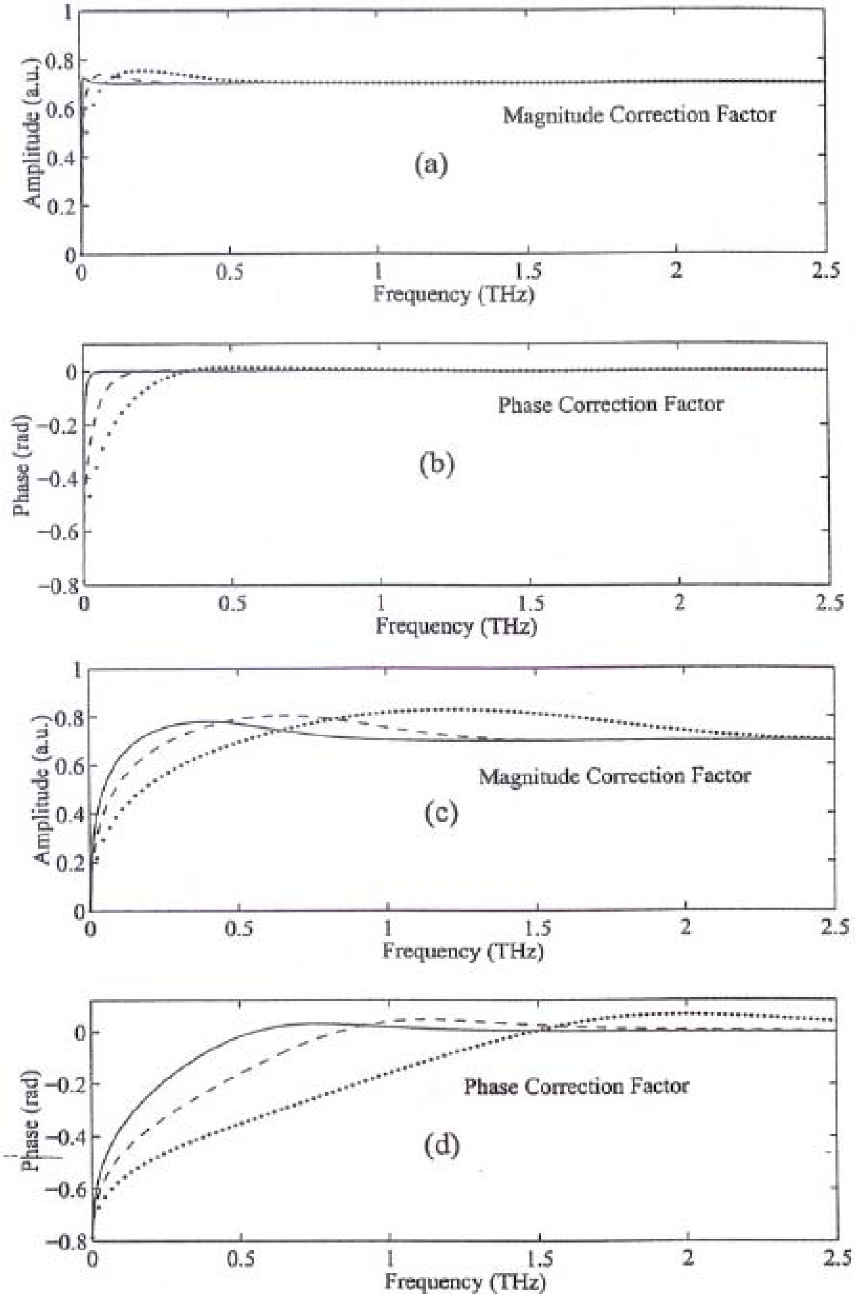

Figure 4-2 Calculated correction factors of "Si window + *n*-type Si samples + Si window". (a) Magnitude correction factors: 8.15 Ω cm (solid line); 1.31 Ω cm (dashed line); 0.48 Ω cm (dotted line). (b) Phase correction factors: 8.15 Ω cm (solid line); 1.31 Ω cm (dashed line); 0.48 Ω cm (dotted line). (c) Magnitude correction factors: 0.21 Ω cm (solid line); 0.12 Ω cm (dashed line); 0.0055 Ω cm (dotted line). (d) Phase correction factors: 0.21 Ω cm (solid line); 0.12 Ω cm (dashed line); 0.0055 Ω cm (dotted line).

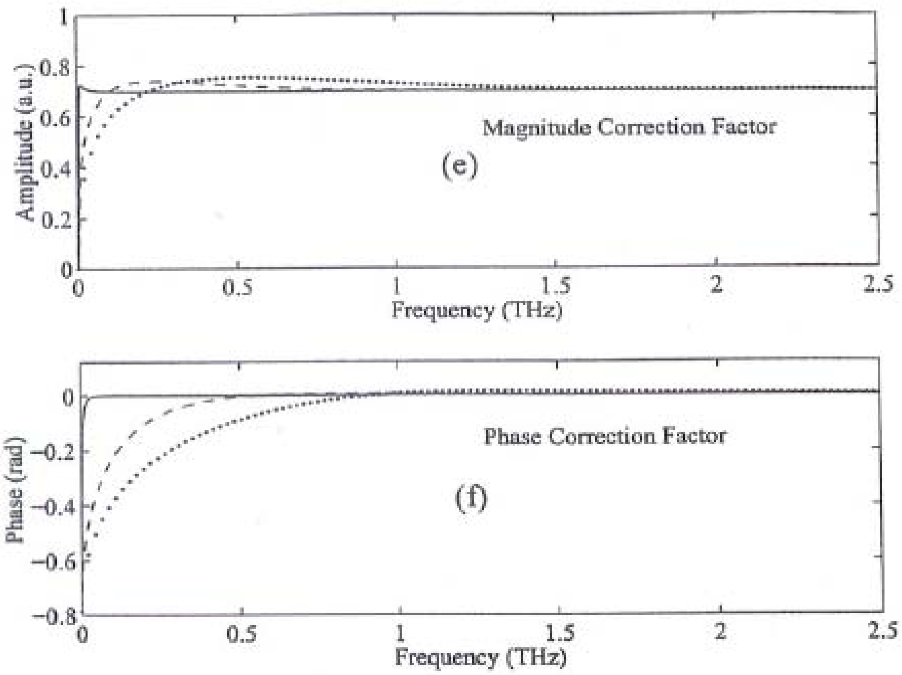

Figure 4-2 Calculated correction factors of "Si window + *p*-type Si samples + Si window". (e) Magnitude correct factors: 9.61 Ω cm (solid line); 0.40 Ω cm (dashed line); 0.17 Ω cm (dotted line). (f) Phase correct factors: 9.61 Ω cm (solid line); 0.40 Ω cm (dashed line); 0.17 Ω cm (dotted line).

Drude Theory

The dielectric properties of semiconductors have been described by the Drude model, which treats the free carriers in a solid as classical point charges subject to random collisions [5]. The electric absorption and dispersion of many systems are odd and even ordered symmetric curves about the logarithm of the frequency. According to the Debye and Drude model, the complex dielectric constant ε with angular frequency ω is [5, 23]

$$\varepsilon = \varepsilon_\infty + \frac{i\sigma}{\omega\varepsilon_0} = \varepsilon_\infty - \frac{\omega_p^2}{\omega(\omega + i\Gamma)} \tag{4-10}$$

where ε_∞ is the limiting high frequency dielectric constant of the given medium, ε_o is the free-space permittivity, Γ is the damping rate, σ is the complex conductivity, and ω_p is the plasma angular frequency defined by $\omega_p{}^2 = Ne^2/\varepsilon_o m^*$. N is the density of carriers, e is the electronic charge, and m^* is the effective carrier mass. The effective mass in Si [6,25] is given by $m_e = 0.26m_o$ and $m_h = 0.37m_o$, for the electrons and holes, respectively, where m_o is the free electron mass. The frequency-dependent complex dielectric constant ε is equal to the square of the complex index of refraction $n = n_r + in_i$ (see Appendix C). The imaginary index n_i is determined by measuring the power absorption coefficient $\alpha = n_i 4\pi/\lambda_o$, where λ_o is the free space wavelength. For undoped silicon, the real part of the index of refraction $n_r = 3.417$ and absorption coefficient $\alpha \cong 0$ have been measured [8] over the frequency range considered here. The complex conductivity given by the Drude model [7,11] is

$$\sigma = \frac{\sigma_{dc}}{1 - i\omega\tau} = \sigma_{dc}\frac{i\Gamma}{\omega + i\Gamma} = \frac{i\varepsilon_0\omega_p^2}{\omega + i\Gamma} \tag{4-11}$$

where $\tau = 1/\Gamma$ is the average collision time (relaxation time) and σ_{dc} is the dc conductivity of the medium, which is given by $\sigma_{dc} = e\mu N$, with the mobility μ equal to $\mu = e/m^{*}\Gamma$. The real and imaginary parts of the complex conductivity are given by

$$\sigma_r = \mathrm{Re}[\sigma] = \frac{\sigma_{dc}}{1+\omega^2\tau^2} \tag{4-12}$$

$$\sigma_i = \mathrm{Im}[\sigma] = \sigma_{dc}\frac{\omega\tau}{1+\omega^2\tau^2} \tag{4-13}$$

Figure 4-3 (a) shows the calculated real and imaginary conductivity at THz frequencies. Under the Drude analysis the real parts of the conductivity are always odd ordered symmetry curves and the imaginary parts of the conductivity are always even ordered symmetry curves about the logarithm of the frequency as shown in Figure 4-3 (b). Figure 4-3 (c) shows the real part of the conductivity plotted against the imaginary part of the conductivity. It is a symmetrical semicircle of radius $\sigma_{dc}/2$. The real axis has two intercept points, σ_∞ and σ_{dc}, on that axis where σ_∞ is the real conductivity at infinite frequency. The imaginary conductivity has its maximum value at $\omega = 1/\tau$. Because of the symmetrical structure, the maximum imaginary conductivity corresponds to the center of the semicircle. In this complex plane, the frequency is increasing when traveling counterclockwise along the semicircle.

Some semiconductor measurements have been analyzed with the Drude model [7,11]. In the low frequency ranges, this model fit well, but at the high frequency ranges, the experimental values are not in agreement with this model, especially high resistivity silicon samples. The Debye equation has been extensively used in the analysis of experimental data on dielectric relaxation because it is valid at low frequency ranges. However, the Debye expression may not hold at high frequencies. Therefore it is required to modify the model to make the calculation more satisfactory at higher frequencies.

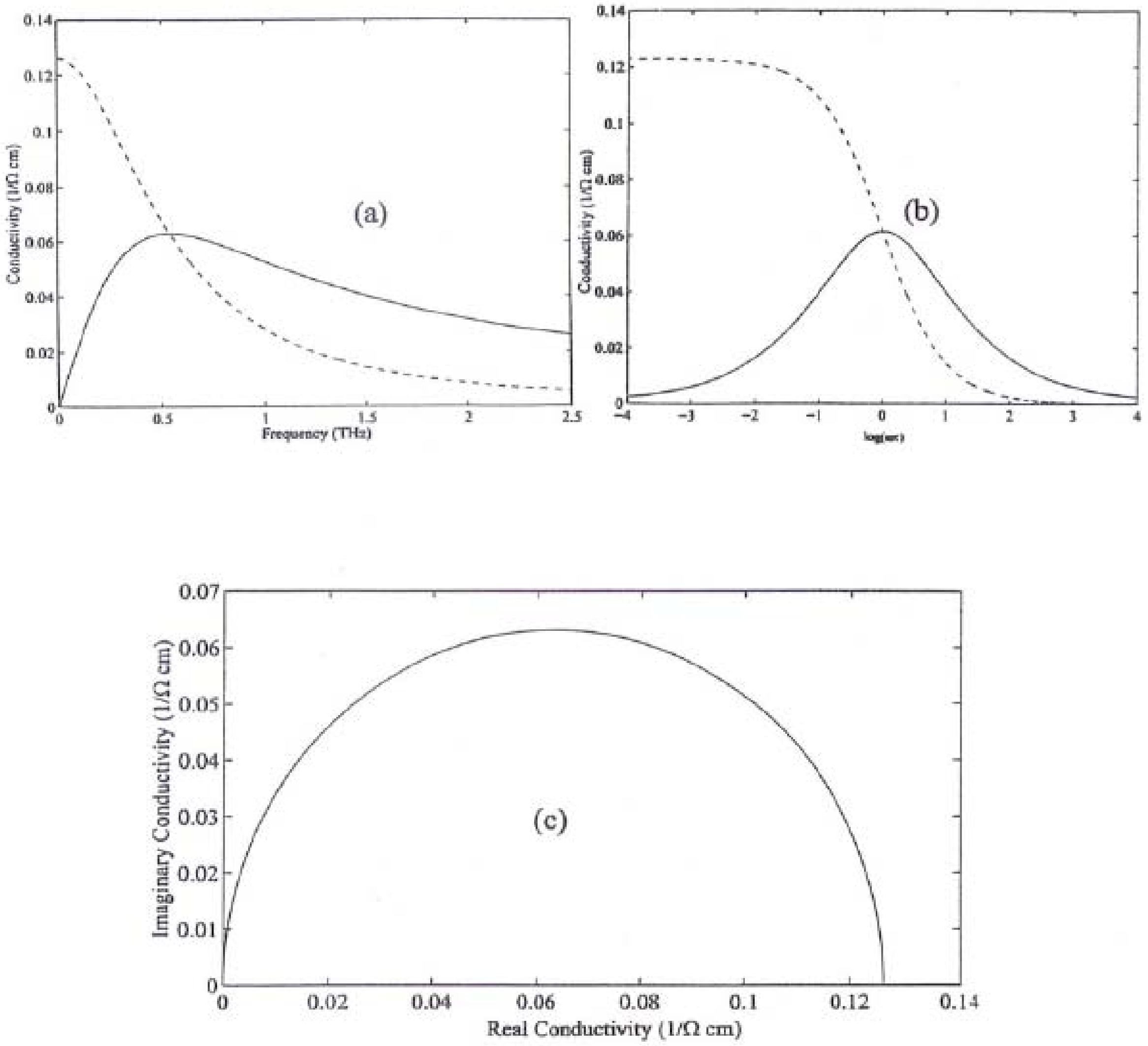

Figure 4-3. Real and imaginary conductivity by Drude theory. (a) Real conductivity (dashed line) and imaginary conductivity (solid line) as a function of the THz frequency; (b) Real conductivity (dashed line) and imaginary conductivity (solid line) as a function of log(ωτ); (c) Real conductivity as a function of imaginary conductivity.

Scattering Theory

The Drude theory has a single carrier relaxation time but, to make a more accurate description of the carrier dynamics, the energy dependence of the carrier dynamics has been developed by many scientists [10,11,12]. The energy dependence of the carrier relaxation time can be split into lattice and impurity scattering relaxation times [12].

$$\frac{1}{\tau(E)} = \frac{1}{\tau_L(E)} + \frac{1}{\tau_I(E)} \qquad (4\text{-}14)$$

where the energy dependent damping rate $\Gamma(E) = 1/\tau(E)$.

Therefore we may simply write

$$\Gamma(E) = \Gamma_L(E) + \Gamma_I(E) \qquad (4\text{-}15)$$

The energy dependent damping rate associated with lattice scattering, $\Gamma_L(E)$, has carrier energy to the power 0.5 and the energy dependent damping rate associated with impurity scattering, $\Gamma_I(E)$, has carrier energy to the power -1.5 [10,11,12]. Therefore the total energy dependent damping rate is

$$\Gamma(E) = \Gamma_l(E/kT_o)^{0.5} + \Gamma_i(E/kT_o)^{-1.5} \qquad (4\text{-}16)$$

where Γ_l and Γ_i are the coupling constants which are characterized by the efficiency of scattering with the lattice and the impurities, and T_o is a normalization parameter with dimension temperature. The conductivity from Drude theory can be shown to be energy dependent by integrating over the conduction or valence band. The fundamental equation of conductivity is given by [11,12]

$$\sigma = \frac{Ne^2}{m^*}\left\langle \frac{\tau(E)}{1 - i\omega\tau(E)} \right\rangle = i\varepsilon_0\omega_p^2\left\langle \frac{1}{\omega + i\Gamma(E)} \right\rangle \qquad (4\text{-}17)$$

where the symbol < > represents Maxwellian averages weighted by the product of the distribution of the carriers times their energy. For a parabolic band [10,11,12],

$$\langle x(E)\rangle = \frac{\int_0^\infty x(E)\cdot E^{1.5}\exp(-E/kT)dE}{\int_0^\infty E^{1.5}\exp(-E/kT)dE} \tag{4-18}$$

The real and imaginary conductivity, index of refraction, and power absorption are given by

$$\mathrm{Re}\,\sigma = \langle\sigma_r\rangle = \frac{Ne^2}{m^*}\left\langle\frac{\Gamma(E)}{\omega^2+\Gamma(E)^2}\right\rangle \tag{4-19}$$

$$\mathrm{Im}\,\sigma = \langle\sigma_i\rangle = \frac{Ne^2}{m^*}\left\langle\frac{\omega}{\omega^2+\Gamma(E)^2}\right\rangle \tag{4-20}$$

$$n_r\left(\langle\sigma_r\rangle,\langle\sigma_i\rangle\right) = \sqrt{\frac{\left(\varepsilon_\infty - \frac{\langle\sigma_i\rangle}{\omega\varepsilon_0}\right) + \sqrt{\left(\varepsilon_\infty - \frac{\langle\sigma_i\rangle}{\omega\varepsilon_0}\right)^2 + \left(\frac{\langle\sigma_r\rangle}{\omega\varepsilon_0}\right)^2}}{2}} \tag{4-21}$$

$$\alpha\left(\langle\sigma_r\rangle,\langle\sigma_i\rangle\right) = \frac{\langle\sigma_r\rangle}{c\varepsilon_0 n_r\left(\langle\sigma_r\rangle,\langle\sigma_i\rangle\right)} \tag{4-22}$$

When the coupling constants Γ_l and Γ_i are adjusted to give the same half-width for the real conductivity and the power absorption, the impurity coupling constant Γ_i has a stronger effect at the high frequency ranges than the lattice coupling constant Γ_l, as shown in Figure 4-4. Scattering theory with only lattice scattering is similar to Drude theory. Compared to Drude theory ($\omega_p/2\pi$ = 0.925 THz, $\Gamma/2\pi$ = 0.62 THz), lattice scattering ($\Gamma_l/2\pi$ = 0.488 THz, Γ_i = 0) predicts a little less absorption at the lower frequencies and predicts a little more absorption at the higher frequencies as shown in the dashed line of Figure 4-4 (a). However, scattering theory with only impurity scattering (Γ_l = 0, $\Gamma_i/2\pi$ = 4.21 THz) predicts too little absorption at the lower frequencies and predicts too much absorption at the higher frequencies. This situation is the same for the real part of conductivity as shown in Figure 4-4 (c). Scattering theory with only lattice scattering predicts too large an index of refraction in the middle frequencies when compared to Drude theory. Scattering theory with only impurity scattering predicts too high an index of refraction in the middle frequencies as shown in Figure 4-4 (b). This situation is reversed for the imaginary part of the conductivity. The lattice scattering predicts too small an imaginary conductivity at the middle frequencies and the impurity scattering predicts too small an imaginary conductivity at the middle frequencies as shown in Figure 4-4 (d). Therefore the impurity coupling constant is an important parameter to reduce the difference between the experimental data and Drude theory.

The mobility is related to the energy dependent damping rate and is given by:

$$\mu = \frac{e}{m^*}\left\langle \frac{1}{\Gamma(E)} \right\rangle = \frac{e}{m^*}\left\langle \frac{1}{\Gamma_l\left(E / kT_0\right)^{0.5} + \Gamma_i\left(E / kT_0\right)^{-1.5}} \right\rangle \tag{4-23}$$

$$\therefore \left\langle \frac{1}{\Gamma_l\left(E / kT_0\right)^{0.5} + \Gamma_i\left(E / kT_0\right)^{-1.5}} \right\rangle = \frac{\mu m^*}{e}. \tag{4-24}$$

Because the lattice scattering depends only on temperature, the lattice coupling constant Γ_l should be held at a constant value with the doped semiconductor materials. To determine the lattice coupling constant, I used the Baccarani-Ostoja mobility curve [26] for *n*-type silicon and the Caughey-Thomas mobility curve [27] for *p*-type silicon. They proposed the following empirical expression for carrier mobility in silicon:

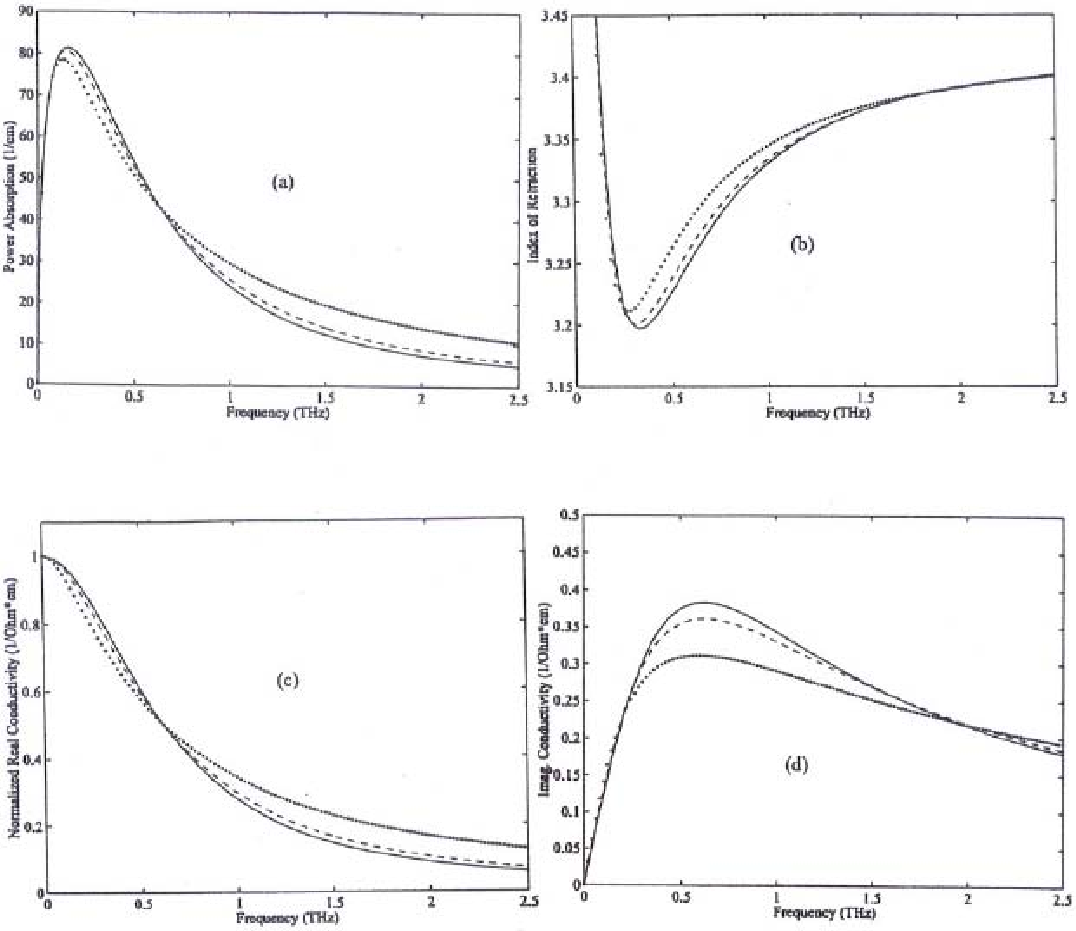

Figure 4-4. Calculated (a) power absorption; (b) index of refraction; (c) real conductivity; (d) imaginary conductivity . The Drude theory with energy independent damping rate is indicated by the solid line. The dashed line describes lattice scattering only ($\Gamma_l/2\pi$=0.488 THz, Γ_i=0) and the dotted line describes impurity scattering only (Γ_l=0, $\Gamma_i/2\pi$=4.21 THz).

$$\mu = \mu_{\min} + \frac{\mu_{\max} - \mu_{\min}}{1 + \left(N / N_{ref}\right)^{\gamma}} \tag{4-25}$$

and determined the numerical values of the four parameters of Table 4-1.

	μ_{max} (cm^2/Vs)	μ_{min} (cm^2/Vs)	γ	N_{ref} (cm^{-3})
Baccarani-Ostoja	1360	92	0.91	1.3×10^{17}
Caughey-Thomas	495	47.7	0.76	6.3×10^{16}

Table 4-1. Four parameters to determine the mobility curve.

These mobility curves are shown in Figure 4-5 (a) for *n* type silicon and in Figure 4-6 (a) for *p* type silicon. These mobility curves saturate at 1360 cm^2/Vs (*n*-type) and 495 cm^2/Vs (*p*-type) and the impurity scattering effect is almost zero in the low carrier density ranges. This means the impurity coupling constant should be zero: $\Gamma_i = 0$. Therefore there are only lattice scattering effects in the carrier density ranges and Equation (4-24) is reduced to

$$\left\langle \frac{1}{\Gamma_l \left(E / kT_0\right)^{0.5}} \right\rangle = 2.011 \times 10^{-13} (\text{sec}) : (n \text{ type}) \tag{4-26}$$

$$\left\langle \frac{1}{\Gamma_l \left(E / kT_0\right)^{0.5}} \right\rangle = 1.041 \times 10^{-13} (\text{sec}) : (p \text{ type}) \tag{4-27}$$

where the calculated lattice coupling constants are $\Gamma_l/2\pi$ = 0.59THz and $\Gamma_l/2\pi$ = 1.15THz for *n* and *p* type silicon, respectively. These lattice coupling constants should be constant over the entire carrier density range. Using the results of Figure 4-5 (a) and Figure 4-6 (a) and Equation (4-27), we can calculate the impurity coupling constants and the coupling ratios,

Γ_i/Γ_l ($\Gamma_l/2\pi$ = 0.59THz for *n* type and $\Gamma_l/2\pi$ = 1.15THz for *p* type), which are shown in Figure 4-5 (b) and Figure 4-6 (b). The inset shows the expanded view of the coupling ratio from 10^{15} cm^{-3} to 2×10^{17} cm^{-3}.

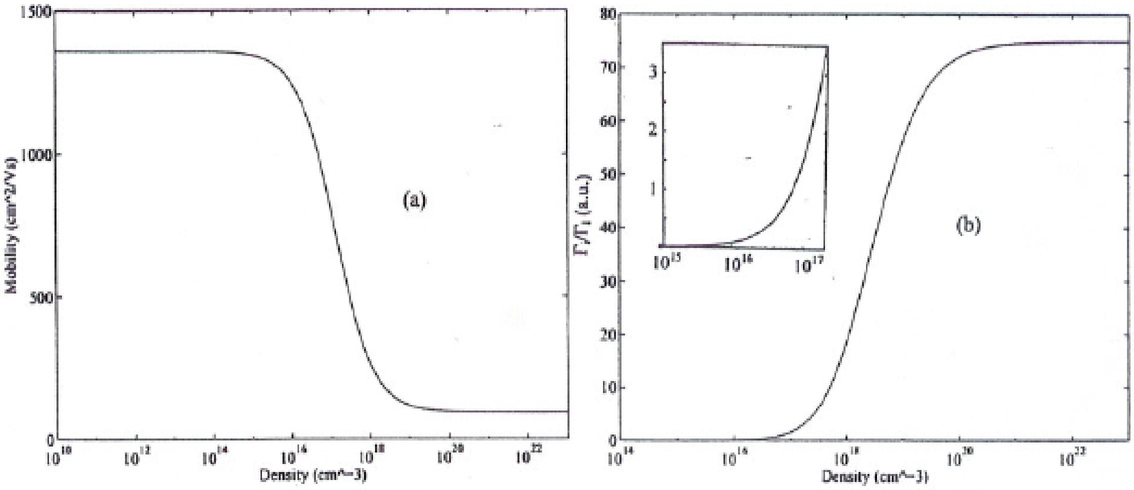

Figure 4-5 Mobility curve of *n*-type and the coupling ratio (a) Baccarani-Ostoja mobility curve; (b) The ratio of impurity and lattice coupling constants

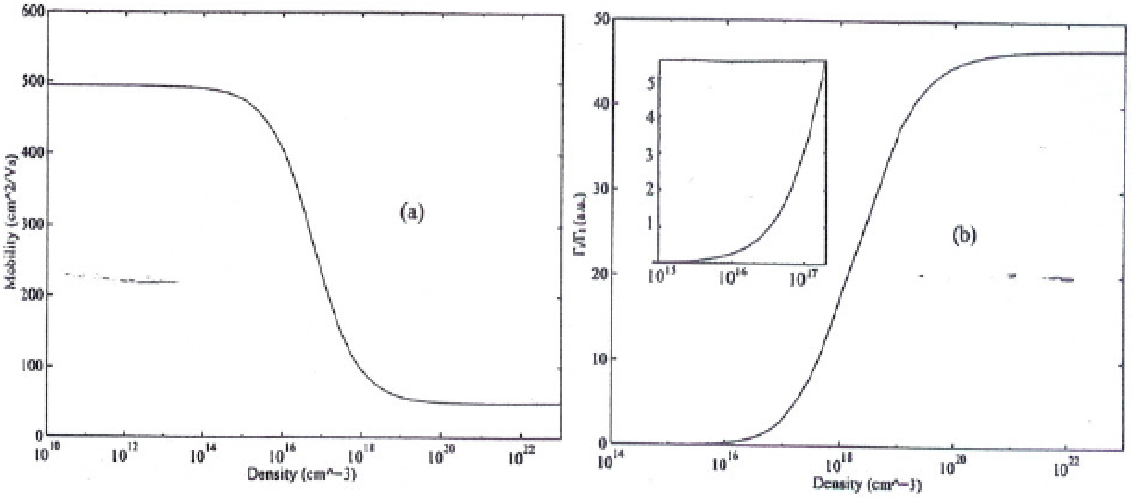

Figure 4-6 Mobility curve of *p*-type and the coupling ratio (a) Caughey-Thomas mobility curve; (b) The ratio of impurity and lattice coupling constants

Cole-Davidson Distribution

Many scientists have tried to measure the dielectric constants of disordered materials, such as molecular liquids [13, 28], polymers [14] and more recently ionic glasses [15]. These results do not follow Debye’s distribution function. They used a modified distribution function, the Cole-Davidson distribution function [13, 28]. This model gives a good fit to the experimental data for the materials. By using Cole-Davidson and Drude theory we obtain a modified complex conductivity which is given by

$$\sigma = \sigma_{dc} \frac{1}{(1 - i\omega\tau)^{\beta}} \tag{4-28}$$

where β is a distribution parameter with $0 \le \beta \le 1$. The Cole-Davidson distribution is the same as Drude theory for $\beta = 1$. The distribution model has a non-symmetrical behavior.

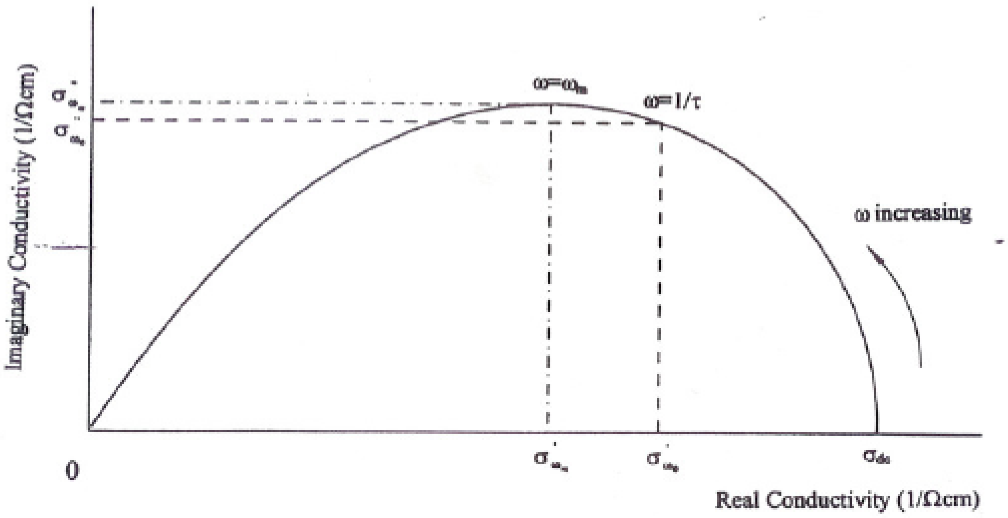

Figure 4-7. The Cole-Davidson plot of the imaginary conductivity against the real conductivity.

The plot of the complex plane, Figure 4-7, gives a skewed arc rather than a semicircle. The center of the skewed arc is shifted in the positive direction oalong the real conductivity axis. The corresponding real and imaginary values are [29]

$$\sigma_{\omega_0}^{'} = \sigma_{dc} 2^{-\beta/2} \cos\frac{\pi\beta}{4} \tag{4-29}$$

$$\sigma_{\omega_0}^{''} = \sigma_{dc} 2^{-\beta/2} \sin\frac{\pi\beta}{4} \tag{4-30}$$

The maximum value of the imaginary conductivity occurs not at 1/τ but at angular frequency ω_m, given by [29]

$$\omega_m = \frac{1}{\tau}\tan\frac{\pi}{2(1+\beta)} \tag{4-31}$$

When the frequency is ω_m the real and imaginary conductivity are given by [29]

$$\sigma_{\omega_m}^{'} = \sigma_{dc}\left[\cos\frac{\pi}{2(1+\beta)}\right]^{\beta}\cos\frac{\pi\beta}{2(1+\beta)} \tag{4-32}$$

$$\sigma_{\omega_m}^{''} = \sigma_{dc}\left[\cos\frac{\pi}{2(1+\beta)}\right]^{\beta}\sin\frac{\pi\beta}{2(1+\beta)} \ . \tag{4-33}$$

Figure 4-8 (a,b) show both the Drude and Cole-Davidson distributions where $\omega_p/2\pi$ = 0.35 THz and $\Gamma/2\pi$ = 0.57 THz. The distribution parameter β for Drude theory is 1, and for the Cole-Davidson model β is 0.85. Figure 4-8 (a) shows that the real and imaginary conductivity have shifted to the high frequencies compared to Drude theory's real and imaginary conductivity. The Cole-Davidson distribution model has a strong effect at the high frequencies. The imaginary conductivity plotted against the real conductivity of Drude theory is a semicircle but the Cole-Davidson distribution model has a skewed arc as shown in Figure 4-8 (b). If the distribution parameter has small values, the skewed arc approximates to a straight line at the zero point of the real axis.

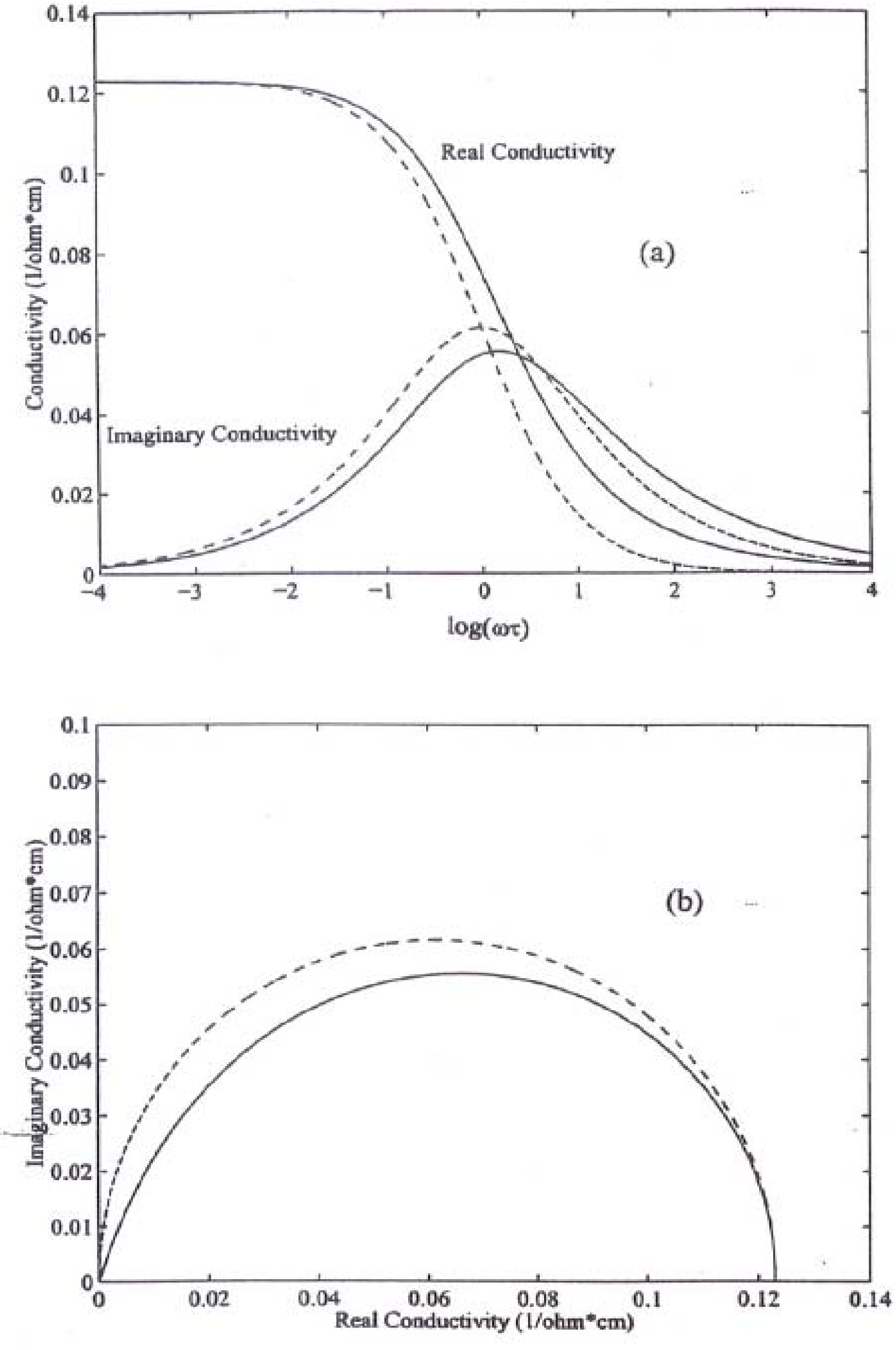

Figure 4-8. Compare the Drude (dashed line) and Cole-Davidson (solid line) distribution. (a) real and imaginary conductivity against log(ωτ); (b) the imaginary conductivity against the real conductivity.

Decay Function

Using the inverse Fourier transform, the frequency-dependent Drude function can be converted to a time-dependent decay function as [30]

$$\sigma(\omega) = \sigma_{dc} \frac{1}{(1 - i\omega\tau)} \tag{4-34}$$

$$\Phi(t) = \Phi_0 \exp\left(-\frac{t}{\tau}\right) \tag{4-35}$$

where Φ_0 is a normalizing parameter. The time-domain response function, f(t) = ifft($1/(1-i\omega\tau)^{\beta}$), of Drude theory gives shown in Figure 4-9 (a) by a solid line where $\beta = 1$ and $\Gamma/2\pi = 0.57$ THz. Drude theory is the single-sided exponential in Equation (4-35). However, for the Cole-Davidson case, the time-domain response function changes to one with faster initial decay which asymptotically approaches the Drude result [15] as shown in a dashed line ($\beta = 0.8$) and dotted line ($\beta = 0.9$) of Figure 4-9 (a).

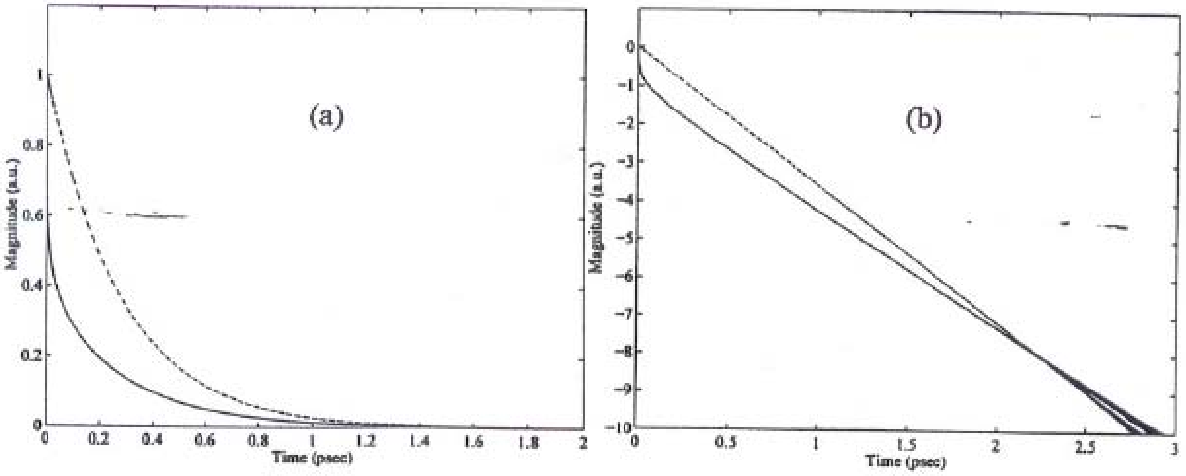

Figure 4-9 Compare the Drude (dashed line) and Cole-Davidson (solid line) distribution function of the relaxation time. (a) decay function; (b) logarithm of the decay function

Figure 4-9 (b) shows the step function, $A(t)=\int_0^t f(x)dx$, of Drude (solid line) and C-D case (dashed or dotted lines). The C-D case approaches 1 much faster. This behavior shows that the Cole-Davidson response function has a distribution of relaxation times. The distribution of relaxation time (primary C-D distribution) is known analytically [15, 28] as shown in Equation 4-36.

$$\rho_{CD}(\tau)=\frac{\sin(\pi\beta)}{\pi\tau}\left[\frac{\tau}{\tau_{CD}-\tau}\right]^{\beta} \qquad \text{for } \tau<\tau_{CD}$$

$$=0 \qquad \text{for } \tau\geq\tau_{CD} \tag{4-36}$$

$$f(\tau)=\int_0^{\tau}\rho_{CD}(x)dx \qquad \text{for } \tau<\tau_{CD}$$

$$=1 \qquad \text{for } \tau\geq\tau_{CD} \tag{4-37}$$

where τ_{CD} is the characteristic relaxation time. Figure 4-10 shows these relations.

In the Cole-Davidson model, the decay function, Φ(t), depends on the distribution parameter. For small distribution parameter these is very rapid decay in the time domain. Figure 4-9 (a) shows this relation.

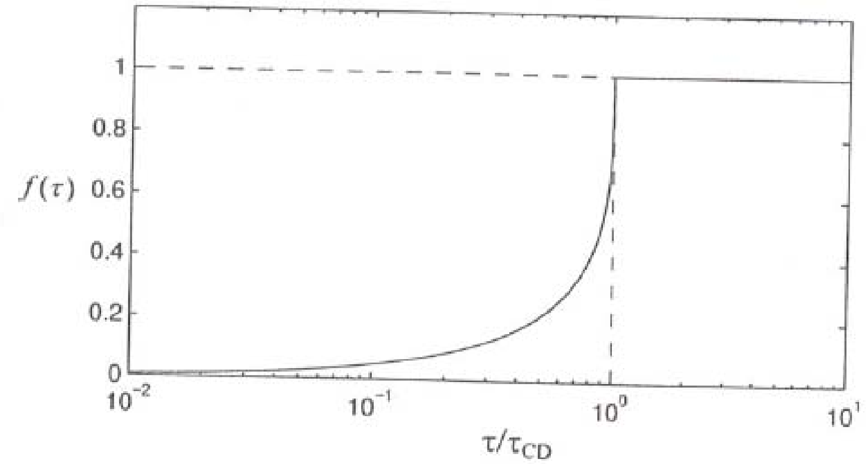

Figure 4-10 The function $f(\tau)$ of processes with relaxation times for β=0.8.

Generalized Conductivity

There are three different theories to analyze the data; Drude, scattering, and Cole-Davidson. The theoretical approaches are described by the following two generalized relationships for the conductivity.

$$\sigma = i\varepsilon_o \omega_p^2 \left\langle \frac{1}{\omega + i\Gamma(E)} \right\rangle \tag{4-37}$$

$$\sigma = \varepsilon_o \omega_p^2 \tau \frac{1}{(1 - i\omega\tau)^{\beta}} \tag{4-38}$$

For Drude theory $\beta = 1$, in Equation (4-37) and $<1/(\omega + i\Gamma(E))> = 1/(\omega + i\Gamma(E))$ in the then equivalent Equation (4-38). For scattering theory $\Gamma(E) = \Gamma_l(E/kT_o)^{0.5} + \Gamma_i(E/kT_o)^{-1.5}$ in Equation (4-37) and for the Cole-Davidson model $0 \leq \beta \leq 1$ in Equation (4-38).

At zero frequency all three theories should give the same dc conductivity which is measured by 4-point probe measurement. The dc conductivity is given by $\sigma_{dc} = e\mu N$ and all the fits originate from the same dc conductivity at $\omega = 0$. Because the dc conductivity is constant, the product μN is should be the same for all the theories, thereby determining the ratio of ω_p^2/Γ and eliminating one free parameter.

CHAPTER V

DATA ANALYSIS FOR DOPED SILICON (TRANSMISSION MEASUREMENT)

Magnitude and Phase Shift

The dotted lines of the Figure 4-2 (c) and (d) show the magnitude and phase correction factors of the lowest resistivity *n* type silicon sample (0.055 Ω cm, sample #9500887-03). The correction factors are large from the low frequency ranges up to 2.5 THz. In Figure 5-1 (a) and (b), the dashed lines show the magnitude and phase spectra of the output pulse, respectively. The time domain THz pulses are shown in Appendix B-9. After using the correction factors for the Si sample, the solid lines show the new spectra of the output pulse. Therefore the power absorption, index of refraction, and real and imaginary conductivity are changed in these frequency ranges as shown in Figure 5-1 (c-f). The open circle shows the results without the corrections and the dot shows the results after the corrections. At the low frequency ranges, the imaginary conductivity (Figure 5-1 (f)) has a large shift and the corrected imaginary conductivity starts from zero. These results agree very well with the theoretical results, especially at the low frequency ranges.

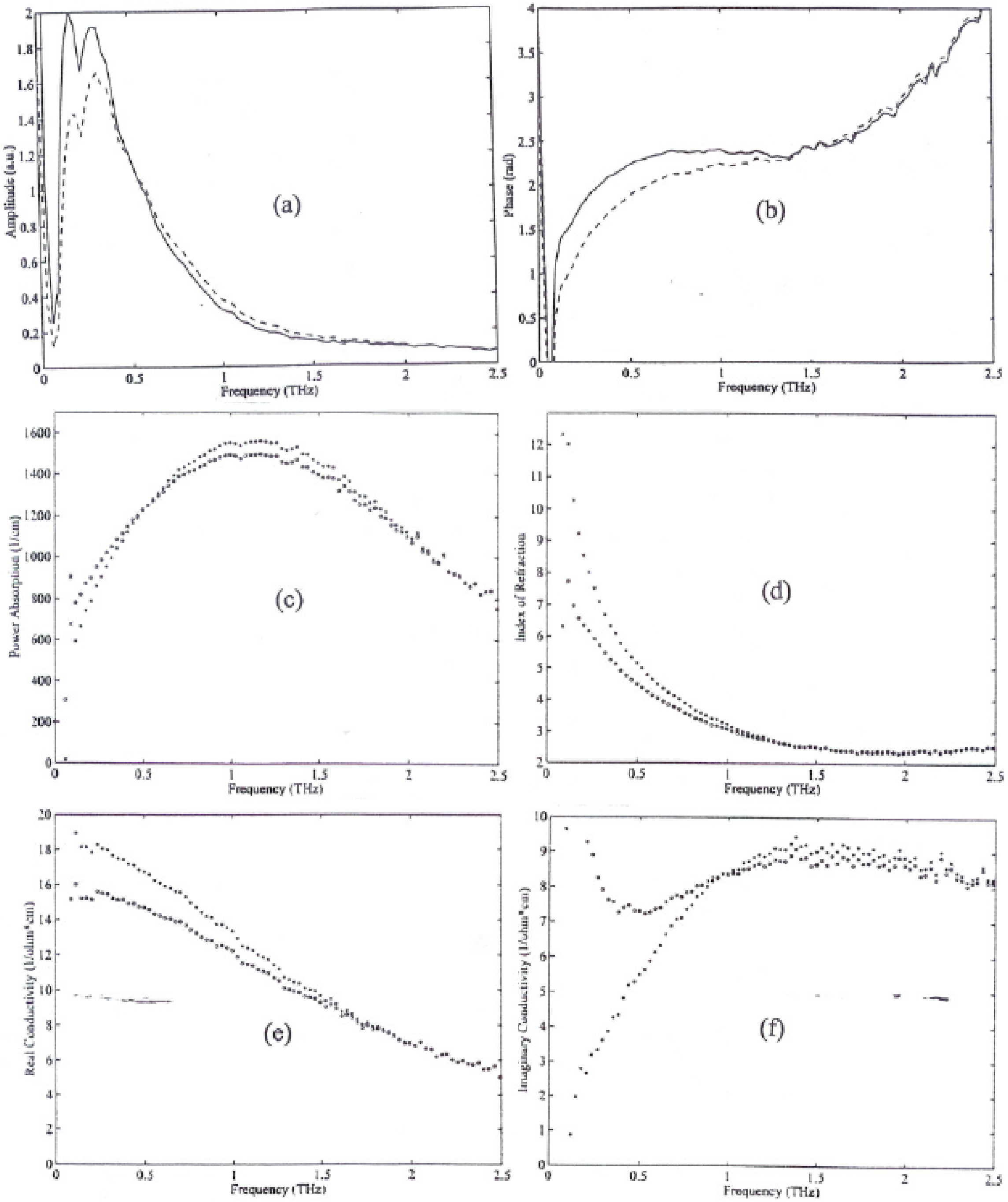

Figure 5-1. Compare before (dashed line) and after (solid line) corrections; (a) Amplitude of spectrum; (b) Phase of spectrum. Before (open circle) and after (dot); (c) Power absorption; (d) Index of refraction; (e) Real conductivity; (f) Imaginary Conductivity

Drude Theory

After applying the correction factors to the experiment data, the *n* and *p* type silicon samples can be analyzed by the simple Drude theory. For these samples we find an excellent agreement with the Drude theory in the low frequency range. However, as the frequency increases beyond the carrier damping rate, the measured power absorption and the real conductivity become significantly larger than the simple Lorentzian shape of Drude theory.

The THz-TDS measurements of the power absorption of the highest resistivity 8.15 Ω cm, *n*-type, and 9.61 Ω cm, *p*-type Si samples are shown in Figure 5-2 (a). Even though the data have an excellent signal-to-noise (S/N) ratio, due to the frequency response of the THz-TDS system the data are considered reliable only above 0.08 THz. The measurement results are the combination of 2 separate measurements of the same highest resistivity *n* and *p* type silicon sample. Since the two data are in excellent agreement in the middle frequency range from 0.3 THz to 0.85 THz, the low frequency range is covered using the GaAs Bowtie 30^{o} transmitter and SOS 10-80-10 receiver and the high frequency uses the GaAs 10-80-10 transmitter and SOS 10-30-10 receiver are taken.

For the highest resistivity *n*-type silicon, the parameters are $\omega_p/2\pi = 0.35$ THz and $\Gamma/2\pi = 0.54$ THz and, for the highest resistivity *p*-type silicon, the parameters are $\omega_p/2\pi = 0.448$ THz and $\Gamma/2\pi = 1.03$ THz. These measurements show the different dynamic behavior of the electrons and holes. The measured index of refraction is shown in Figure 5-2 (b). The index of refraction is strongly frequency-dependent, showing a clear minimum followed by a dramatic increase towards low frequencies. The measured index of refraction approaches 3.417, which is the same index of refraction as the undoped high resistivity silicon. Given these measurements of the power absorption and index of refraction, the general relationship of Equation (4-11) determines the real σ_r and the imaginary σ_i parts of the conductivity as shown in Figure 5-2 (c,d). Because of the excellent agreement with Drude theory for low frequency ranges the dc conductivity σ_{dc} is a reasonable value; σ_{dc} = 7.93 Ω cm for *n*-type and σ_{dc} = 9.25 Ω cm for *p*-type. These values could be more accurate than the four-point-probe measurements. At zero frequency the four-point-probe measurements are indicated by the asterisks as shown in Figure 5-2 (c).

Figure 5-2 (e) shows the real conductivity as a function of imaginary conductivity. The solid line describes simple Drude theory for 8.15 Ω cm, *n*-type Si and the dashed line describes simple Drude theory for 9.61 Ω cm, *p*-type Si. The measurements are from 0 to 2.5 THz. In this complex plane, the frequency is increasing when traveling counterclockwise along the semicircle. Like Figure 5-2 (c), the four-point-probe measurements are indicated by the asterisks. Although the real conductivity is in good agreement with the Drude theory at the low frequencies, the imaginary conductivity is in disagreement with the Drude theory at these frequencies. Therefore there are disagreements for all frequency ranges between the measurements and the simple Drude theory in this figure. These disagreements may indicate the need for an extension of the simple Drude model as in scattering theory or the Cole-Davidson model.

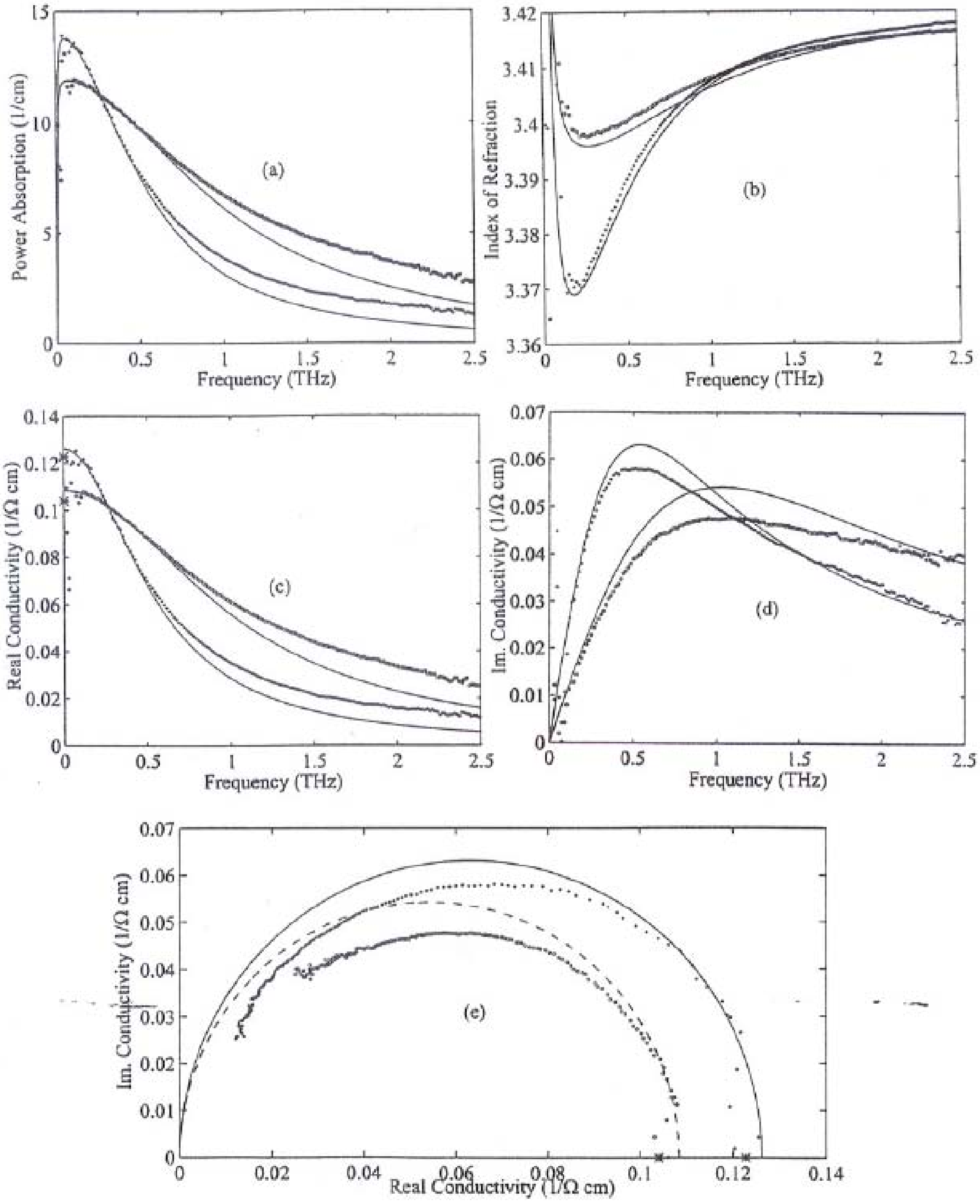

Figure 5-2. Measured results for 8.15 Ω cm, *n*-type (dots) and 9.61 Ω cm, *p*-type (open circles) silicon. Solid lines describe simple Drude theory. (a) Power absorption; (b) Index of refraction; (c) Real conductivity; (d) Imaginary Conductivity; (e) Real conductivity as a function of imaginary conductivity.

Calculation of Mobility by Drude Theory

The mobility is calculated from $\mu=e/(m^*\Gamma)$ and the values of the *n*-type and *p*-type samples are 2000 cm^2/Vs and 730 cm^2/Vs, respectively. These values are higher than the literature values of 1360 cm^2/Vs and 450 cm^2/Vs expected for lightly doped *n*-type and *p*-type silicon, respectively [26,27]. The mobilities of other samples are shown in Table 6-1 to Table 6-5 in Chapter VI, and the mobility curves are shows in Figure 6-6.

Scattering Theory

Because of the energy dependent damping rate, the experimental results should be fit by considering electron-phonon collisions (lattice) and carrier scattering from ionized impurities. The ratio of the lattice and impurity scattering constants are already calculated as shown in Figure 4-5 (b) and 4-6 (b). However, the results do not follow these ratios. The lowest dopant results are well fit by the theory for which the major carrier relaxation process is from scattering by impurities and the minor process is electron-phonon scattering. In contrast, in order to obtain reasonable agreement with the measurements, at much higher number densities of carriers the relative proportion of lattice scattering must be increased.

Figure 5-3 (a-d) show the same THz-TDS measurements of the highest resistivity 8.15 Ω cm, *n*-type, and 9.61 Ω cm, *p*-type Si samples. Pure impurity scattering, shown as the dotted lines calculated with the *n*-type parameters $\omega_p/2\pi$ = 0.437 THz, $\Gamma_i/2\pi$ = 3.8 THz and Γ_l = 0, and *p*-type parameters $\omega_p/2\pi$ = 0.588 THz, $\Gamma_i/2\pi$ = 8 THz and Γ_l = 0, predicts too little absorption at the low frequencies and too much absorption at the high frequencies. Pure electron-phonon (lattice) scattering, indicated by the dashed lines and calculated with the *n*-type parameters $\omega_p/2\pi$ = 0.37 THz, Γ_i = 0 and $\Gamma_l/2\pi$ = 0.45 THz and *p*-type parameters $\omega_p/2\pi$ = 0.485 THz, Γ_i = 0 and $\Gamma_l/2\pi$ = 0.9 THz is similar to Drude theory, and predicts too little absorption at higher frequencies. The best fitting combination of impurity and lattice scattering are shown as the solid lines. The *n*-type parameters $\omega_p/2\pi$ = 0.393 THz, $\Gamma_i/2\pi$ = 1.695 THz and $\Gamma_l/2\pi$ = 0.105 THz and *p*-type parameters $\omega_p/2\pi$ = 0.54 THz, $\Gamma_i/2\pi$ =4.69 THz and $\Gamma_l/2\pi$ = 0.138 THz, provide a better fit to the measurements but still shows deviations at higher frequencies.

Figure 5-3 (e) shows the real conductivity as a function of imaginary conductivity. The measurements cover the 0 to 2.5 frequency range. For the high frequency range, the scattering theory shows significant deviation from the measurements.

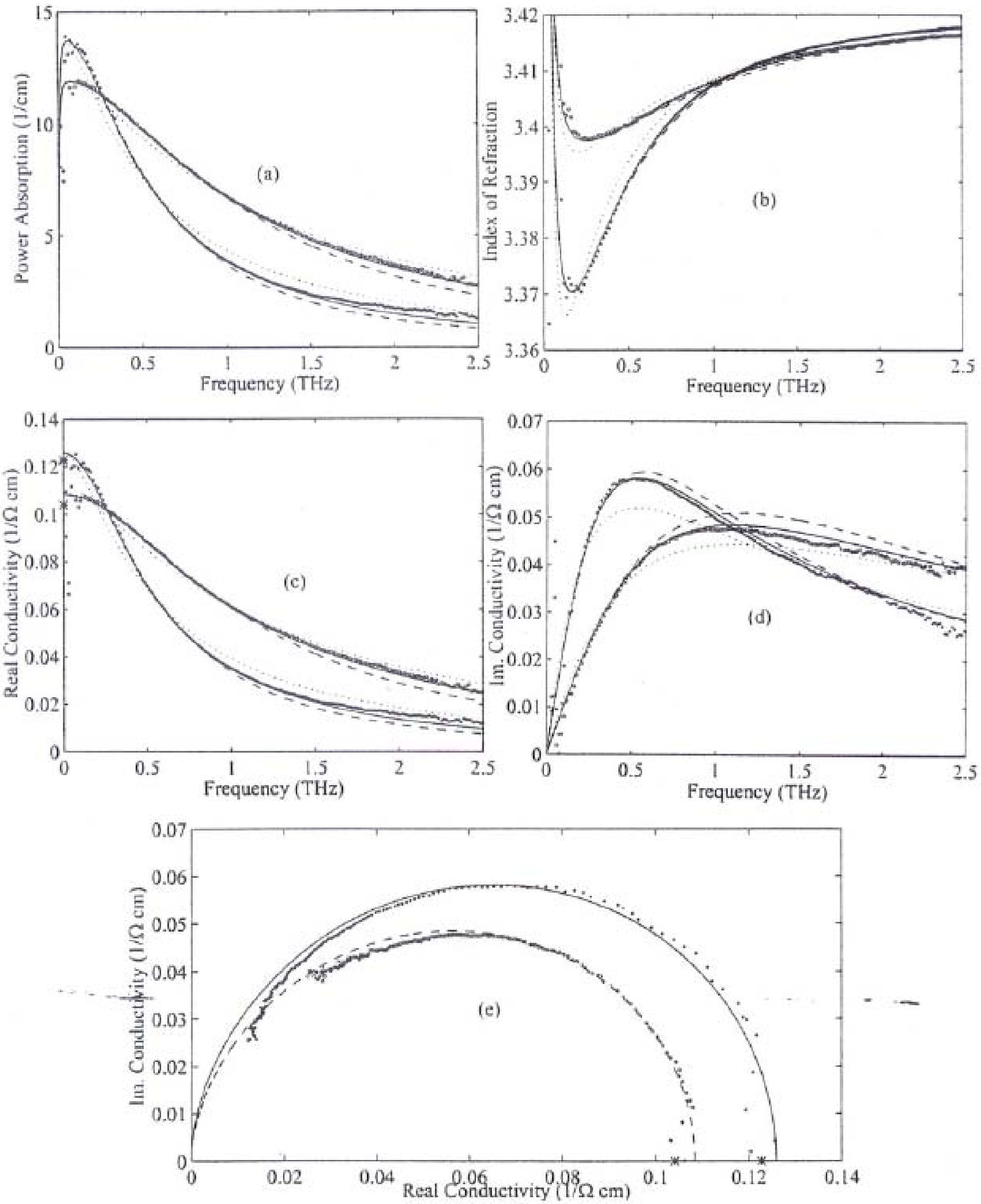

Figure 5-3. Measured results for 8.15 Ω cm, *n*-type (dots) and 9.61 Ω cm, *p*-type (open circles) silicon. The lines describe pure impurity scattering (dotted line), pure lattice scattering (dashed line), and impurity and lattice scattering (solid line). (a) Power absorption; (b) Index of refraction; (c) Real conductivity; (d) Imaginary conductivity; (e) Real conductivity as a function of imaginary conductivity.

Calculation of Mobility by Scattering Theory

The mobility is calculated from $\mu = \frac{e}{m}\left\langle \frac{1}{\Gamma(E)} \right\rangle$ and the values for *n* and *p* type Si sample are 1580 cm^2/Vs and 490 cm^2/Vs respectively. These values are lower than the mobilities from the Drude theory. Because these experimental results were measured at 293 ^oK temperature, the mobility is a bit large compared to the literature values which are measured at 300 ^oK temperature [26,27]. Usually, the electron and hole mobility in pure materials have a temperature dependence given by [31] $\mu = AT^{-r}$ and the values of the parameters are given in Table 5-1.

	Electrons	**Holes**	**Units**
A	1.43×10^9	1.35×10^8	$cm^2K^{-r}V^{-1}sec^{-1}$
r	2.42	2.20	-

Table 5-1. Parameters for the temperature dependence of electron and hole mobilities in high-purity silicon.

The mobility difference between 293 ^oK and 300 ^oK is 85 cm^2/Vs for *n*-type silicon and 25 cm^2/Vs for *p*-type silicon. Therefore the calculated mobilities are in good agreement with previous measurements [26, 27].

Cole-Davidson Distribution

The Drude theory and the scattering theory give a good fit to the power absorption and the real conductivity at the low frequencies but these theories do not give a good fit at the high frequencies. Also, these theories disagree with the index of refraction and the imaginary conductivity. However, the Cole-Davidson model gives an excellent fit to all of the experimental results. As shown in Figure 5-6, the Cole-Davidson distribution parameter β depends on the density of carriers. For low carrier density the distribution parameter is a small value and the parameter approaches unity as the number density of carriers is increased.

The power absorption coefficient of the highest resistivity 8.15 Ω cm, *n*-type and 9.61 Ω cm, *p*-type silicon samples are again shown in Figure 5-4 (a). The experimental data are extremely well fit over the entire frequency range by the Cole-Davidson distribution shown as the solid lines. For *n*-type sample, the Cole-Davidson parameter is $\beta = 0.84$, $\omega_p/2\pi = 0.323$ THz and $\Gamma/2\pi = 0.46$ THz, and for *p*-type, $\beta = 0.76$, $\omega_p/2\pi = 0.404$ THz and $\Gamma/2\pi = 0.84$ THz. The measured index of refraction is shown in Figure 5-4 (b), where a well-resolved minimum can be observed. The real and imaginary parts of the conductivity are shown in Figure 5-4 (c) and (d). The Cole-Davidson distribution again provides a markedly better fit than the Drude theory or the scattering theory results. At zero frequency, the four-point-probe measurements are indicated by the asterisks in the real part of the conductivity.

Figure 5-4 (e) shows the real conductivity as a function of imaginary conductivity up to 2.5 THz. For the high frequency range, the Cole-Davidson distribution has excellent agreement to the measurements (dots for *n*-type and open circle for *p*-type).

Figure 5-5 shows the deviation of the high resistivity *n* type sample between the measurements and the theory. Cole-Davidson distribution has less than 1 percent deviation from 0.5 to 1.5 THz as shown in Figure 5-5 (c). For the low frequency range, the deviation is less than 2 percent, while the deviation is increased up to 6 percent for the high frequency range. For the high frequency range, the Drude result of the real conductivity has up to 50 percent deviation as shown in Figure 5-5 (a), and the scattering result of the real conductivity has up to 25 percent deviation as shown in Figure 5-5 (b). In comparison, the Cole-Davidson distribution shows very good agreement with the measurements.

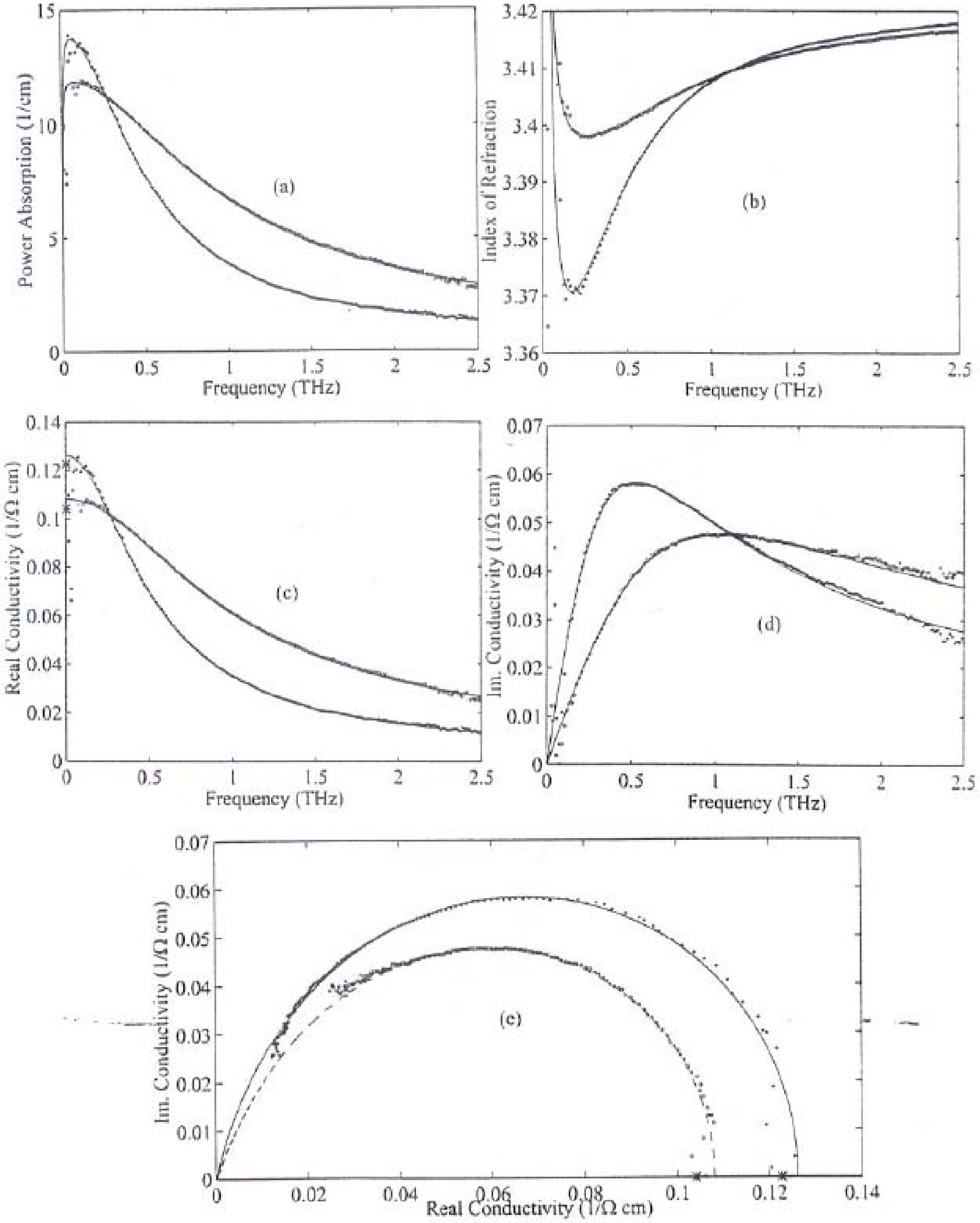

Figure 5-4. Measured results for 8.15 Ω cm, *n*-type (dots) and 9.61 Ω cm, *p*-type (open circles) silicon. Solid lines describe Cole-Davidson distribution. (a) Power absorption; (b) Index of refraction; (c) Real conductivity; (d) Imaginary conductivity; (e) Real conductiviry as a function of imaginary conductivity.

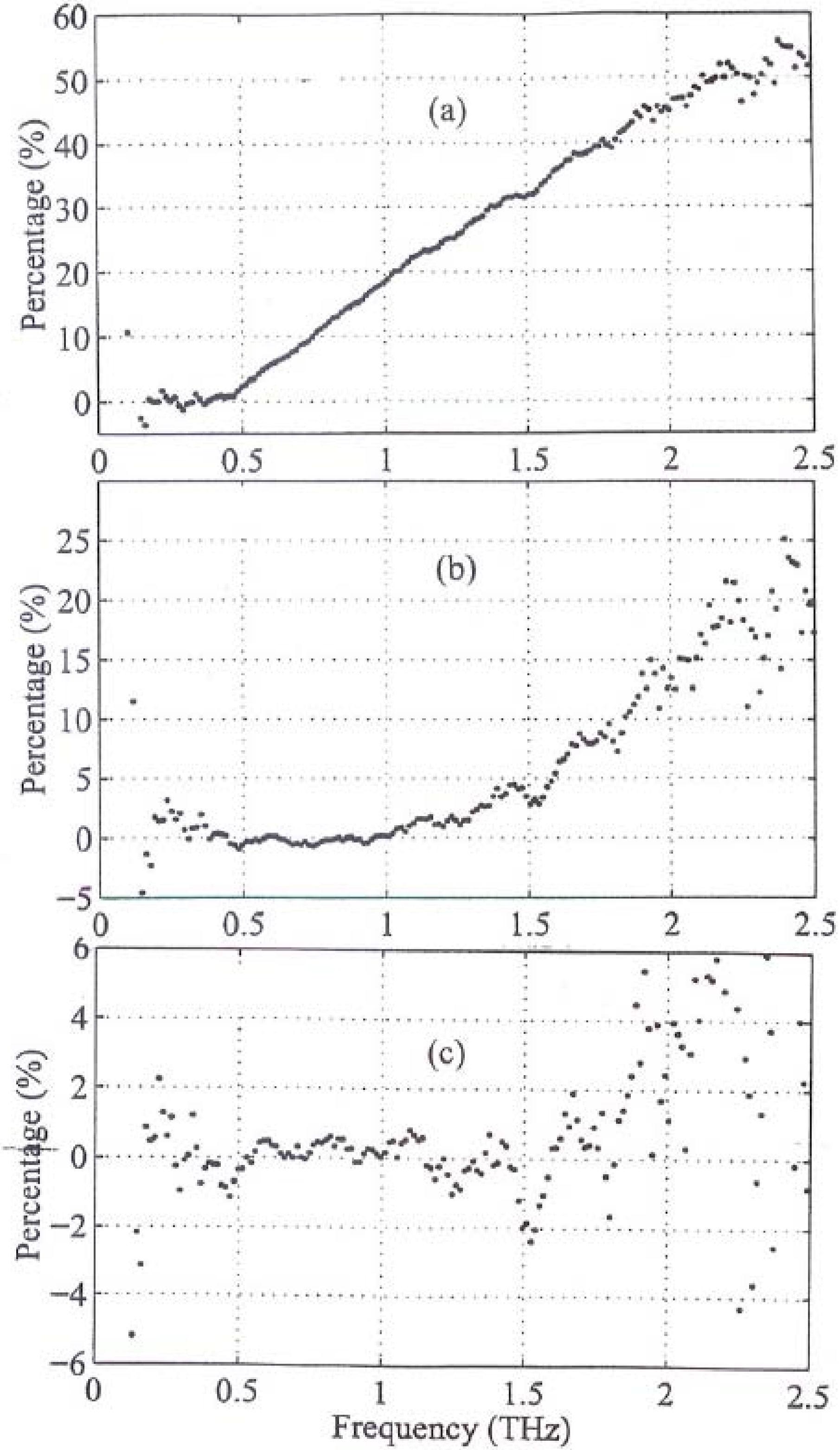

Figure 5-5. Deviation between measurements and theory of 8.15 Ω cm, *n*-type Si. (a) Drude theory (b) Scattering theory (c) Cole-Davidson distribution.

One of the possible physical processes resulting in the C-D distribution is reorientation of carriers by recombination and generation. Carrier recombination is the opposite process to carrier generation. Therefore, in thermal equilibrium, a process of recombination must occur for every process of generation. For thermal equilibrium the carrier distribution is uniquely described by the Fermi-level [12]. Since the electron and hole are created in close proximity, they attract each other and can form a hydrogen-like bond state, the exciton [38]. In this THz-TDS Si transmission measurement, there may be exciton absorption in doped semiconductors which include [39] a periodic alternation of the doping of only one semiconductor to form a series of homojunctions. The electron and hole approach each other closely, which causes the increase in their binding energy at the periodic alternation homojunction semiconductors [40,41] like the modulation doped Si. Because of the increased exciton binding energy, the life time of exciton is substantially changed [42].

Calculation of Mobility by Cole-Davidson Distribution

The mobility is calculated from $\mu=e/(m^*\Gamma)$ and the values of the 8.15 Ω cm, *n*-type, and 9.61 Ω cm, *p*-type samples are 2340 cm^2/Vs and 900 cm^2/Vs, respectively. These values are higher than the other measurements. However, at the high carrier density samples, the measured mobilities are in good agreement with the previous measurements [26,27]. The mobilities of other samples are shown in Table 6-1 to Table 6-5 in Chapter VI, and the mobility curves are shows in Figure 6-6.

Distribution Parameter

As discussed for the Cole-Davidson distribution of Chapter IV, the distribution parameter β has a strong effect at the high frequencies when compared to Drude theory. For the power absorption and the real conductivity, the higher resistivity sample has more deviation at the high frequencies. Thereby the distribution parameters depend on the resistivity of the sample. Because the higher resistivity samples have low carrier densities, the distribution parameter can be plotted as a function of carrier densities.

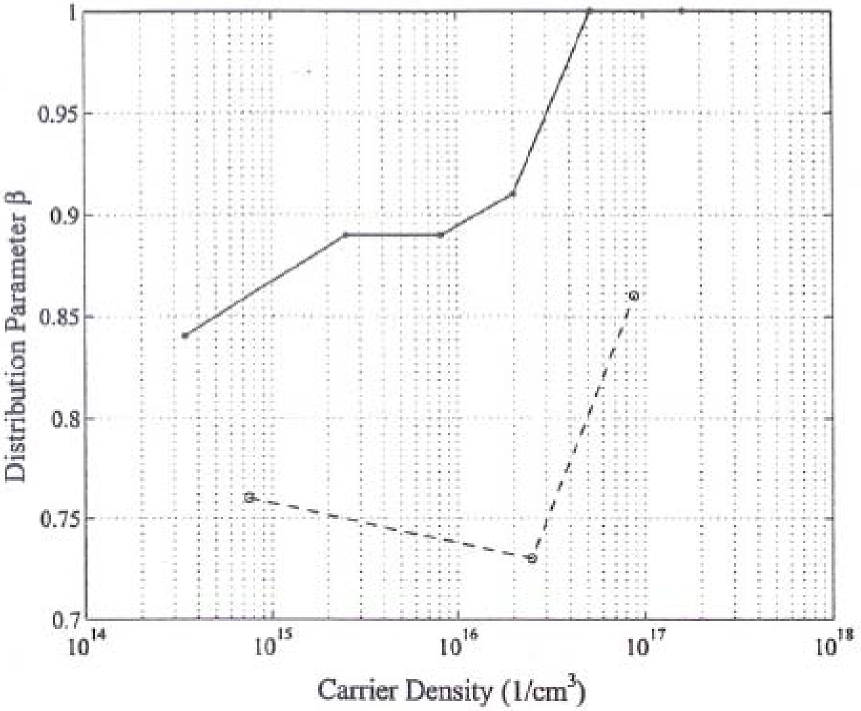

Figure 5-6. The Cole-Davidson distribution parameters as a function of carrier density (solid line: *n*-type & dashed line: *p*-type).

Figure 5-6 shows the relation between the distribution parameters and the carrier densities. For the *n*-type samples (solid line) the distribution parameter increases with density of carriers. For the two highest number densities the distribution parameter is 1, and Cole-Davidson theory reduces to Drude theory. For the *p*-type samples (dashed line) the distribution parameter shows a more abrupt increase as the density is increased.

CHAPTER VI

RESULTS AND CONCLUSIONS

Measured Results for Silicon Samples

In this section, the measured results for *n* and *p* type silicon samples are shown in Figure 6-1 to Figure 6-5. The measured time domain THz pulses are shown in Appendix B-1 to B-9. The Drude theory and scattering theory are shown as dashed lines and dotted lines, respectively. The Cole-Davidson distribution, shown as the solid lines, gives an excellent fit to all of the experimental results. The four-point-probe measurements are indicated by the asterisks in the real conductivity figures.

For the high resistivity samples, the measurements do not agree with Drude theory for high frequency ranges. However, all theories have good agreement with measurements for the low resistivity samples. Some figures cannot distinguish the Cole-Davidson distribution lines (dashed lines) and scattering theory lines (dotted lines) because these two lines are in very good agreement except at the high frequency ranges.

The theoretical fitting parameters and the calculated carrier densities and mobilities for *n* and *p* type silicon are shown in Table 6-1 to Table 6-5. Frequencies are in THz; mobilities are in cm^2/Vsec; resistivities are in Ω cm; multiply N by 10^{14} /cm^3 for the *n*-type and *p*-type silicon entry. To determine of the accuracy of the THz-TDS results I changed either the plasma frequency or the damping rate by ± 5%, ± 2%, and ± 1% and adjusted the other parameters to fit the data. By this process I determined that the two parameters have ± 1% accuracy and the mobility and the carrier density are determined within ± 2% accuracy.

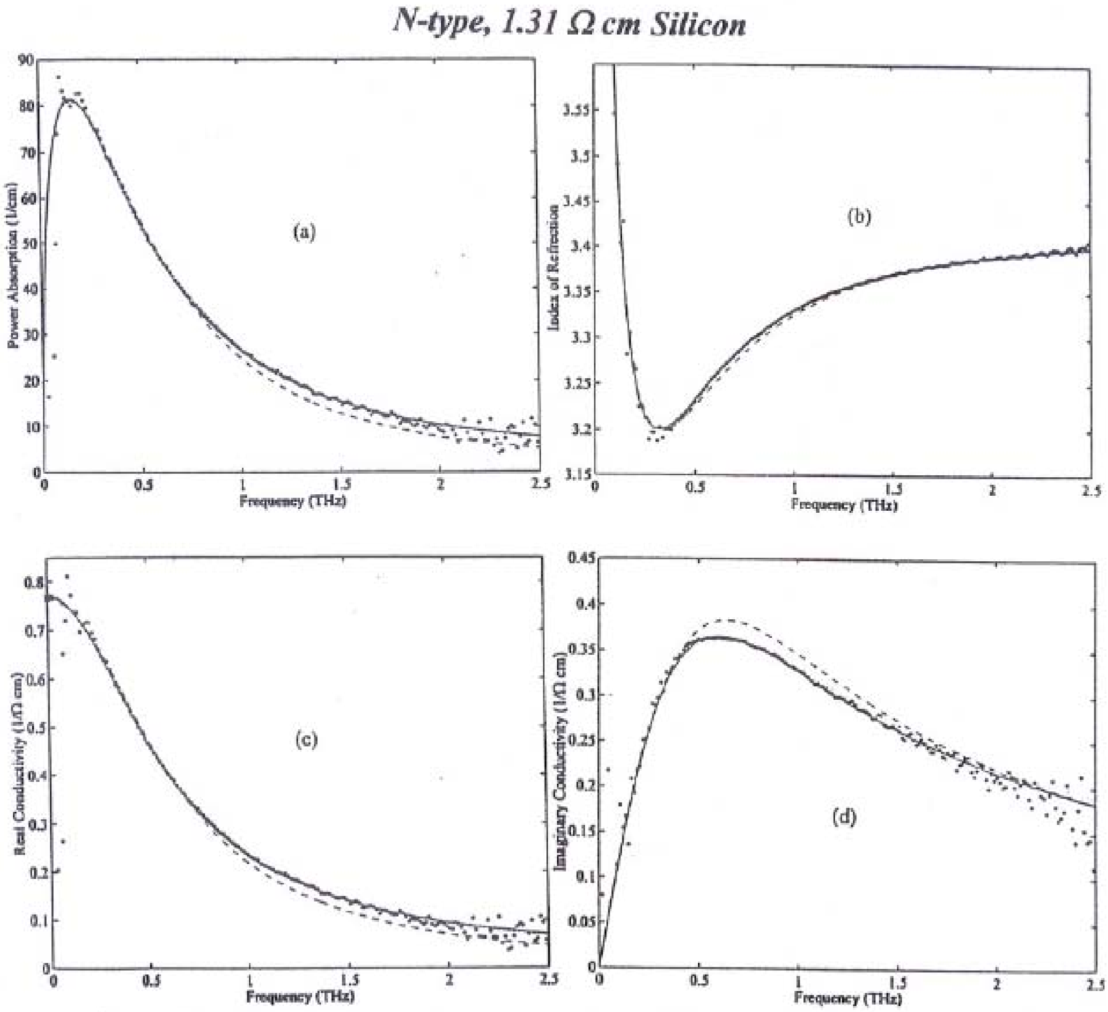

Figure 6-1. Results for 1.31 Ω cm, *n*-type silicon. Solid lines describe Cole-Davidson distribution, dashed lines describes Drude theory, and dotted lines describes scattering theory. (a) Power absorption; (b) Index of refraction; (c) Real conductivity; (d) Imaginary Conductivity.

Theories	$\omega_p/2\pi$	$\Gamma/2\pi$	β	$\Gamma_i/2\pi$	$\Gamma_l/2\pi$	**N**	μ	$1/\sigma_{dc}$
Drude	0.935	0.635	x	x	x	28	1740	1.29
Scattering	1.010	x	x	1.58	0.14	33	1420	1.29
C-D	0.873	0.550	0.89	x	x	25	1960	1.29

Table 6-1. Theoretical fitting parameters for 1.31 Ω cm, *n*-type silicon.

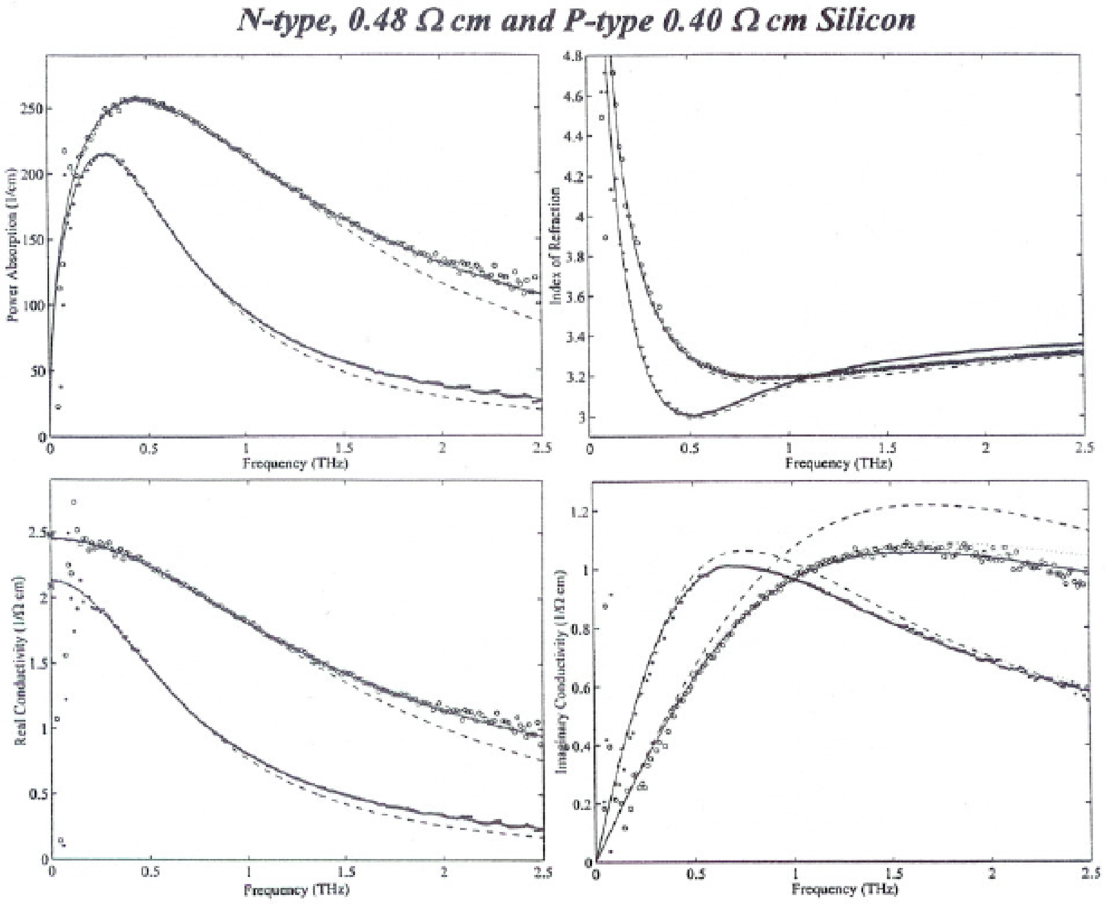

N-type, 0.48 Ω cm and P-type 0.40 Ω cm Silicon

Figure 6-2. Results for 0.48 Ω cm, *n*-type (dot) and 0.40 Ω cm, *p*-type (circle) silicon. Solid lines describe Cole-Davidson distribution, dashed lines describes Drude theory, and dotted lines describes scattering theory. (a) Power absorption; (b) Index of refraction; (c) Real conductivity; (d) Imaginary Conductivity.

Theories	$\omega_p/2\pi$	$\Gamma/2\pi$	β	$\Gamma_i/2\pi$	$\Gamma_l/2\pi$	**N**	μ	$1/\sigma_{dc}$
Drude	1.695 (2.715)	0.752 (1.68)	x (x)	x (x)	x (x)	92 (360)	1430 (450)	0.47 (0.41)
Scattering	1.829 (3.240)	x (x)	x (x)	1.75 (7.70)	0.18 (0.20)	108 (480)	1240 (310)	0.47 (0.41)
C-D	1.590 (2.355)	0.660 (1.26)	0.89 (0.73)	x (x)	x (x)	82 (250)	1630 (600)	0.47 (0.41)

Table 6-2. Theoretical fitting parameters for 0.48 Ω cm, *n*-type silicon; values in parenthesises are for 0.40 Ω cm, *p*-type silicon

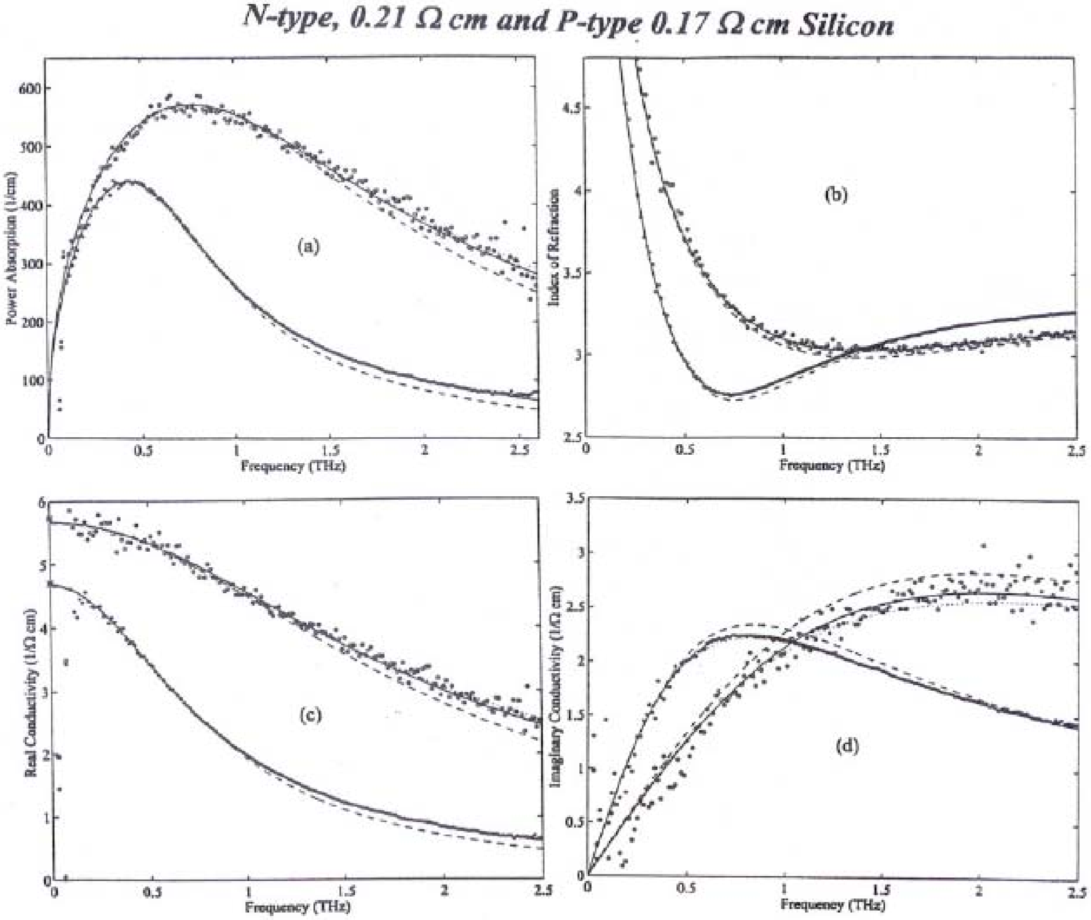
N-type, 0.21 Ω cm and P-type 0.17 Ω cm Silicon

Figure 6-3. Results for 0.21 Ω cm, *n*-type (dot) and 0.17 Ω cm, *p*-type (circle) silicon. Solid lines describe Cole-Davidson distribution, dashed lines describes Drude theory, and dotted lines describes scattering theory. (a) Power absorption; (b) Index of refraction; (c) Real conductivity; (d) Imaginary Conductivity.

Theories	$\omega_p/2\pi$	$\Gamma/2\pi$	β	$\Gamma_i/2\pi$	$\Gamma_l/2\pi$	**N**	μ	$1/\sigma_{dc}$
Drude	2.653 (4.49)	0.838 (1.98)	x (x)	x (x)	x (x)	230 (930)	1280 (380)	0.21 (0.18)
Scattering	2.863 (5.32)	x (x)	x (x)	1.98 (8.20)	0.20 (0.30)	260 (1300)	1110 (260)	0.21 (0.18)
C-D	2.530 (4.28)	0.760 (1.80)	0.91 (0.86)	x (x)	x (x)	210 (840)	1420 (420)	0.21 (0.18)

Table 6-3. Theoretical fitting parameters for 0.21 Ω cm, *n*-type silicon; values in parenthesises are for 0.17 Ω cm, *p*-type silicon.

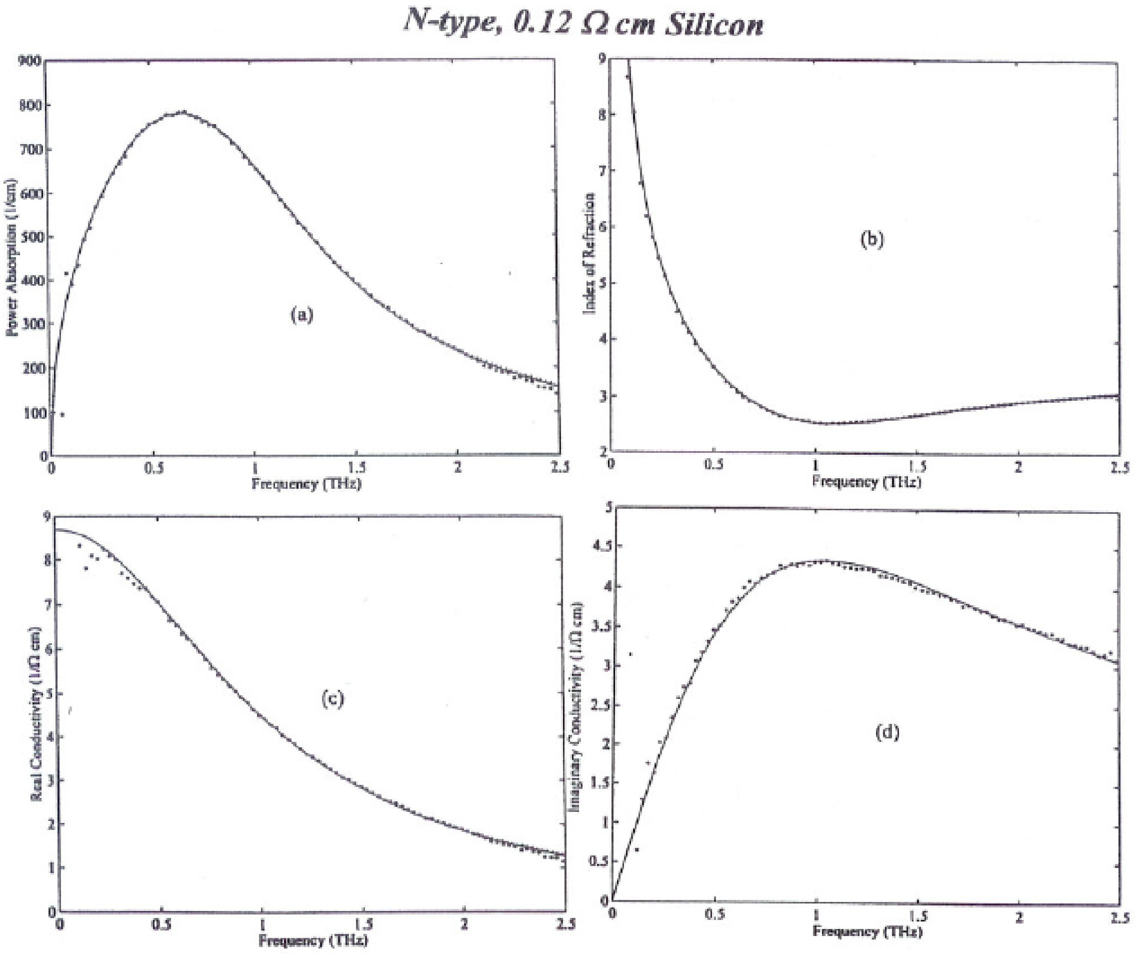

Figure 6-4. Results for 0.12 Ω cm, *n*-type silicon. Solid lines describe Cole-Davidson distribution, dashed lines describes Drude theory, and dotted lines describes scattering theory. (a) Power absorption; (b) Index of refraction; (c) Real conductivity; (d) Imaginary Conductivity.

Theories	$\omega_p/2\pi$	$\Gamma/2\pi$	β	$\Gamma_i/2\pi$	$\Gamma_l/2\pi$	**N**	μ	$1/\sigma_{dc}$
Drude	4.03	1.04	x	x	x	520	1040	0.12
Scattering	4.17	x	x	1.4	0.35	560	980	0.11
C-D	4.03	1.04	1	x	x	520	1040	0.12

Table 6-4. Theoretical fitting parameters for 0.12 Ω cm, *n*-type silicon. (Sample number 950088701)

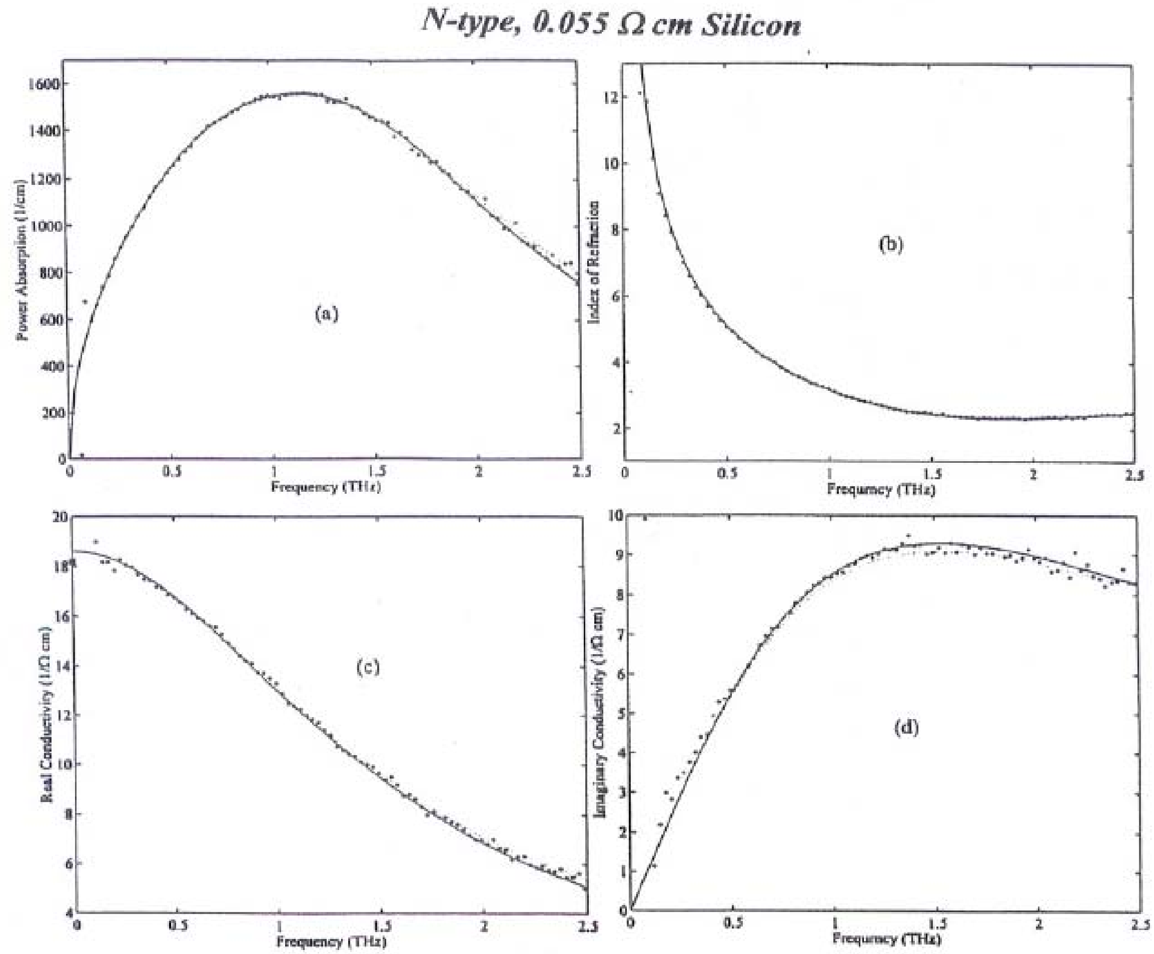

Figure 6-5. Results for 0.055 Ω cm, *n*-type silicon. Solid lines describe Cole-Davidson distribution, dashed lines describes Drude theory, and dotted lines describes scattering theory. (a) Power absorption; (b) Index of refraction; (c) Real conductivity; (d) Imaginary Conductivity.

Theories	$\omega_p/2\pi$	$\Gamma/2\pi$	β	$\Gamma_i/2\pi$	$\Gamma_l/2\pi$	**N**	μ	$1/\sigma_{dc}$
Drude	7.15	1.53	x	x	x	1600	700	0.054
Scattering	7.41	x	x	1.68	0.60	1800	650	0.054
C-D	7.15	1.53	1	x	x	1600	700	0.054

Table 6-5. Theoretical fitting parameters for 0.055 Ω cm, *n*-type silicon.

Mobility Curves

The mobilities calculated from scattering theory are in good agreement with the previous measurements [26, 27]. At low carrier densities, Cole-Davidson and Drude mobilities are much higher than the previous measurements. However, the mobilities of all theories have a good agreement for a high density of carriers as shown in Figure 6-6. All the mobility curves (Equation (4-25)) follow the Baccarani-Ostaja curve for *n*-type silicon and the Caughey-Thomas curve for *p*-type silicon. The fit parameters are shown in Table 6-6.

	μ_{max} (cm^2/Vs)	μ_{min} (cm^2/Vs)	γ	N_{ref} ($\times 10^{16}\ cm^{-3}$)
Cole-Davidson	2520 (1000)	60 (30)	0.55 (0.55)	2.5 (4.0)
Drude	2150 (780)	80 (70)	0.55 (0.68)	3.5 (5.0)
Scattering	1650 (530)	90 (50)	0.60 (0.65)	7.0 (7.5)

Table 6-6. Four parameters to determine the mobility curves of *n*-type silicon; values in parentheses are for *p*-type silicon.

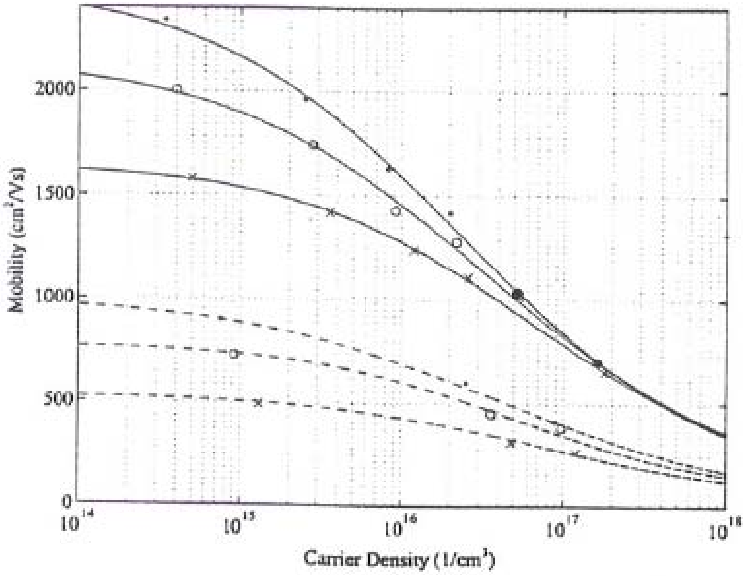

Figure 6-6. Mobilities and carrier density for the Drude theory (circles), Cole-Davidson distribution (dots) and scattering theory (x) fits to our measurement series on six *n*-type (solid lines) and three *p*-type (dashed lines) Si samples

Conclusions

Using the technique of THz time-domain spectroscopy, the frequency-dependent absorption and dispersion of a thin polyethylene film and doped *n* and *p* type silicon were measured from 0.08 THz to 2.5 THz. In the thin film measurement, the output THz pulses have multiple reflections. The magnitude of total transmission and the phase difference were strongly frequency-dependent, and this phenomenon can be explained by Fabry-Perot theory. The measurements were in good agreement with the theoretical results.

In the reflection measurement of doped silicon sample, the magnitude and the phase difference of the reflected THz pulse from the silicon sample surface was in good agreement between the measurement and the theory. By analyzing the data, I can determine the presence of a 7 μm air gap between the Si window and the Si sample. To our knowledge, this is the first broadband investigation of a doped Si sample below 2.5 THz.

Compared to earlier studies of doped silicon [7, 11], the new experimental results have sufficient precision to test alternative theories. For both *n* and *p* type silicon, Drude theory fits well with the measurement for the lowest frequencies. However, as the frequency increases beyond the carrier damping rate, $\Gamma/2\pi$, the measured power absorption and the real conductivity become significantly larger than the simple Drude theory (up to 50 percent), while the measured peak of the imaginary part, occurring approximately at $\Gamma/2\pi$, is significantly lower than the Drude result. These deviations are strongest for the lightest doping and decrease as the doping level is increased.

The scattering theory, which is one of the modified Drude theories, is a better fit than Drude theory, but there is still significant deviation at higher frequencies (up to 25 percent). The carrier relaxation in the scattering theory is due to both electron-phonon (lattice) collisions and carrier scattering from ionized impurities, and the comparison is not self-consistent. At the lowest carrier densities, where the experimental results should be fit with only lattice collisions, the results are best fit with impurity scattering as the major process and lattice scattering as the minor process. In contrast, at much higher density the relative proportion of lattice scattering must be increased (rather than decreased) to obtain reasonable agreement with the measurements.

A surprising and significant result is that all the measurements are exceptionally well fit by the Cole-Davidson distribution, which corresponds to Drude theory with a fractional exponent of the distribution parameter β. Drude theory uses a single sided exponential exp $(-t/\tau)$ with one relaxation time τ. However, for C-D case the time-domain response function changes to one with a much faster initial decay which asymptotically approaches the Drude theory. The distribution parameter β approaches unity for *n*-type and *p*-type silicon as the number density of carriers is increased. The Drude theory was derived from the Debye equation and the empirical C-D distribution was derived from a modified Debye equation [29, 37]. To our knowledge, this is the first application of the C-D distribution to semiconductor research.

The investigation of the important low frequency range for the high resistivity sample was measured using a GaAs Bowtie 30^{o} transmitter and SOS 10-80-10 receiver. Due to the frequency response of THz-TDS system, the data is considered reliable above 0.08 THz frequency. For the low resistivity silicon samples, the strong absorption and dispersion lie above 2.5 THz. An earlier absorption measurement [23] of doped *n* type silicon with synchrotron radiation source and bolometric power detection has excellent agreement with our *n* type high resistivity sample and they extended the measurement up to 6 THz frequency range.

CHAPTER VII

REFERENCES

1. F. M. Smits, “Measurements of Sheet Resistivities with the Four-Point Probe,” Bell system Technical Journal, Vol. 37, 711-718 (1958).

2. L. J. Van der Pauw, “A Method of Measuring Specific Resistivity and Hall Effect of Discs of Arbitrary Shape,” Philips Research Reports, Vol. 13, 1-9 (1958).

3. J. Lange, “Method for Hall Mobility and Resistivity Measurements on Thin Layers,” J. Appl. Phys., Vol. 35, No. 9, 2659-2664 (1964).

4. L. B. Valdes, “Resistivity Measurements on Germanium for Transistors,” Proc. Institute of Radio Engineers, Vol. 42, 420-427 (1954).

5. R. T. Kinasewitz and B. Senitzky, “Investigation of the Complex Permittivity of N-type Silicon at Millimeter Wavelengths,” J. Appl. Phys., Vol. 54, 3394-3398 (1983).

6. J. D. Holm and K. S. Champlin, “Microwave Conductivity of Silicon and Germanium,” J. Appl. Phys., Vol 39, 275-284 (1968).

7. M. van Exter and D. Grischkowsky, “Optical and Electronic Properties of Doped Silicon From 0.1 to 2 THz,” Appl. Phys. Lett., Vol. 56, NO. 17, 1694-1696 (1990).

8. D. Grischkowsky, S. Keiding, M. van Exter, and Ch. Fattiger, “Far-infrared Time-domain Spectroscopy with Terahertz Beams of Dielectrics and Semiconductors,” J. Opt. Soc. Am. B, Vol. 7, No. 10, 2006-2015 (1990).

9. N. Katzenellenbogen and D. Grischkowsky, “Electrical Characterization to 4 THz of N- and P-type GaAs using THz time-domain spectroscopy,” Appl. Phys. Lett., Vol. 61, 840-842 (1992).

10. M. Vindevoghel, J. Vindevoghel, and Y. Leroy, “Mean Momentum Relaxation Time and Scattering Processes from Absorption Spectra in Millimeteric and Far Infrared Ranges,” Infrared Physics, Vol. 15, 161-173 (1975).

11. M. van Exter and D. Grischkowsky, “Carrier Dynamic of Electrons and Holes in Moderated Doped Silicon,” Phys. Rev. B, Vol. 41, No. 17, 12140-12149 (1990).

12. R. A. Smith, “Semiconductors,” Cambridge University Press (1959).

13. D. W. Davidson and R. H. Cole, “Dielectric Relation in Glycerine,” J. Chem. Phys., Vol. 8, 1417 (1950).

14. B. Gross, “Dielectric Relaxation and the Davidson-Cole Distribution Function,” J. Appl. Phys., Vol. 57, 2331-2333 (1985).

15. K. Pathmanathan and J. R. Stevens, “Improved Analysis of Ionic Conductivity Relaxation using the Electric Modulus with a Cole-Davidson Distribution,” J. Appl. Phys., Vol. 68, 5128-5132 (1990).

16. M. van Exter, Ch. Fattinger, and D. Grischkowsky, “High-brightness Terahertz Beam Characterized with an Ultrafast Detector,” Appl. Phys. Lett., Vol. 55, 337-339 (1989).

17. M. van Exter, Ch. Fattinger, and D. Grischkowsky, “Terahertz Time-Domain Spectroscopy of Water Vapor,” Optics Lett., Vol. 14, No. 20, 1128-1130 (1989).

18. M. van Exter, and D. Grischkowsky, “Characterization of an Optoelectronic Terahertz Beam System,” IEEE Trans. Microwave Theory Tech., Vol. 38, No. 11, 1684-1691 (1990).

19. B. W. Nicholson, “Ranging Studies with an Ultra-Wideband, Pulsed, Optoelectronic THz Beam System,” Thesis of Master of Since. (1995).

20. R. A. Cheville and D. Grischkowsky, “Far-Infrared Terahertz Time-Domain Spectroscopy of Flames,” Opti. Lett., Vol. 20, No. 15, 1646-1648 (1995).

21. M. Born and E. Wolf, “Principle of Optics,” Pergamon Press, Oxford, (1987).

22. T. Kihara and K. Yokomori, “Simultaneous Measurement of Refractive Index and Thickness of Thin Film by Polarized Reflectances,” Appl. Opti., Vol. 29, No. 34, 5069-5073 (1990).

23. T. Ohba and S. Ikawa, “Far-infrared Absorption of Silicon Crystals,” J. Appl. Phys., Vol. 64, 4141-4143 (1988).

24. G. W. Chantry, “Properties of Dielectric Materials,” in *Infrared and Millimeter Waves* Vol. 8, Academic Press, New York, (1983).

25. R. N. Dexter, H. J. Zeiger, and B. Lax, “Cyclotron Resonance Experiments in Silicon and Germanium,” Phys. Rev., Vol. 104, No. 3, 637-644 (1956).

26. G. Baccarani and P. Ostoja, “Electron Mobility Empirically Related to the Phosphorus Concentration in Silicon,” Solid-State Electronics, Vol. 18, 579-580 (1975).

27. D. M. Caughey and R. F. Thomas, “Carrier Mobilities in Silicon Empirically Related to Doping and Field,” Proc. IEEE, Vol. 50, 2192-2193 (1967).

28. D. W. Davisdon and R. H. Cole, “Dielectric Relaxation in Glycerol, Propylene Glycol, and *n*-Propanol,” J. Chem. Phys., Vol. 19, No. 12, 1484-1490 (1951).

29. “McGraw-Hill Encyclopedia of Science & Technology”, McGraw-Hill, Vol. 13, 246-253 (1992).

30. D. Grischkowsky and N. Katzenellenbogen, “Femtosecond Pulses of Terahertz Radiation: Physics and Applications,” OSA Proceedings on Picosecond Electronics and Optoelectronics, Vol. 9. 9-14 (1991).

31. C. Jacoboni, C. Canali, G. Ottaviani and A. Alberigi Quaranta, “A Review of Some Charge Transport Properties of Silicon,” Solid-State Electronics, Vol. 20, 77-89 (1977).

32. G. W. Chantry, J. W. Fleming, and P. M. Dmith, “Far Infrared and Millimetre-Wave Absorption Spectra of Some Low-Loss Polymers,” Chem. Phys. Lett., Vol. 10, No. 4, 473-477 (1971).

33. A. Renfrew and P. Morgan, “Polythene,” Iliffe & Sons Ltd., Second Edition, (1960).

34. J. W. Shackleton, “General Charcateristics of Polyethylene,” Trans. Am. Inst. Elec. Engi., Vol. 64, 912-916 (1945).

35. R. R. Tummala and E. J. Rymazewski, “Microelectronics packaging handbook,” van Nostrand Reinhold, New York, (1980).

36. G. W. Chantry, H. M. Evans, J. W. Fleming, and H.A. Gebbie, “TPX, a new Material for Optical Components in the Far Infra-Red Spectral Region,” Infrared Physics, Vol. 9, 31-33 (1969).

37. E. Sanchez Martinez, R. Diaz Calleja, and W. Gunber, “Complex Polarizability as used to Analyze Dielectric Relaxation Measurements,” Colloid Polymer Sci., Vol. 270, 146-153 (1992)

38. K. W. Boer, “Survey of Semiconductor Physics,” Van Nostrand Reinhold, New York, (1990).

39. S. M. Sze, “Physics of semiconductor Devices,” John Wiley & Sons, New York, (1981).

40. R. C. Miller and D. A. Kleinman, “Excitons in GaAs Quantum Wells,” J. Lumin., Vol. 30, 520-540 (1985).

41. K. Ploog and G. H. Dohler, “Compositional and Doping Superlattices in III-V Semiconductors,” Adv. Phys., Vol. 32, No. 3, 285-359 (1983).

42. R. Dingle, W. Wiegmann, and C. H. Henry, “Quantum States of Confined Carriers in Very Thin $Al_xGa_{1-x}As$-GaAs-$Al_xGa_{1-x}As$ Heterostructures,” Phys. Rev. Lett., Vol. 33, 827-830 (1974).

APPENDIX A

CALCULATION OF MAGNITUDE AND PHASE SHIFT OF THIN FILM MEASUREMENT

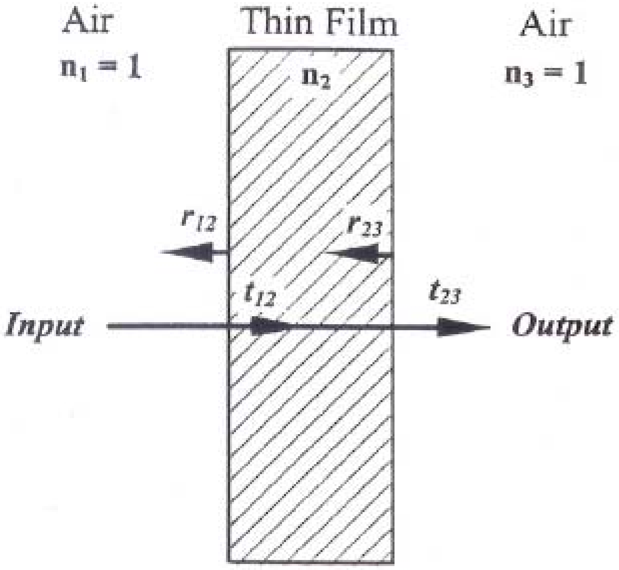

Figure A-1. Propagation of the THz pulse through the thin film.

The reflection and transmission coefficients are

$$r_{12} = \frac{n_1 - n_2}{n_1 + n_2},\quad r_{23} = \frac{n_2 - n_3}{n_2 + n_3},\quad t_{12} = \frac{2n_1}{n_1 + n_2}, \text{ and } t_{23} = \frac{2n_2}{n_2 + n_3}$$

The complex amplitude transmission of a free standing absorptive thin film is given by [21]

$$t = \frac{t_{12}t_{23}\exp(-\alpha d/2)\exp(i\beta_o)}{1 + r_{12}r_{23}\exp(-\alpha d)\exp(i2\beta_o)} \tag{A-1}$$

where α is an absorption coefficient, and $\beta_o = 2\pi n_2 d/\lambda_o$. λ_o is the free space wavelength.

$$t = \frac{t_{12}t_{23}\exp(-\alpha d/2)\exp(i\beta_o)\left(1 + r_{12}r_{23}\exp(-\alpha d)\exp(-i2\beta_o)\right)}{\left(1 + r_{12}r_{23}\exp(-\alpha d)\exp(i2\beta_o)\right)\left(1 + r_{12}r_{23}\exp(-\alpha d)\exp(-i2\beta_o)\right)}$$

$$= \frac{t_{12}t_{23}\exp(-\alpha d/2)\exp(i\beta_o)\left[1 + r_{12}r_{23}\exp(-\alpha d)\cos(2\beta_o) - ir_{12}r_{23}\exp(-\alpha d)\sin(2\beta_o)\right]}{1 + r_{12}^2 r_{23}^2\exp(-2\alpha d) + 2r_{12}r_{23}\exp(-\alpha d)\cos(2\beta_o)}$$

let $\left[1+r_{12}r_{23}\exp(-\alpha d)\cos(2\beta_o)-ir_{12}r_{23}\exp(-\alpha d)\sin(2\beta_o)\right]=A\exp(i\phi)$ (A-2)

where $A=\left[\left\{1+r_{12}r_{23}\exp(-\alpha d)\cos(2\beta_o)\right\}^2+r_{12}^2r_{23}^2\exp(-2\alpha d)\sin^2(2\beta_o)\right]^{1/2}$

$$=\left[1+r_{12}^2r_{23}^2\exp(-2\alpha d)+2r_{12}r_{23}\exp(-\alpha d)\cos(2\beta_o)\right]^{1/2}$$

$$t=\frac{t_{12}t_{23}\exp(-\alpha d/2)\exp(i\beta_o)\exp(i\phi)A}{1+r_{12}^2r_{23}^2\exp(-2\alpha d)+2r_{12}r_{23}\exp(-\alpha d)\cos(2\beta_o)}$$

The total transmission is

$$t=\frac{t_{12}t_{23}\exp(-\alpha d/2)\exp(i\beta_o)\exp(i\phi)}{\left[1+r_{12}^2r_{23}^2\exp(-2\alpha d)+2r_{12}r_{23}\exp(-\alpha d)\cos(2\beta_o)\right]^{1/2}} \qquad \text{(A-3)}$$

where the amplitude transmission is given by

$$|t|=\frac{t_{12}t_{23}\exp(-\alpha d/2)}{\left[1+r_{12}^2r_{23}^2\exp(-2\alpha d)+2r_{12}r_{23}\exp(-\alpha d)\cos(2\beta_o)\right]^{1/2}} \qquad \text{(A-4)}$$

In this case $n_1 = n_3$, $t_{23} = t_{21}$ and $r_{12} = -r_{23}$

$$|t|=\frac{t_{12}t_{21}\exp(-\alpha d/2)}{\left[1+r_{12}^4\exp(-2\alpha d)-2r_{12}^2\exp(-\alpha d)\cos(2\beta_o)\right]^{1/2}}$$

$$=\frac{t_{12}t_{21}\exp(-\alpha d/2)}{\left[\left\{1+r_{12}^4-2r_{12}^2\cos(2\beta_o)\right\}+r_{12}^4\left\{\exp(-2\alpha d)-1\right\}-2r_{12}^2\left\{\exp(-\alpha d)-1\right\}\cos(2\beta_o)\right]^{1/2}}$$

let $D=1+r_{12}^4-2r_{12}^2\cos(2\beta_o)$

$$|t|=\left(\frac{t_{12}t_{21}}{\sqrt{D}}\right)\frac{\exp(-\alpha d/2)}{\left[1+\dfrac{\left\{r_{12}^4\left(\exp(-2\alpha d)-1\right)-2r_{12}^2\left(\exp(-\alpha d)-1\right)\cos(2\beta_o)\right\}}{D}\right]^{1/2}}$$

where $r^2_{12} < 1$ and $r^4_{12} << 1$, consider only the first order terms of the denominator

$$|t| = \left(\frac{t_{12}t_{21}}{\sqrt{D}}\right)\exp\left(-\alpha d/2\right)\left[1-\frac{1}{2}\frac{\left\{r_{12}^{4}\left(\exp\left(-2\alpha d\right)-1\right)-2r_{12}^{2}\left(\exp\left(-\alpha d\right)-1\right)\cos\left(2\beta_{o}\right)\right\}}{D}\right]$$

$$= \left(\frac{t_{12}t_{21}}{\sqrt{D}}\right)\left[\left\{\exp\left(-\alpha d/2\right)-1\right\}+1\right]\left[1-\frac{1}{2}\frac{\left\{r_{12}^{4}\left(\exp\left(-2\alpha d\right)-1\right)-2r_{12}^{2}\left(\exp\left(-\alpha d\right)-1\right)\cos\left(2\beta_{o}\right)\right\}}{D}\right]$$

consider only the first order terms

$$|t| = \left(\frac{t_{12}t_{21}}{\sqrt{D}}\right)\left[1+\left\{\exp\left(-\alpha d/2\right)-1\right\}-\frac{1}{2}\frac{\left\{r_{12}^{4}\left(\exp\left(-2\alpha d\right)-1\right)-2r_{12}^{2}\left(\exp\left(-\alpha d\right)-1\right)\cos\left(2\beta_{o}\right)\right\}}{D}\right]$$

$$= \left(\frac{t_{12}t_{21}}{\sqrt{D}}\right)\left[1-\frac{\alpha d}{2}-\frac{1}{2}\frac{\left\{r_{12}^{4}\left(-2\alpha d\right)-2r_{12}^{2}\left(-\alpha d\right)\cos\left(2\beta_{o}\right)\right\}}{D}\right]$$

$$= \left(\frac{t_{12}t_{21}}{\sqrt{D}}\right)\left[1-\frac{\left(\alpha d/2\right)\left(1+r_{12}^{4}-2r_{12}^{2}\cos\left(2\beta_{o}\right)\right)}{D}-\frac{\alpha d\left(-r_{12}^{4}+r_{12}^{2}\cos\left(2\beta_{o}\right)\right)}{D}\right]$$

$$= \left(\frac{t_{12}t_{21}}{\sqrt{D}}\right)\left[1-\frac{\left(\alpha d\right)\left(\frac{1}{2}+\frac{1}{2}r_{12}^{4}-r_{12}^{2}\cos\left(2\beta_{o}\right)\right)}{D}-\frac{\alpha d\left(-r_{12}^{4}+r_{12}^{2}\cos\left(2\beta_{o}\right)\right)}{D}\right]$$

$$= \left(\frac{t_{12}t_{21}}{\sqrt{D}}\right)\left[1-\frac{\left(\alpha d\right)\left(\frac{1}{2}-\frac{1}{2}r_{12}^{4}\right)}{D}\right]$$

therefore the magnitude shift is

$$|t| = \left(\frac{t_{12}t_{21}}{\sqrt{D}}\right)\left[1-\frac{\frac{\alpha d}{2}\left(1-r_{12}^{4}\right)}{D}\right] \qquad \text{(A-5)}$$

From Equation (A-2), the phase term is given by

$$\sin\phi = \frac{-r_{12}r_{23}\exp(-\alpha d)\sin(2\beta_o)}{A} \tag{A-6}$$

$$\cos\phi = \frac{1 + r_{12}r_{23}\exp(-\alpha d)\cos(2\beta_o)}{A} \tag{A-7}$$

$$\tan\phi = \frac{-r_{12}r_{23}\exp(-\alpha d)\sin(2\beta_o)}{1 + r_{12}r_{23}\exp(-\alpha d)\cos(2\beta_o)} \tag{A-8}$$

in this case $r_{23} = -r_{12}$

$$\tan\phi = \frac{r_{12}^2\exp(-\alpha d)\sin(2\beta_o)}{1 - r_{12}^2\exp(-\alpha d)\cos(2\beta_o)}$$

$$= \frac{r_{12}^2\exp(-\alpha d)\sin(2\beta_o)}{\left(1 - r_{12}^2\cos(2\beta_o)\right) - r_{12}^2\left(\exp(-\alpha d) - 1\right)\cos(2\beta_o)}$$

$$= \frac{r_{12}^2\exp(-\alpha d)\sin(2\beta_o)}{\left(1 - r_{12}^2\cos(2\beta_o)\right)\left[1 - \frac{r_{12}^2\left(\exp(-\alpha d) - 1\right)\cos(2\beta_o)}{1 - r_{12}^2\cos(2\beta_o)}\right]}$$

consider only the first order terms

$$= \frac{r_{12}^2\exp(-\alpha d)\sin(2\beta_o)}{\left(1 - r_{12}^2\cos(2\beta_o)\right)}\left[1 + \frac{r_{12}^2\left(\exp(-\alpha d) - 1\right)\cos(2\beta_o)}{1 - r_{12}^2\cos(2\beta_o)}\right] \tag{A-9}$$

in this case α << 1 and $r_{12}^2\cos(2\beta_o)$ << 1.

$$\tan\phi = \frac{r_{12}^2\sin(2\beta_o)}{\left(1 - r_{12}^2\cos(2\beta_o)\right)} = r_{12}^2\sin(2\beta_o) \tag{A-10}$$

Therefore the phase shift is

$$\phi = \tan^{-1}\left(r_{12}^2\sin(2\beta_o)\right)$$

APPENDIX B

MEASURED THz PULSES OF *N* AND *P* TYPE SILICON SAMPLES

Figure B-1 shows measured THz pulses of the highest resitivity *p* type silicon using a GaAS Bowtie 30^o transmitter and SOS 10-80-10 receiver. Figure B-2 to Figure B-9 show measured THz pulse of the *n* and *p* type silicon samples using a GaAs 10-80-10 transmitter and SOS 10-30-10 receiver.

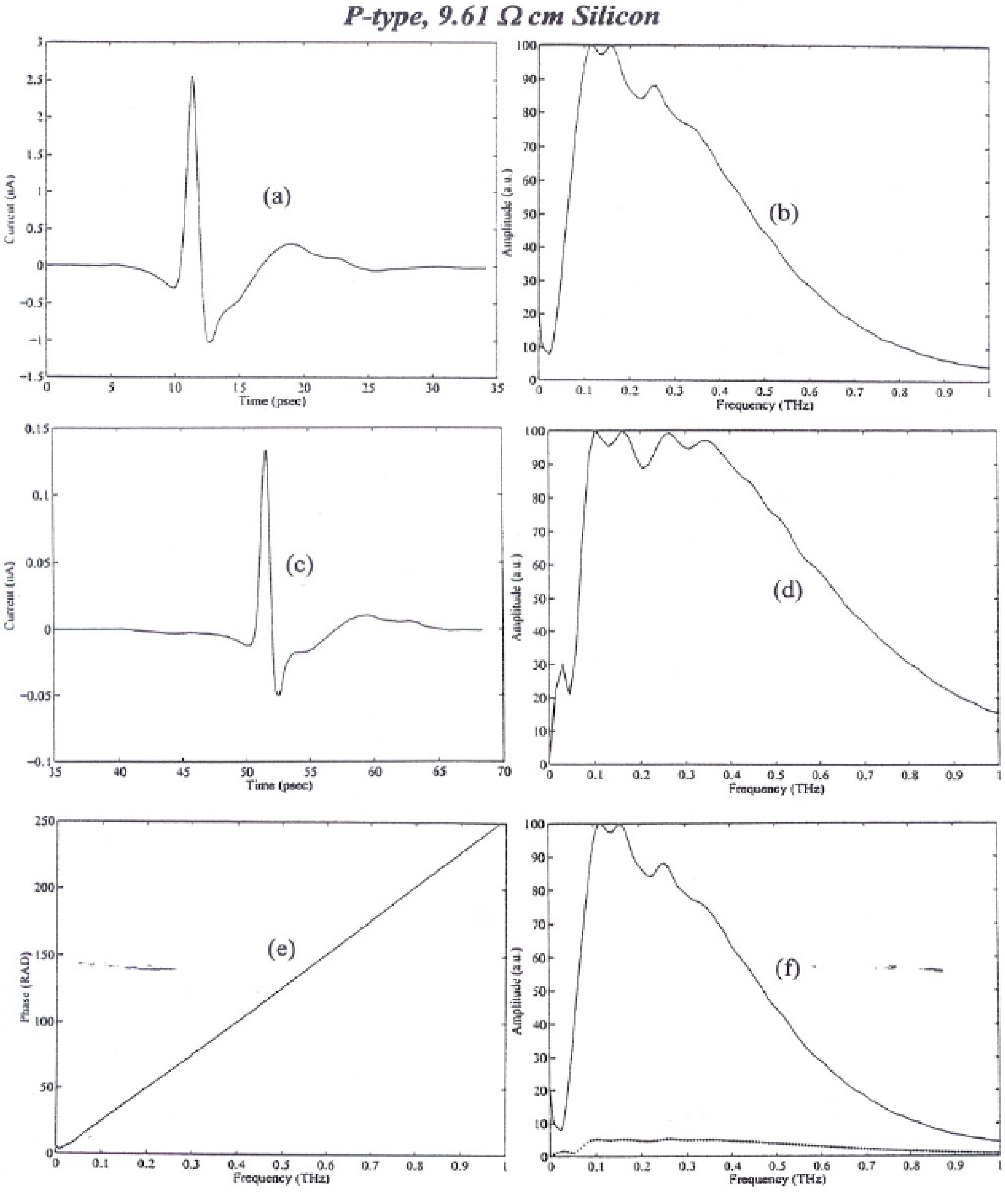

Figure B-1. 9.61 Ω cm, *p*-type silicon measured by GaAs Bowtie 30° transmission and SOS 10-80-10 receiver. (a) input THz pulse; (b) Normalized amplitude spectrum of (a); (c) output THz Pulse; (d) Normalized amplitude spectrum of (c); (e) The phase difference; (f) compare two amplitude spectra; input(solid line) and output (dashed line).

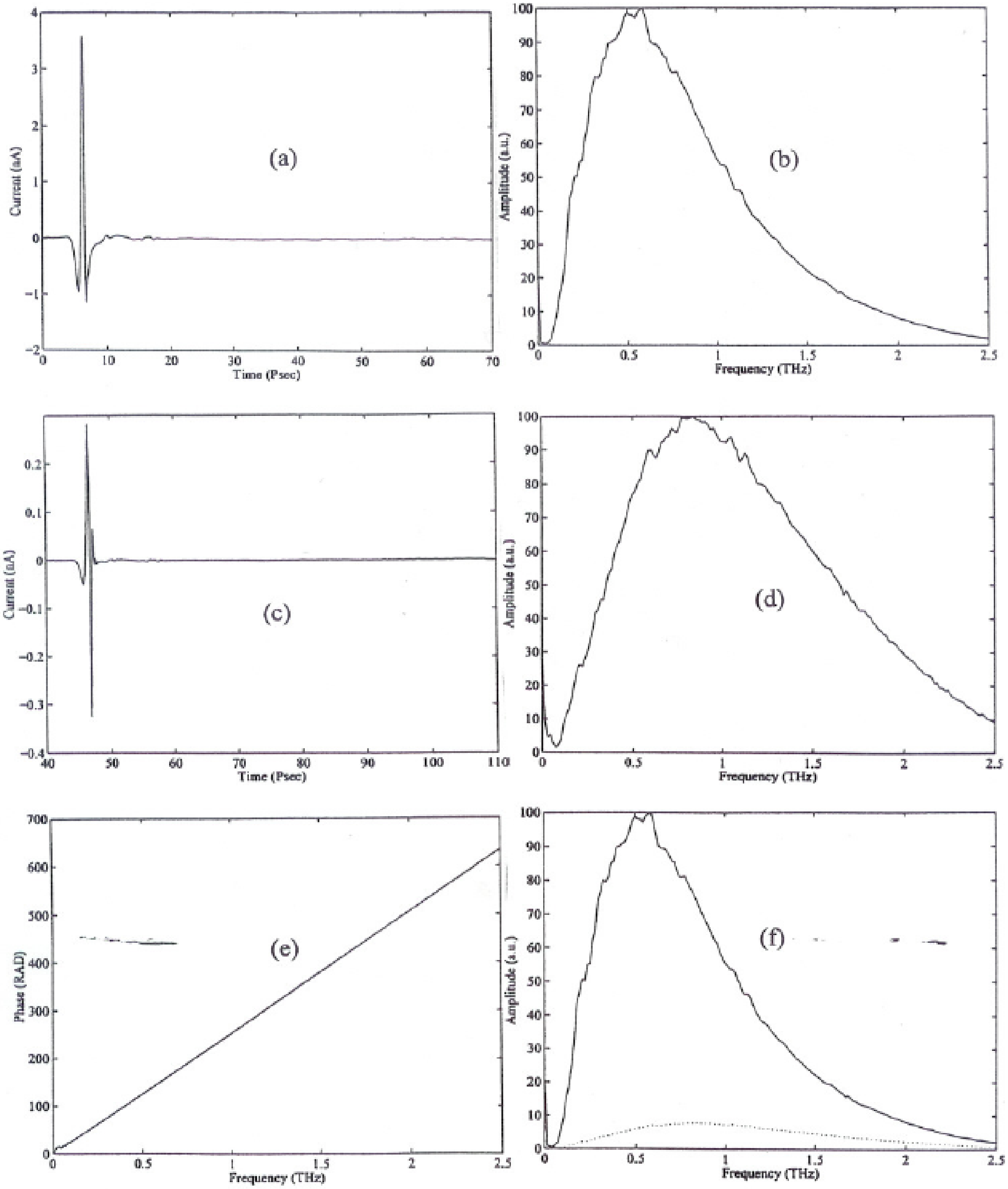

Figure B-2. 9.61 Ω cm, *p*-type silicon measured by GaAs 10-80-10 transmission and SOS 10-30-10 receiver. (a) input THz pulse; (b) Normalized amplitude spectrum of (a); (c) output THz Pulse; (d) Normalized amplitude spectrum of (c); (e) The phase difference; (f) compare two amplitude spectra; input(solid line) and output (dashed line).

N-type, 1.31 Ω cm Silicon

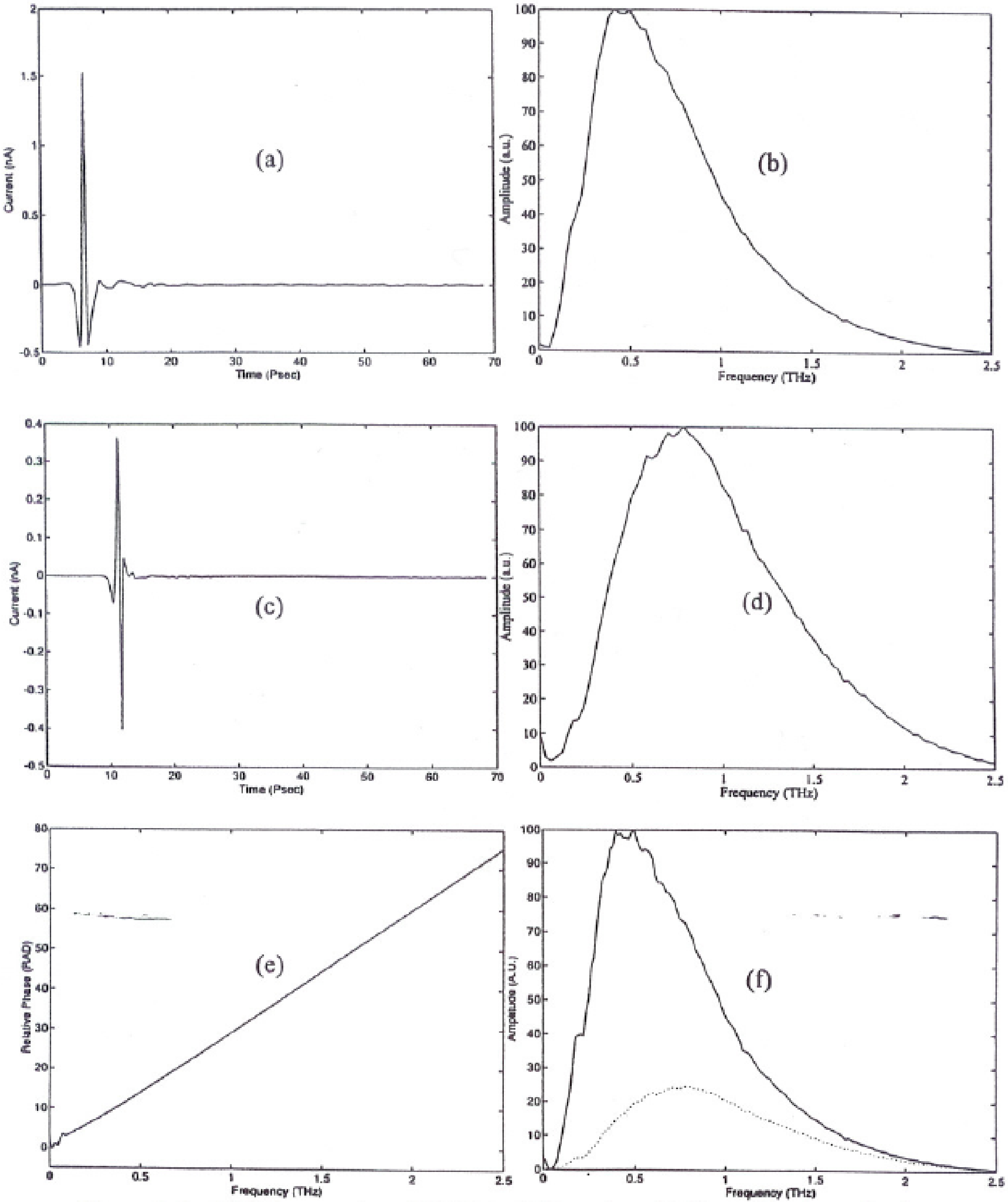

Figure B-3. 1.31 Ω cm, *n*-type Si (a) input THz pulse; (b) Normalized amplitude spectrum of (a); (c) output THz Pulse; (d) Normalized amplitude spectrum of (c); (e) The phase difference; (f) compare two amplitude spectra; input(solid line) and output (dashed line).

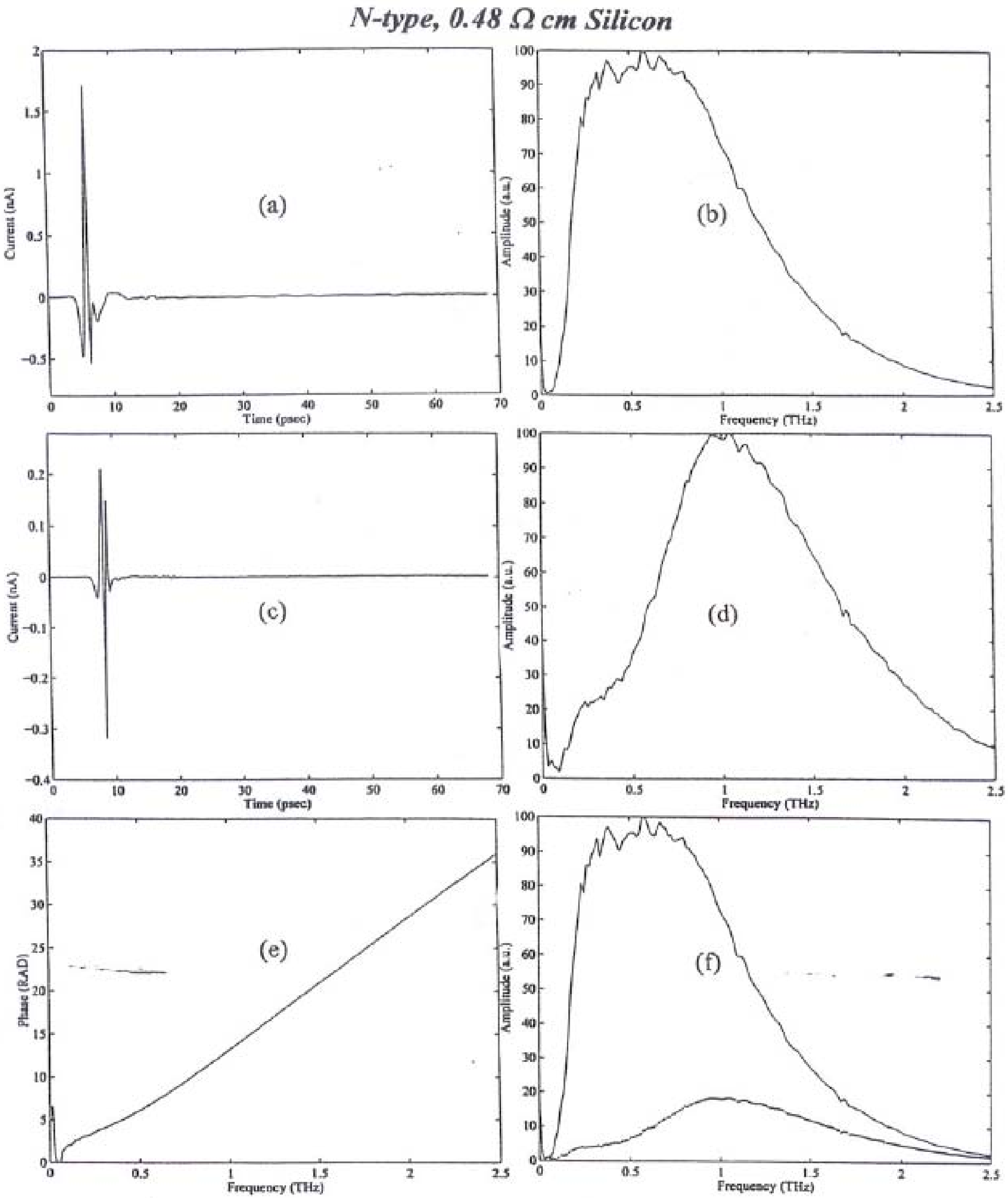

Figure B-4. 0.48 Ω cm, *n*-type Si (a) input THz pulse; (b) Normalized amplitude spectrum of (a); (c) output THz Pulse; (d) Normalized amplitude spectrum of (c); (e) The phase difference; (f) compare two amplitude spectra; input(solid line) and output (dashed line).

P-type 0.40 Ω cm Silicon

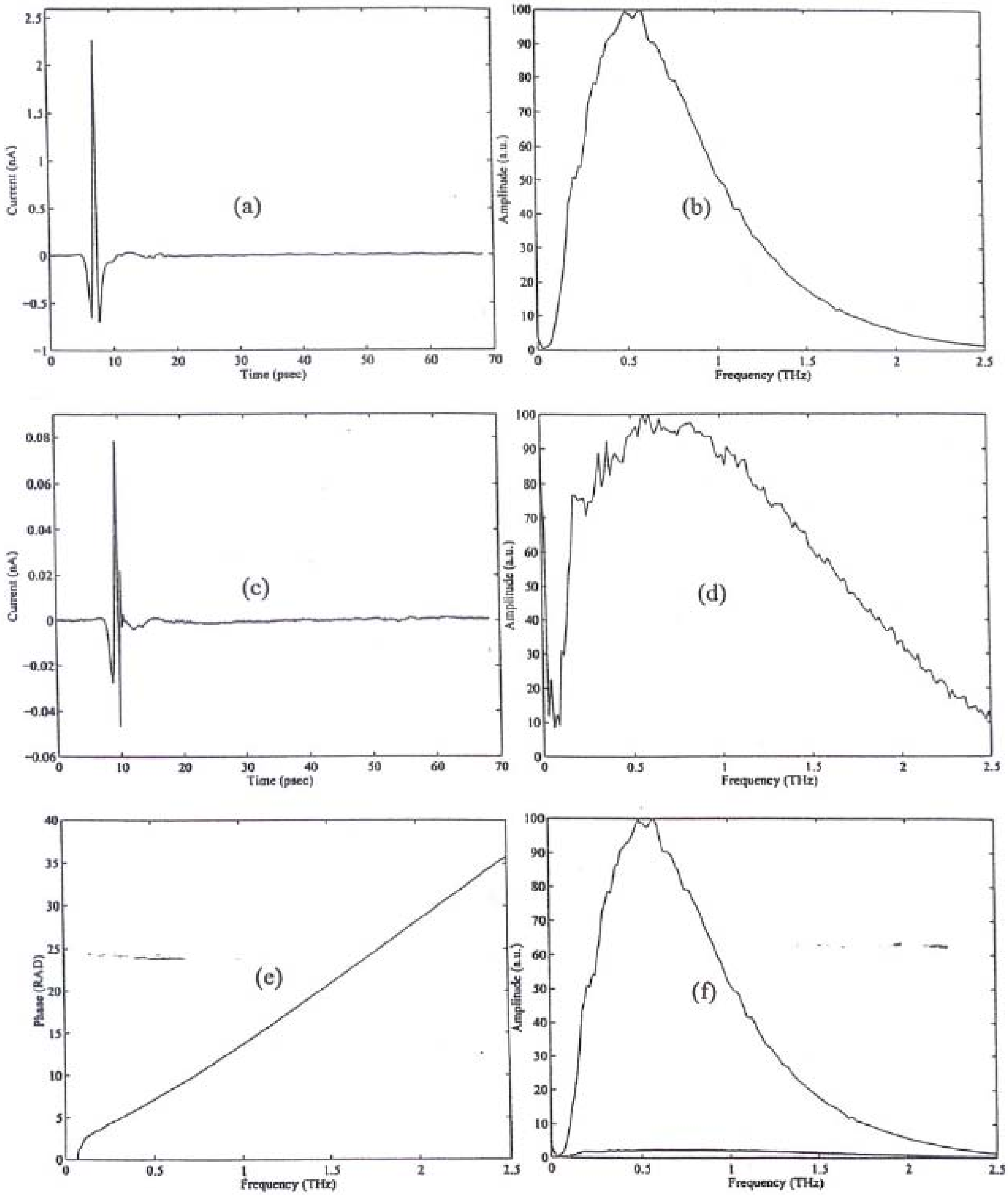

Figure B-5. 0.40 Ω cm, *p*-type Si (a) input THz pulse; (b) Normalized amplitude spectrum of (a); (c) output THz Pulse; (d) Normalized amplitude spectrum of (c); (e) The phase difference; (f) compare two amplitude spectra; input(solid line) and output (dashed line).

N-type, 0.21 Ω cm Silicon

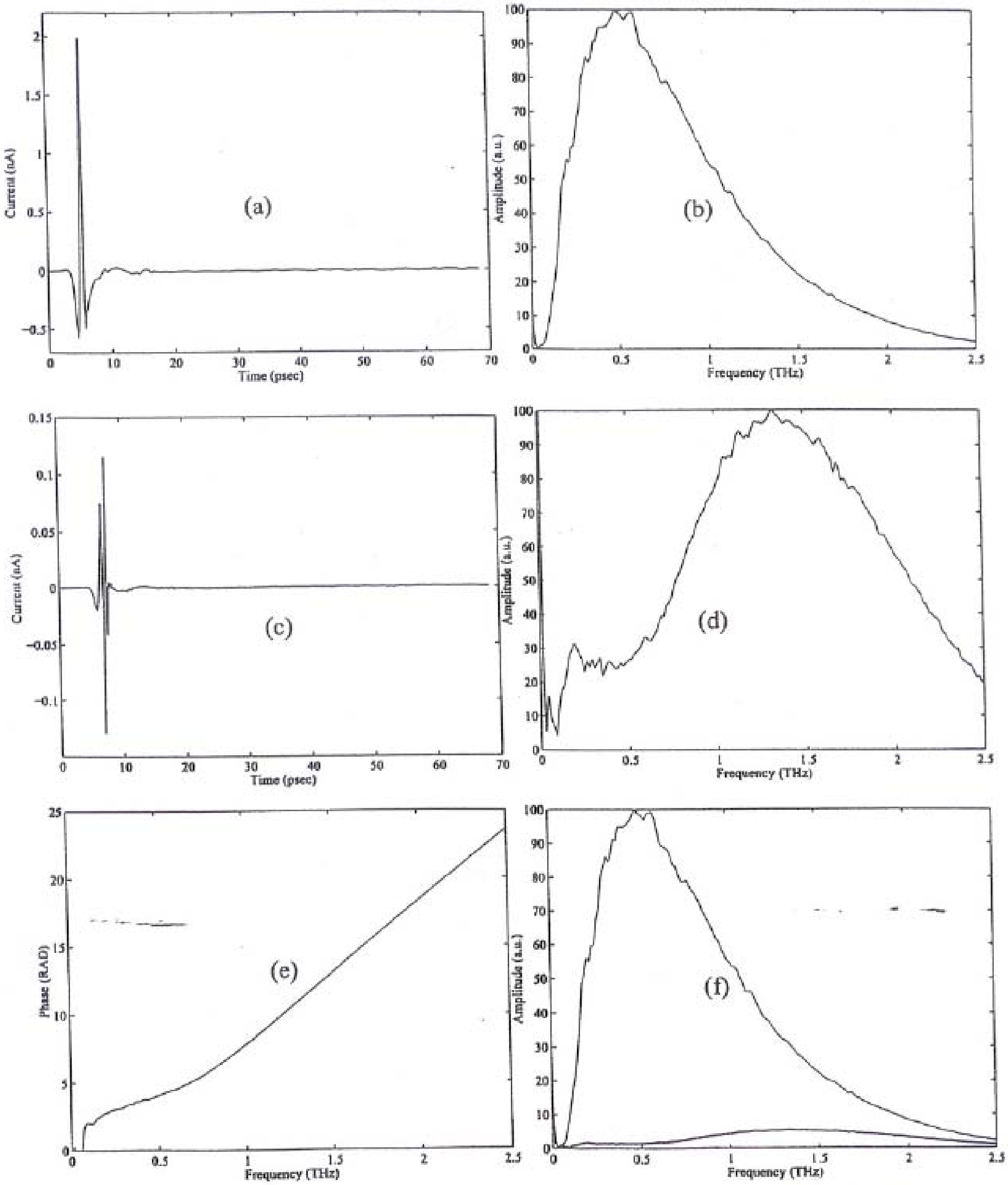

Figure B-6. 0.21 Ω cm, *n*-type Si (a) input THz pulse; (b) Normalized amplitude spectrum of (a); (c) output THz Pulse; (d) Normalized amplitude spectrum of (c); (e) The phase difference; (f) compare two amplitude spectra; input(solid line) and output (dashed line).

P-type 0.17 Ω cm Silicon

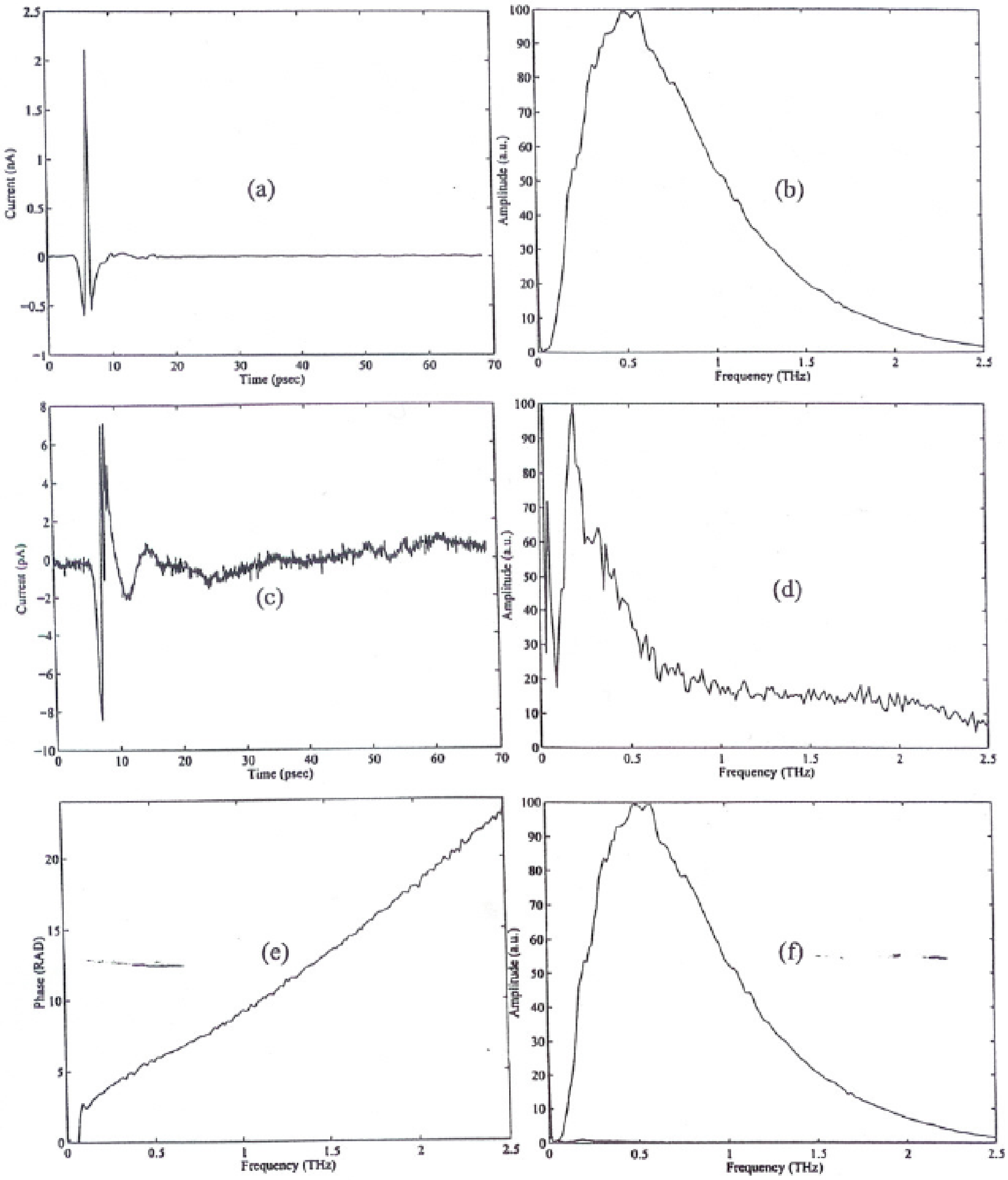

Figure B-7. 0.17 Ω cm, *p*-type Si (a) input THz pulse; (b) Normalized amplitude spectrum of (a); (c) output THz Pulse; (d) Normalized amplitude spectrum of (c); (e) The phase difference; (f) compare two amplitude spectra; input(solid line) and output (dashed line).

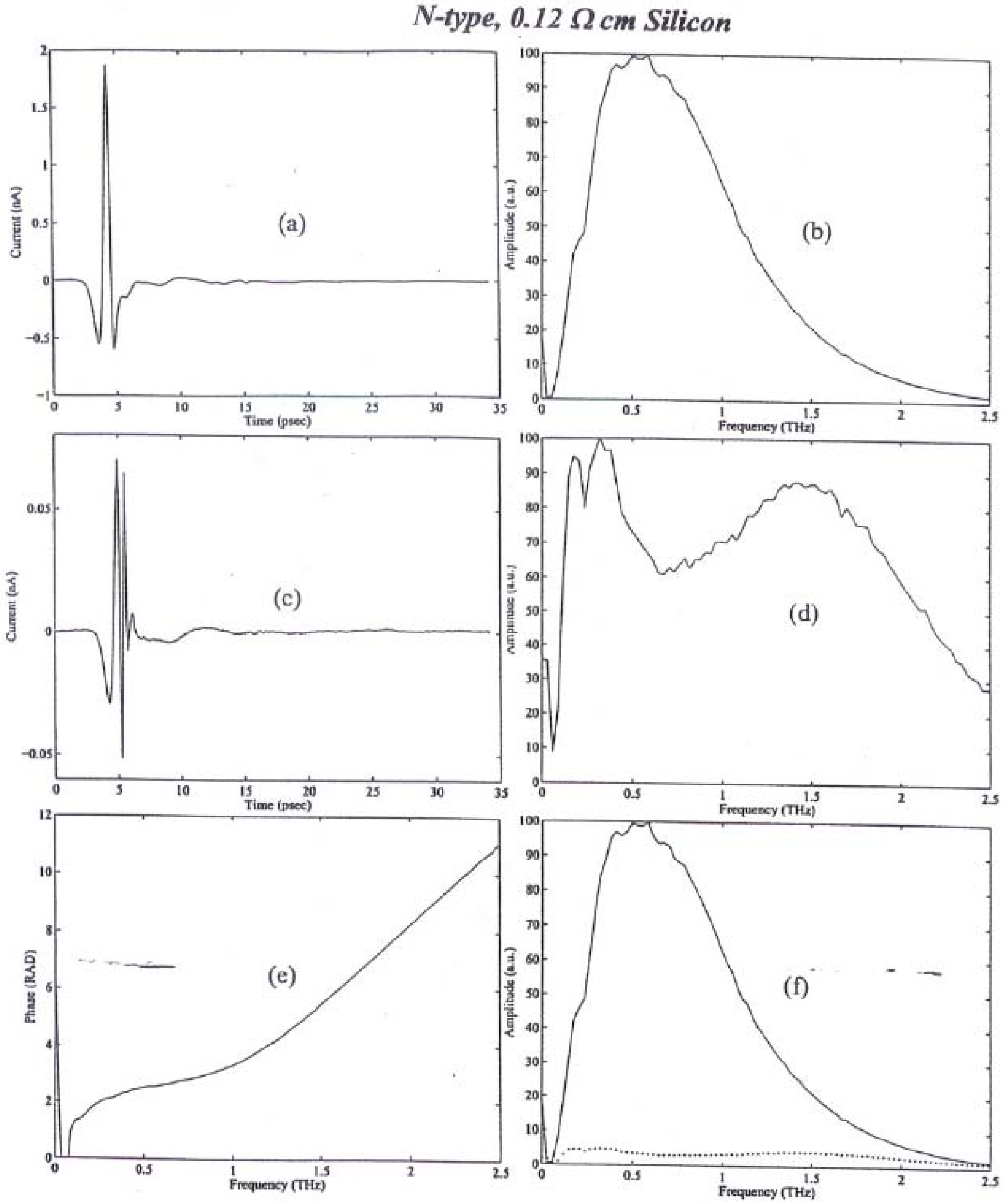

Figure B-8. 0.12 Ω cm, *n*-type Si (a) input THz pulse; (b) Normalized amplitude spectrum of (a); (c) output THz Pulse; (d) Normalized amplitude spectrum of (c); (e) The phase difference; (f) compare two amplitude spectra; input(solid line) and output (dashed line).

N-type, 0.055 Ω cm Silicon

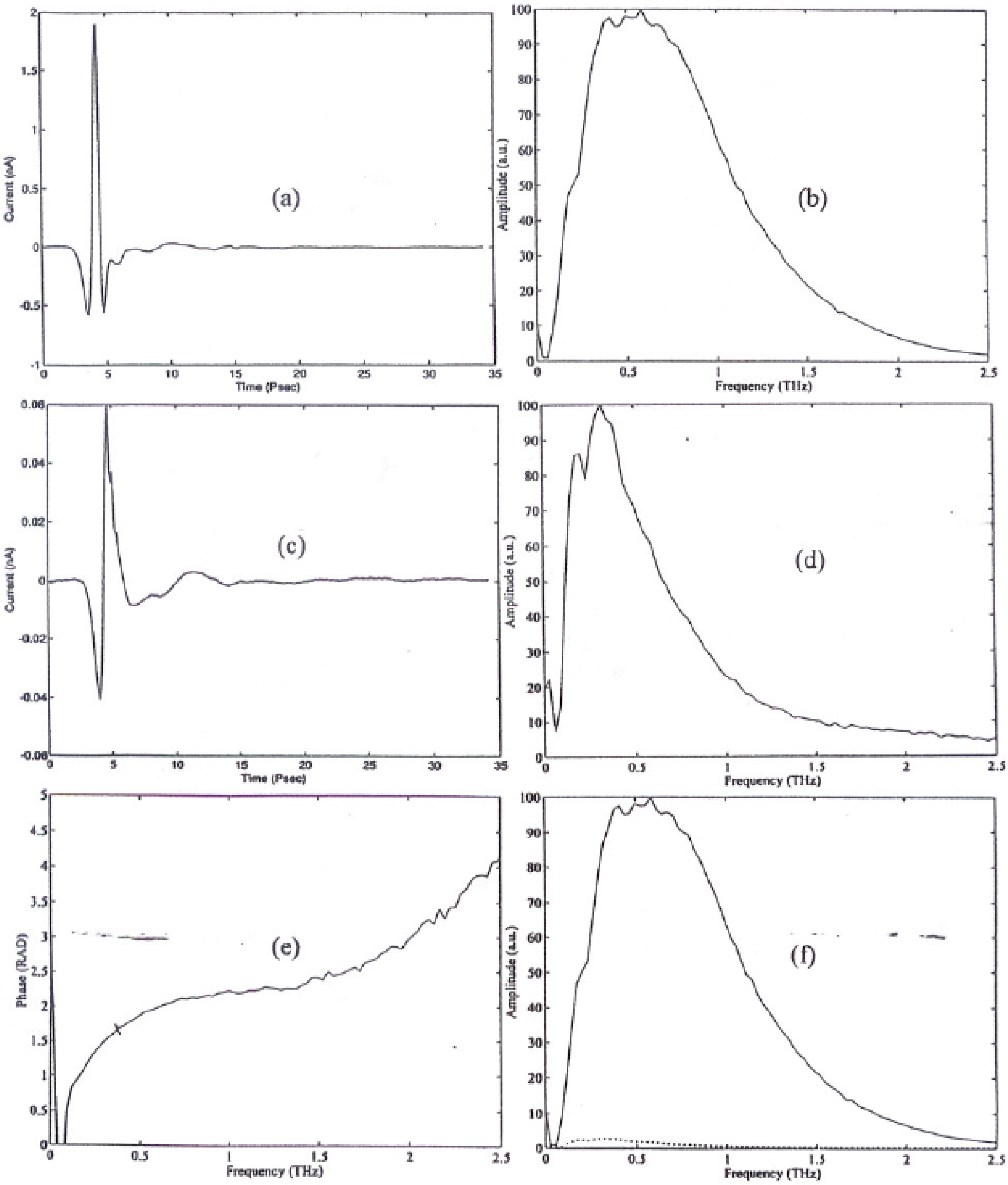

Figure B-9. 0.055 Ω cm, *n*-type Si (a) input THz pulse; (b) Normalized amplitude spectrum of (a); (c) output THz Pulse; (d) Normalized amplitude spectrum of (c); (e) The phase difference; (f) compare two amplitude spectra; input(solid line) and output (dashed line).

APPENDIX C

CALCULATION OF REAL AND IMAGINARY PART OF INDEX OF REFRACTION

The frequency-dependent complex dielectric constant ε is equal to the square of the complex index of refraction n=n$_r$ + *i* n$_i$.

$$\varepsilon = \varepsilon_\infty + i\frac{\sigma}{\omega\varepsilon_o} = \left(n_r + in_i\right)^2 \qquad \text{(C-1)}$$

$$\varepsilon_\infty + \frac{i}{\omega\varepsilon_o}\left(\sigma_{dc}\frac{\Gamma^2 + i\Gamma\omega}{\omega^2 + \Gamma^2}\right) = \left(n_r + in_i\right)^2$$

$$\varepsilon_\infty - \frac{1}{\omega\varepsilon_o}\left(\sigma_{dc}\frac{\Gamma\omega}{\omega^2 + \Gamma^2}\right) + i\frac{\sigma_{dc}}{\omega\varepsilon_o}\frac{\Gamma^2}{\left(\omega^2 + \Gamma^2\right)} = n_r^2 - n_i^2 + i2n_rn_i \qquad \text{(C-2)}$$

where $\sigma_{dc} = \frac{\omega_p^2\varepsilon_o}{\Gamma}$ and imaginary part is

$$2n_rn_i = \frac{\sigma_{dc}}{\omega\varepsilon_o}\frac{\Gamma^2}{\left(\omega^2 + \Gamma^2\right)}$$

$$n_i = \frac{1}{2n_r}\frac{\sigma_{dc}}{\omega\varepsilon_o}\frac{\Gamma^2}{\left(\omega^2 + \Gamma^2\right)} \qquad \text{(C-3)}$$

and the real part is

$$n_r^2 - n_i^2 = \varepsilon_\infty - \frac{\sigma_{dc}}{\omega\varepsilon_o}\frac{\Gamma\omega}{\left(\omega^2 + \Gamma^2\right)} \qquad \text{(C-4)}$$

From Equation (C-3) and (C-4),

$$n_r^2 - \frac{A^2\Gamma^4}{4n_r^2} = \varepsilon_\infty - A\Gamma\omega$$

$$n_r^4 - \left(\varepsilon_\infty - A\Gamma\omega\right)n_r^2 - \frac{A^2\Gamma^4}{4} = 0 \qquad \text{(C-5)}$$

where $A = \frac{\sigma_{dc}}{\omega\varepsilon_o}\left(\frac{1}{\omega^2 + \Gamma^2}\right) = \frac{\omega_p^2}{\omega\Gamma}\left(\frac{1}{\omega^2 + \Gamma^2}\right)$

From Equation (C-5) and (C-3)

$$n_r = \sqrt{\frac{\left(\varepsilon_\infty - A\Gamma\omega\right) + \sqrt{\left(\varepsilon_\infty - A\Gamma\omega\right)^2 + A^2\Gamma^4}}{2}} \tag{C-6}$$

$$n_i = \frac{A\Gamma^2}{2n_r} \tag{C-7}$$

VITA

TAE-IN JEON

Candidate for the Degree of

Doctor of Philosophy

Thesis: NEW APPLICATIONS OF THz TIME-DOMAIN SPECTROSCOPY

Major Field: Electrical Engineering

Biographical:

Personal Data: Born in Pusan, Korea, January 20, 1964, the son of Mr. Jeong-Weon Jeon and Mrs. Ok-Sun Ji.

Education: Graduated from Bae-Jeong High School, Pusan, Korea, in February 1982; received Bachelor of Science Degree in Physics from Dong-A University, Pusan, Korea, in February 1988; receiverd Master of Science Degree in Electronics Engineering from Dong-A University, Pusan, Korea, in February 1990; completed requirements for Doctor of Philosophy degree at Oklahoma State University in May 1997.

Professional Experience: Graduate Research Assistant, Department of Electrical and Computer Engineering and Center for Laser and Photonics Research, Oklahoma State University, June 1993 to present; Part-time Lecturer, Dong-A University, Pusan, Korea, March 1990 to June 1990; Part-time Lecturer, Gyung-Nam Technical Collage, Pusan, Korea, March 1990 to June 1990; Part-time Lecturer Dong-Eui Technical Collage, Pusan, Korea, March 1989 to June 1990.

Professional Membership: Optical Society of America (OSA), Institute of Electrical and Electronics Engineers (IEEE), Korean American Scientists and Engineers Association (KSEA).

Name: Tae-In Jeon Date of Degree: May, 1997

Institution: Oklahoma State University Location: Stillwater, Oklahoma

Title of Study: NEW APPLICATIONS OF THz TIME-DOMAIN SPECTROSCOPY

Pages in Study: 117 Candidate for the Degree of Doctor of Philosophy

Major Field: Electrical Engineering

Scope and Method of Study: The purpose of this study was to apply the THz Time-Domain Spectroscopy (THz-TDS) in thin film and doped silicon. In order to characterize of the samples, two pulse shapes were measured by the THz-TDS technique: the reference pulse without a sample and the output pulse with the sample. In the silicon measurement, transmission and reflection measurements were used to take the output THz pulse. Using Fourier analyses of the reference and output pulses, the frequency-dependent absorption and dispersion of the samples can be obtained.

Findings and Conclusions: Via ultrafast optoelectronic THz techniques, the multiple reflections theory was used in the thin film measurement and the theory and the measurement were well fit. The measured index of refraction was 1.51 and the power absorption was less than 1.5 /cm from 0.1 THz to 2.5 THz frequency range. In the silicon measurement, alternative theories of conduction were tested by precisely measuring the complex conductivity of doped silicon from low frequencies to frequencies higher than the plasma frequency and carrier damping rate. These results, obtained for both *n* and *p*-type samples, spanning a range of more than 2 orders of magnitude in the carrier density, do not fit any standard theory. A Cole-Davidson type distribution applied here for the first time to a crystalline semiconductor is in good agreement over the full frequency range with the complex conductivity and thereby demonstrates that the fractal conductivity is not just found in disordered material.

ADVISER'S APPROVAL: ____